MIXING AND TRANSPORT IN A FRINGING REEF LAGOON

By

JACQUELINE M. BRANYON

A DISSERTATION PRESENTED TO THE GRADUATE SCHOOL
OF THE UNIVERSITY OF FLORIDA IN PARTIAL FULFILLMENT
OF THE REQUIREMENTS FOR THE DEGREE OF
DOCTOR OF PHILOSOPHY

UNIVERSITY OF FLORIDA

2015

© 2015 Jacqueline M. Branyon

To my loved ones for all of their support

ACKNOWLEDGMENTS

First, I would like to thank my advisor, Dr. Valle-Levinson, for allowing me the opportunity to pursue my PhD in a field that I have become extremely passionate about. His enthusiasm, mentorship, and patience have allowed me to conduct my research in an independent manner, which has made me a better researcher and has helped shaped my scientific career. I would also like to thank the other members of my PhD committee: Dr. Maitane Olabarrieta, Dr. Robert Thieke, and Dr. Jonathan Martin. I truly appreciate the mentorship and guidance that all of my committee members provided. Their expertise and encouragement were invaluable in helping me complete this scientific endeavor.

I would also like to thank my colleagues: Lauren Ross, Kim Arnott, and Sabrina Parra, for their continued involvement in my growth as a research scientist. They continue to be wonderful mentors and role models. I am grateful for their countless reviews of my work and encouraging conversations. In addition, I would like to thank my other lab mates and field mates (Armando Castillo, Chris DiScenza, Amanda Tritinger, Sangdon So, Juan Paniagua, Fernanda Nascimento, Mo Al-Khaldi, Ahmed Yousif, and Zak Bedell) for their smiling faces and for making work more fun. I would also like to extend my gratitude to the members of the 2013 Water Institute Graduate Fellowship program for the unique learning opportunities (both in Florida and abroad) that allowed me to pursue interdisciplinary work.

The majority of my research was conducted in Puerto Morelos, Mexico, and would not have been possible without help from the following people: Ismael Mariño-Tapia, Mario Rebolledo Vieyra, Gemma Franklin, and Emmanuel Sanchez. I thank them for their help and great attitudes in successfully conducting fieldwork. It was a pleasure working with them and learning from them. I would also like to thank Edgar Escalante and others from Instituto de Ciencias del Mar y Limnología, Universidad Nacional Autónoma de México, for hosting our research.

Finally, I would like to thank my family and friends for their love and support over the years. They constantly surrounded me with laughter and love and believed in my character and ability to accomplish this dissertation. In particular, I would like to thank my parents, Leslie and Bob Branyon, for their love, invaluable support, sacrifices, and never-ending encouragement. I would also like to thank Cheryl Branyon, Katie Amerson, and Tim Brower for their love and friendship and for keeping me sane throughout this process. The care and understanding from all of my loved ones and friends has meant the world to me. Thank you to all who have supported me.

The research for this dissertation was funded by the NSF Coastal SEES program and the Water Institute Graduate Fellowship program.

TABLE OF CONTENTS

page

LIST OF TABLES

LIST OF FIGURES

LIST OF ABBREVIATIONS

BSA	Backscatter Anomaly is the demeaned instantaneous backscatter intensity
SGD	Submarine Groundwater Discharge is volumetric rate at which subterranean water leaves the seabed
SWI	Salt Water Intrusion is a backflow event at the spring that allows saltier lagoon water to enter the brackish water spring cavern.
TKE	Turbulent Kinetic Energy is the mean kinetic energy per unit mass in turbulent flow eddies
WSE	Water Surface Elevation is the relative height of the water's surface, η (eta)

Abstract of Dissertation Presented to the Graduate School
of the University of Florida in Partial Fulfillment of the
Requirements for the Degree of Doctor of Philosophy

MIXING AND TRANSPORT IN A FRINGING REEF LAGOON

By

Jacqueline M. Branyon

December 2015

Chair: Arnoldo Valle-Levinson
Co-chair: Maitane Olabarrieta
Major: Coastal and Oceanographic Engineering

Wave-driven circulation and inlet dynamics were investigated in a Caribbean fringing reef lagoon via velocity transect data collected by a towed ADCP along two lagoon-inlet systems over diurnal tidal cycles. Increases in inlet width and varying bathymetry caused atypical flow dynamics, including inflow at the inlets and residual recirculation patterns. A non-dimensional S number was proposed that relates inlet length to radius of flow curvature as a proxy of advective versus local acceleration to predict the occurrence of recirculation patterns. For large S numbers (>10), recirculation patterns can develop, as observed at the large inlet.

High-frequency (64 Hz) velocity measurements were used to observe submarine groundwater discharge (SGD) at springs in the lagoon over a fortnightly tidal cycle. The protected, low discharging (0.2 m/s) spring (Pargos) exhibited isotropic turbulence behavior and turbulent kinetic energy (TKE) values of ~0.2 m^2s^{-2}. The high recharge spring exposed to lagoon flows demonstrated anisotropic turbulence fields and higher TKE (~1.5 m^2s^{-2}). SGD and TKE varied inversely with the semidiurnal tide acquiring maximum values at low tide. At Pargos, turbulence dissipation rates were calculated

from the fast Fourier transform of velocities using the Taylor's Frozen Hypothesis. Tidal shifts in the inertial subrange followed Nasmyth spectrum expectations and rates of TKE dissipation reached maximum values (~ $5x10^{-3}$ m^2s^{-3}) during periods of sustained vertical velocity (~0.2 m/s). A linear relationship was established between the discharge velocity and log of dissipation, which allowed a reasonable prediction of SGD and dissipation rates through Bernoulli dynamics. This novel approach requires only a pressure head difference between the spring and inland water surface elevation.

A weeklong study investigated the interaction of lagoon circulation and SGD transport via a moored ADCP. A significant wave height threshold (0.3 m) determined if the SGD plume was carried away from its source by wave-driven circulation or if it remained at the spring. Turbulence generated by SGD was stronger than lagoon flow turbulence, and dissipation, production, and buoyancy determined TKE transport. In addition, infragravity waves and low frequency eddy overturning modulated plume movement.

CHAPTER 1
INTRODUCTION AND BACKGROUND

Mixing and Transport

The health of shallow reef-lagoon systems is dependent on the mixing and transport conditions of the flow fields. For the purposes of this dissertation, mixing will be defined as the changing of a physical system to create a tendency toward homogeneity in a heterogeneous system. Throughout the coastal reef system, mixing conditions affect the efficiency of transport mechanisms, which determine the movement and concentrations of important ecological parameters. For example, mixing will influence the following: biological transport, such as distribution of fish larva and coral reproductive spores; nutrient transport, such as dispersal of geochemical concentrations; and sediment transport, including beach nourishment or erosion [*Monismith,* 2007; *Hearn,* 2011; *Hench and Rosman,* 2013].

It is widely accepted that the hydrodynamics of coral reefs modify transport processes, which determine the ecological efficiency and health of these systems [*Monismith,* 2007; *Hearn,* 2011; *Hench and Rosman,* 2013]. The spatial scales of coral reef hydrodynamics can vary from several kilometers (regional scales) [e.g., *Hench et al.,* 2008; *Lowe et al.,* 2009] to less than a millimeter (molecular scales) [*Hearn and Hunter,* 2001]. In addition, hydrodynamics associated with lagoon-reef flows vary temporally from time scales that occur instantaneously (<1s), daily (tidal), weekly (fortnightly and subtidal), monthly, and annually. Furthermore, the highly variable temporal and spatial scales of physical processes in reefs are interconnected [e.g., *Hearn and Hunter,* 2001]. However, as the number of physical processes that are studied increases, the ability to resolve dependent and independent mechanisms becomes more difficult. Nevertheless, it is important to consider the relation of individual processes with respect to the system as a whole for scientific investigations [e.g., *Hearn and Hunter,* 2001]. This dissertation will focus on the temporal and spatial evolution of mass transfer to explain mixing in shallow reef systems.

Circulation

Circulation affects transport mechanisms vital to the ecological health of coral reef systems, including: sediment, nutrient, and pollutant transport [*Prager,* 1991; *Hench et al.*, 2008; *Lowe et al.,* 2009b]. Previous studies found that in these environments, circulation is driven by waves, tides, and wind [*Roberts et al.* 1975*; Andrews and Pickard*, 1990]. The relative importance of these mechanisms is determined by the local morphology and oceanic forcing conditions found in the coral reef systems [*Lowe et al*., 2009]. The morphology of a fringing reef system is classified as coral reefs growing adjacent to a coastline, allowing for the formation of shallow lagoons and ocean exchange flow at reef breaks [*Kennedy and Woodroffe*, 2002]. Creating a morphologic barrier, reefs dissipate incoming wave energy, lowering significant wave height and energy within the lagoon. As a result of wave-breaking at the reef, waves drive circulation in shallow reef systems. Waves breaking over the reef generate radiation stress gradients resulting in a setup of the water surface in the lagoon, which drives outflow at the reef breaks [*Longuet & Stewart,* 1964;*Coronado et al.*, 2007; *Hench et al.,* 2008; *Taebi,* 2011]. The expected behavior of wave-driven circulation consists of inflow over the reef, alongshore flow in the lagoon, and outflow at the inlets [*Hench et al.,* 2008; *Taebi,* 2011].

Numerical models have simulated these flow structures [*Lowe et al.,* 2009b; *Marino et al.,* 2010], and observational studies have proposed circulation patterns over varying spatial scales (ranging from kilometers to meters) and temporal scales (ranging from months to seconds) [*Coronado et al.,* 2007; *Taebi et al.,* 2011; *Hench et al.,* 2008]. However, still to be determined is the tidal influence on the spatial structure of wave-driven currents and in particular the intratidal flow structures at inlets at spatial resolution of O(10m).

Other studies have shown that mean sea level changes over the reef will influence wave-driven currents [*Hearn,* 1999; *Coronado et al.,* 2007]. This concept suggests that tides, even those in microtidal systems, could affect wave-driven currents, especially under low wind and low wave height conditions. Circulation is one of the mixing processes that determine flow behavior in a reef-lagoon system. Another mixing process is the turbulent discharge of submarine groundwater into the lagoon.

Submarine Groundwater Discharge

Submarine groundwater discharge (SGD) has become widely recognized as a critical connection between groundwater resources and the sea, playing a consequential role in the global budget of dissolved materials [*Moore 1996*; *Santos et al.,* 2008; *Valle Levinson et al.,* 2011]. Research has shown that SGDs can vary from slow diffusive fluxes (~ cm/day) through bed sediment seepage [*Paulsen et al.,* 2007; *Martin et al.,* 2007] to rapid fluxes (~1 m/s) at point sources [*Valle Levinson et al.,* 2011]. Diffuse SGDs typically occur through low-permeability mediums (sandy sea beds), while point SGDs are associated with highly permeable karst topography [*Burnett,* 2006; *Valle Levinson et al.,* 2011]. Although seepage sources may provide more flux by volume to the global budget, point sources, such as submarine springs, establish a rapid response relationship between groundwater resources and the ocean [*Valle Levinson et al., 2011; Parra et al.,* 2014].

In coastal karst aquifers, point SGD sources are formed over time from the dissolution of limestone that creates a complex groundwater matrix of subterranean conduits [*Moore 1996*; *Beddows et al.,* 2007; *Valle Levinson et al., 2011; Parra et al.,* 2014]. In mature karst topography, like the Yucatan peninsula, meteoric surface water drains to subterranean cave systems [*Kaufmann,* 1999], as indicated by the absence of rivers [*Beddows et al.,* 2007]. The lack of surface water resources and the direct connection between subterranean freshwater resources and the sea makes these karst conduit systems particularly vulnerable to threats of sea level rise, pollution, and depleting resources due to increased consumption.

Recently, studies have made an effort to understand the hydrologic characteristics of SGDs at springs [*Peterson et al.,* 2009; *Valle-Levinson et al.,* 2011; *Exposito-Diaz et al.,* 2013; *Parra et al.,* 2014]. In these systems, the peizometric pressure heads of the inland water table and the sea surface balance the groundwater matrix and control SGD [*Valle Levinson et al.,* 2011]. The change in sea surface elevation due to tides, wind, waves, storm surge, and set-up have been shown to modulate the spring's discharge based on a relative pressure gradient [*Li et al.,* 1999; *Kim and Hwang,* 2002; *Taniguchi,* 2002; *Valle Levinson et al.,* 2011; *Vera et al.,* 2012; *Parra et al.,* 2014]. When the pressure gradient between inland groundwater and the sea surface increases, spring discharge will also increase. When the gradient becomes less or reverses in direction, SGDs become weaker and more sensitive to even slight changes in mean sea level. Previous studies [*Valle-Levinson et al.,* 2011; *Parra et al.,* 2013] have observed that in shallow estuaries in the Yucatan peninsula, an increase in sea level can even lead to reversal of spring flow, causing saltwater intrusion into the aquifer. To protect groundwater resources, it is crucial to understand the discharge behavior of the system in order to predict how it will respond to sea-level rise.

Other studies have highlighted the significance of SGDs to the quality of the groundwater and its dispersion (and resulting impact) on the coastal ecosystems [e.g., *Hernandez-Terrones*, 2010]. In karst topography like the Yucatan peninsula, groundwater can become polluted by rain runoff, resulting in increased chemical (phosphorus and nitrogen) fluxes to lagoon reefs via SGD [*Mutchler et al.,* 2007; *Young et al.,* 2008; *Hernandez-Terrones*, 2010]. These increases in nitrogen and phosphorus in the lagoon can alter the ecosystem's health (e.g., increases in seagrass production) [*Carruthers et al.,* 2005] and cause phytoplankton and macroalgae blooms that change aquatic habitats [*Valiela et al*., 1990]. In addition, SGDs are typically more buoyant than lagoon waters due to their lower salinity. As a result, buoyant plumes discharging at the seabed rise to the surface and are transported by lagoon flows. While these plumes can be monitored by dye or chemical tracers, the variability of their location in the water column has made it difficult to capture their physical properties. One such property that is very evident in these SGDs is turbulence.

Turbulence

Turbulence from submarine springs can enhance mixing in the water column, which influences nutrient, pollutant, and sediment transports and concentrations, impacting the biological health of the system [*Rippeth et al.,* 2001; *McCaffrey et al.,* 2014]. Progress has been made in understanding turbulence for energetic tidal [*Rippeth et al.,* 2001; *Souza et al.,* 2004; *Thomson et al.,* 2010; *McCaffrey et al.,* 2014] and shelf flows [*Vermeulen, et al.,* 2011; *Palmer et al.,* 2014]. But relatively few studies have focused on turbulence at SGDs [*Peterson et al.,* 2009; *Exposito-Diaz et al.,* 2013; *Parra* *et al.,* 2014]. Based on previous work, we expect the maximum values of turbulent kinetic energy (TKE), turbulence dissipation [*Parra et al.,* 2014], turbulence production, and vertical eddy viscosity [*Exposito-Diaz, et al.,* 2013] to occur during low tide when the discharge and vertical velocity are at maximums. Studies at submarine springs have shown that turbulence is dependent on discharge intensity and the lunar tides [*Exposito-Diaz et al.,* 2013; *Parra et al.,* 2014], but they were limited in their data resolution (≤4 Hz sampling rate) and time series (~4 days). Longer studies (+10 days) have addressed fortnightly variability in seepage and point SGDs [*Kim and Hwang,* 2002; *Taniguchi,* 2002] and TKE [*Parra et al.,* 2015], but have not examined the variability of turbulence dissipation rates.

Motivation and Objectives

Submarine groundwater discharge (SGD) provides a critical connection between groundwater resources and the marine environment, effecting the dispersion of subterranean waters (and resulting impact) on the coastal ecosystems [*Hernandez-Terrones*, 2010]. However, groundwater can become polluted by runoff, resulting in increased chemical (phosphorus and nitrogen) fluxes to lagoon reefs via SGD [*Mutchler et al.,* 2007; *Young et al.,* 2008; *Hernandez-Terrones*, 2010]. These increases in nitrogen and phosphorus in the lagoon can alter the ecosystem's health (e.g., seagrass) [*Carruthers et al.,* 2005] by causing phytoplankton and macroalgae blooms that change aquatic habitats [*Valiela et al*., 1990]. It is therefore critical to understand the fate of SGD within a fringing reef lagoon.

The first objective of this paper is to investigate lagoon-inlet circulation, with a focus on the tidal influence in a microtidal environment. Using high spatial resolution data, lagoon-inlet circulation patterns are resolved and the vertical structure of flow is analyzed at the reef breaks.

The second objective of this study is to examine SGD at point source springs. To accomplish this, high-resolution velocity data are used to characterize and compare turbulence and SGDs at two different point sources in close proximity (< 200m) in a fringing reef lagoon. The seasonal variability is analyzed, as well as variability in the spring-neap tidal cycles. In addition to turbulence observations, methods of predicting spring discharge and TKE dissipation rates are proposed by analyzing karst conduit flow.

The final objective of this investigation is to determine the relationship between lagoon flows and SGDs. To date, previous studies have not investigated the interaction between lagoon flows and the SGD plume in the water column. To address this, vertical profiles of velocity are examined near a spring. Conditions for mixing behavior are established and movement of the SGD plume is analyzed with respect to lagoon flows.

CHAPTER 2
TIDAL AND RESIDUAL LAGOON-INLET CIRCULATION

Introduction to Circulation

Circulation determines transport of materials that are vital to the health of coral reef systems. Transport effects the dispersion and concentrations of sediments, nutrients, and pollutants by lagoon-scale flows [*Prager,* 1991; *Hench et al.*, 2008; *Lowe et al.,* 2009b]. Previous studies found that in coral reef environments, circulation is driven mainly by waves, tides, and wind [*Roberts et al.,* 1975; *Andrews and Pickard*, 1990]. The relative importance of these forcing mechanisms depends on the morphology and oceanic conditions inherent to a particular reef [*Lowe et al.,* 2009a]. For example, in shallow, microtidal fringing reef systems, waves tend to dominate circulation, while tides play a minor role [*Coronado et al.,* 2007; *Hench et al.*, 2008; *Lowe et al.,* 2009a; *Lowe et al.,* 2009b]. In fringing reef systems, coral reefs grow adjacent to the coastline, allowing for the formation of shallow lagoons and ocean exchange flow at reef breaks [*Kennedy and Woodroffe,* 2002]. Creating a morphologic barrier, reefs dissipate incoming wave energy, resulting in decreased significant wave height in the lagoon. It is well recognized that waves drive circulation in shallow reef systems by breaking over the reef, generating cross-shore radiation stress gradients. *Taebi et al.,* [2011] explains how the excess momentum associated with the waves induces currents across the reef that must be balanced according to continuity. As a result, the mass flux due to the wave generated stress gradients causes a water level setup in the lagoon that drives outflow at reef breaks [*Longuet & Stewart,* 1964; *Coronado et al.,* 2007; *Hench et al.,* 2008; *Taebi et al.,* 2011]. The expected wave-driven inflow over a reef is illustrated in Figure 2-1 with alongshore flow within the lagoon, and outflow at the inlets.

Numerical models have simulated these flow structures [*Lowe et al.,* 2009b; *Marino et al.,* 2010], and observational studies have proposed circulation patterns over varying spatial scales (ranging from kilometers to meters) and temporal scales (ranging from months to seconds) [*Coronado et al.,* 2007; *Taebi et al.,* 2011; *Hench et al.,* 2008]. However, still to be determined is the tidal influence on the spatial structure of wave-driven currents (or intratidal flow structures at inlets) at fine spatial (< 1m) and temporal (intratidal) resolutions. Other studies have shown that mean sea level changes over the reef can influence wave-driven currents [*Hearn,* 1999; *Coronado et al.,* 2007]. This concept suggests that tides, even those in microtidal systems, could affect wave-driven currents, especially under low wind (< ~3 m/s) and low significant wave height (<0.3 m) conditions. The objective of this study is to describe the kinematics and dynamics of the circulation over a diurnal tidal cycle in a microtidal fringing reef system, Puerto Morelos, Mexico.

The circulation of Puerto Morelos lagoon has been studied via observational experiments [*Merino-Ibarra and Otero-Davalos,* 1991; *Coronado et al.,* 2007] and numerical models [*Marino et al.,* 2010], which showed that currents are driven by waves, with minor influences from remote forcing (Yucatan Current), tides, and wind. However, these studies were limited in their spatial resolution, as well as their ability to resolve circulation patterns and vertical structure of flow at the reef breaks. This study addresses those limitations and investigates the tidal influence on circulation in this specific microtidal environment.

In the Methodology section, the experiment site, sampling methods, and data analysis techniques are reviewed. Then, the findings are presented in the Results section, focusing on inlet dynamics by comparing tidal and residual flow fields. In the Discussion section, tidal variations of the flow kinematics are determined through horizontal divergences and vertical components of relative vorticity; the dominant terms of the horizontal momentum balance are presented; and conditions are suggested when an inlet is susceptible to gyre formation through a non-dimensional number, which compares advective to local accelerations.

Methodology

Site Description

Puerto Morelos in Quintana Roo, Mexico (Figure 2-2) marks the origin of the Mesoamerican Reef, one of the longest barrier reefs (>1000km) in the world. The fringing reef at Puerto Morelos is approximately 4 km in length along the coast and encloses a lagoon that varies in width from 500 to 1,500 m (Figure 2-2). The shallow (3-4 m average depth), lagoon has three reef breaks: two inlets (at the north and center of the reef) and a navigation channel to the south. The northernmost inlet, Boca Grande, is approximately 700 m wide and 6 m deep; the central inlet, Boca Chica, is approximately 250 m wide and 5 m deep; and the navigation channel to the south is 400 m wide and dredged to approximately 8 m [*Coronado et al.,* 2007]. Roughly 10 km offshore, the shelf edge drops to >400 m [*Ruiz-Renteria et al.,* 1998]. The reef provides a unique habitat for coral and marine life, as well as necessary shore protection by dissipating wave energy from deep-water waves.

Tides are semidiurnal with a form-factor of (~0.34), indicating a slight diurnal influence. The tidal range is 10 to 30 cm, and current generation within the lagoon is dominated by wave-driven flows [*Coronado et al.,* 2007]. The winds in the area are dominated by easterly Trade Winds (typically 4-10 m/s), which generate waves with an annual significant wave height of 0.8 m and a typical period of 7 seconds [*Coronado et al.,* 2007].

Puerto Morelos' karst aquifer allows for the formation of multiple sources of submarine groundwater discharge (SGD) (both seepage and point sources) in the lagoon. As a result, the salinity inside the lagoon varies from 22 g/kg at SGD points, to an average of 36 g/kg inside the lagoon.

Sampling Methods

During neap tide in July 2011, a downward pointing RDI 1200 kHz Workhorse Acoustic Doppler Current Profiler (ADCP) was towed in a repeated circuit. The ADCP sampled current profiles and bathymetry throughout the lagoon at 2.5 Hz. The continuous circuits of current profiles captured cross sectional flow fields along the lagoon and across the inlets over two separate 24-hour experiments (Figure 2-2). One circuit was covered on July 21-22, 2011, at the central inlet (Boca Chica) with a total of 38 repetitions. A second circuit provided data on July 23-24, 2011, at the northern inlet (Boca Grande) with 32 repetitions. The vertical resolution (bin size) of the velocity data was 0.25 m and reached an average depth of ~5 m. A Differential Garmin Global Positioning System (DGPS) determined geographic coordinates during the experiments, which were then used to correct the velocity data for the vessel's velocity (~1.5 m/s). Raw velocity profiles were averaged in ensembles of 20 profiles (8 s intervals) to produce a spatial resolution of ~12 m. These experiments provided current velocity data with a spatial resolution that is rarely found in reef lagoons.

Wind data were obtained from a meteorological station located on a pier at the National Autonomous University of Mexico (UNAM), approximately 2 km southwest of the Boca Chica inlet. Wave data were also collected during the experiments from a moored ADCP at the reef, ~200 m south of the Boca Chica inlet. Figure 2-3 shows the wind vectors as well as the water surface elevation and significant wave height during sampling of the two circuits.

During Boca Chica measurements, winds were ~5 m/s and predominantly southwestward, and significant wave heights varied between 0.3 and 0.4 m. For the Boca Grande experiment, the winds were ~7 m/s and predominantly northwestward. The significant wave height during this period ranged from 0.5 and 0.7 m, shy of the 0.8 m annual average, but clearly higher than the summer expected wave height of 0.2 m [*Coronado et al.,* 2007].

Data Analysis

The collected ADCP data were compass-corrected using the method of Joyce [1989]. Then, circuit data were separated into individual transects of uniformly gridded data in space and time. The spatial resolution of the gridded transects was 30 m in the horizontal and 0.25 m in the vertical for Boca Chica, and 25 m in the horizontal and 0.25 m in the vertical for Boca Grande.

A least-squares fit (LSF) to diurnal (K1) and semidiurnal (M2) harmonics was then used to determine the tidal contribution to the horizontal velocity components (*u,v*) at each transect. The LSF analysis produced five parameters for both the *u* (East-West, across-lagoon flow) and the *v* (North-South, along-lagoon flow) components of flow. The parameters were the subtidal flow (u_s, v_s); the amplitude (u_{a2}, v_{a2}) and phase ($u_{\theta 2}$, $v_{\theta 2}$) of the semidiurnal tidal constituents; and the amplitude (u_{a1}, v_{a1}) and phase ($u_{\theta 1}, v_{\theta 1 1}$) of the diurnal tidal constituents. As shown by *Valle-Levinson et al.* [2009], the simultaneous signal at all points of an interpolated mesh grid can be reconstructed from the fit to the equation:

$$(u,v) = (u_s, v_s) + (u_{a2}, v_{a2})\sin[\sigma_2 t + (u_{\theta 2}, v_{\theta 2})] + (u_{a1}, v_{a1})\sin[\sigma_1 t + (u_{\theta 1}, v_{\theta 1})] \qquad \text{(2-1)}$$

where σ_2 and σ_1 are the M2 semidiurnal (2π/12.42 h) and K1 diurnal (2π/23.9 h) tidal frequencies, and *t* is time in hours from the beginning of the sampling transect.

Flow fields were then reconstructed in the horizontal plane at each bin depth by interpolating among transects (e.g., BC: transects 1-3 and BG: transects 1-4). The spatial resolution of the uniform grid was approximately 25 m across the lagoon and 10 m across the inlets, to allow for a higher spatial analysis of inlet dynamics. The reconstructed grids allowed inspection of the expected flows fields at any time, *t,* during the experiment. Flow fields were calculated in half hour increments to evaluate the intratidal evolution of flow. These reconstructed flow fields are used to present a kinematic and dynamic analysis associated with the circulation patterns.

Kinematics

In order to gain a basic understanding of tidal and non-tidal flow patterns, the horizontal divergence is calculated as:

$$\nabla \cdot u_h = \frac{\partial u}{\partial x} + \frac{\partial v}{\partial y} \qquad \text{(2-2)}$$

The right hand side components ($\frac{\partial u}{\partial x}, \frac{\partial v}{\partial y}$) can be calculated from gridded observations to determine horizontal divergence or convergence of flow.

Similarly, the vertical component of relative vorticity, associated exclusively with horizontal flows, can be determined with observations through:

$$(\nabla \times u)\mathbf{k} = \frac{\partial v}{\partial x} - \frac{\partial u}{\partial y} \tag{2-3}$$

Positive values indicate counter-clockwise rotation of horizontal flows.

Dynamics

As presented later, vertical homogeneity in horizontal currents allow the use of a vertically averaged momentum balance to study the hydrodynamics along the circuits sampled. The *U* and *V* components of the horizontal momentum balance, where capital letters indicate vertically averaged, can be written as:

$$\frac{dU}{dt} - fV = -\frac{1}{\rho}\frac{\partial P}{\partial x} + \frac{\mathrm{T}_x}{\rho H} \tag{2-4}$$

$$\frac{dV}{dt} + fU = -\frac{1}{\rho}\frac{\partial P}{\partial y} + \frac{\mathrm{T}_y}{\rho H} \tag{2-5}$$

The first term is total flow acceleration, which is composed of the local and advective acceleration terms. The second term represents the Coriolis acceleration. The forces on the left side are balanced by the barotropic pressure gradient (third term) and frictional effects (last term on the right-hand side). The last term include surface and bottom stresses. For the purposes of this study, the baroclinic pressure gradient terms are ignored because the water column is well mixed. In fact, baroclinic accelerations are two orders of magnitude smaller than barotropic forces per unit mass. Frictional effects due to the wind were estimated similarly to the frictional bed term. However, frictional forcing due to the wind was on average lower (order of magnitude) than frictional forcing at the bed. For details on the calculations relating to equations 2-4 and 2-5 please see the supplemental equations in the Appendix.

Results

Measurements at both Boca Grande and Boca Chica circuits were collected over neap tide, during tidal ranges of ~15 cm. This section analyzes depth-averaged flows observed at the inlets and the resulting constituents of the Least Squares Fit (LSF) to the tidal harmonics. This is followed by examination of the residual horizontal flow fields (surface and depth averaged) throughout the circuits, as well as the residual behavior at the inlet with respect to depth. Throughout the presentation of the results, the behavior of the flow fields will be compared for the two inlet systems. The results that follow are the first of its kind to be reported for this area and are relevant to reef lagoons throughout the world.

Inlet Flows

The two inlets behaved very differently according to their variations in width and bathymetry. Boca Chica is a smaller, relatively flat bottom inlet, while Boca Grande is a larger, bathymetrically variable inlet, as shown in Figure 2-4.

At Boca Chica, the depth-averaged *U* component of flow (Figure 2-4B) was modulated by the semidiurnal tide (Figure 2-4A). Strongest outflows (eastward at 12 cm/s) occurred during the semidiurnal flood and strongest inflows (westward at 6 cm/s) occurred during the semidiurnal ebb, which may seem counterintuitive. However, the total water surface elevation (tides + significant wave height) was highest during flood tide, causing a greater setup in the lagoon that drove outflow at the inlet (Figure 2-4A). The *V* component of flow for Boca Chica (Figure 2-4C) was southward during low tide and northward during high tide, but overall, appeared to be weaker than the *U* component of flow (Figure 2-4B). The Boca Chica inlet bathymetry is relatively flat (5.4-

5.6 m depth range), favoring relatively uniform flow conditions across the inlet (Figure 2-4B&C).

The flows at Boca Grande inlet were also wave-driven with less apparent semidiurnal variations as compared to Boca Chica (Figure 2-4E&F). The significant wave height during the Boca Grande experiment was over twice that of the Boca Chica experiment (Figure 2-4A&D), causing an increase in setup that likely subdued the tidal signal. However, the semidiurnal tide still influenced the flow by modifying the total water surface elevation. The sum of the tidal signal (η) and the significant wave height (H_s) is depicted by the red line in Figure 2-4D and appear to oscillate at a period of ~6 hours. To investigate this oscillation in the water surface elevation, we applied the LSF analysis to the K1, M2, and M4 tidal constituents. In doing so, the influence of the M4 tidal component in Boca Grande becomes evident (Figure 2-5E).

The M4 signal is an overtide harmonic generated by the interaction of the M2 harmonic (period of 12.42 hours) with itself. The presence of the M4 harmonic (period of 6.21 hours) in Boca Grande is likely due to the well-defined M2 signal in the water surface elevation (Figure 2-4D). During the Boca Grande experiment tides were predominantly semidiurnal, while during the Boca Chica experiment tides had a mixed (semidiurnal-diurnal) form. The mixed tidal conditions result in a subdued influence of the M4 overtide at Boca Chica, as observed in the tidal constituent amplitudes (Figure 2-5B).

The flows at Boca Grande were also modified by variable bathymetry (3.8- 6.4 m depth range) that caused lateral variation in flow across the inlet. Northeastward outflow occurred at the deeper south end and southwestward inflow occurred over the shallower north end of the inlet. The strength of the *U* and *V* components was of similar magnitude (Figure 2-4E&F), unlike Boca Chica where the *U* component dominated the flow (Figure 2-4B&C). In addition, Boca Grande flows were in opposing directions at the inlet edges, indicating lateral shears that would allow for counter rotating circulation patterns. The competing inflow around the north edge of the inlet and outflow at the southern edge was present throughout the experiment, suggesting that the recirculation conditions would be observed in the tidally averaged flow. Therefore, the origin and thresholds of these recirculation patterns will be explored further in the residual flow Results and Discussion section of the paper.

Residual or Tidally Averaged Flows

The residual (or tidally averaged) flow analysis of the inlet systems focuses on the spatial variability in the horizontal (x,y) plane over the lagoon and the vertical (y,z) plane across the inlet. The reconstructed signal of the M2, K1, and M4 harmonics (Figure 2-5A&D) closely matches the observed flow values with root mean squared errors less 0.08 m/s for both experiments.

Boca Chica

In the Boca Chica surface and depth-averaged flows, the circuit flows were predominately eastward, indicating weak alongshore variation (Figure 2-6A&B). At the inlet, both surface and depth-averaged flows indicated residual outflow. To examine the tidally averaged variation in velocity with respect to depth, the residual flow at the inlet were examined, as seen in Figure 2-7A. The Boca Chica vertical structure of horizontal velocities demonstrated converging outflow (eastward). The strongest outflows (20 cm/s) occurred ~1 m below the surface, decaying with depth due to the bottom frictional influence. The southwestward wind conditions opposed the surface residual outflow, damping its strength and altering the direction with respect to flows at depth. The periods of inflow observed during ebb of the semidiurnal tidal cycle (Figure 2-4) do not appear in the residual component. The residual outflows at the Boca Chica inlet agree with numerical simulations [*Lowe et al.,* 2009b] and observed inlet behavior [*Coronado et al.,* 2007; *Lowe et al.,* 2009a] for wave-driven circulation systems. Similar to a funnel, flows converge in a uniform direction as water exits the lagoon, creating the strongest outflows in the center of the inlet.

Boca Grande

The residual flows for Boca Grande are unlike the typically expected flow patterns for shallow reef lagoon systems (Figure 2-1). At Boca Grande alongshore flow competes with offshore flow, which produces a cyclonic flow recirculation. The location and strength of this recirculation varies based on the shift in laterally sheared flows with respect to depth. The gyre occurs at the north end of the inlet in the surface flow field, as seen in Figure 2-6C. However, as the magnitude of the alongshore flows increases with the tide, the gyre shifts in the direction of the alongshore flow, appearing at the southern end of the inlet in the depth averaged flows (Figure 2-6D). This is likely the result of the northwestward wind opposing the predominant southwestward (alongshore) currents. The across lagoon residual flow structure at the Boca Grande circuit is highly variable, transitioning from southwestward flow (~20 cm/s) near the shore to northeastward flow (~35 cm/s) at the inlet. The strongest flows occur in the deepest section of the inlet near its southern end, indicating that frictional effects dominate over inertial effects [*Valle-Levinson et al.*, 1998]. At this change in geometry, flows rotate clockwise with respect to depth, likely due to a combination of bathymetric changes and centrifugal acceleration as outflow curves at the inlet edges.

The Boca Grande cross-inlet residual flows transition from strong outflow (35 cm/s) at the southern end of the inlet to inflow (10 cm/s) at the northern end, creating vertical variability of the cross-inlet flow field (Figure 2-6D). Lateral shears occur at the north end of the inlet, where weak (5-10 cm/s) inflow is present throughout the water column (Figure 2-7B). In addition, two-layer flow occurs in the center of the inlet, with outflow at the surface and inflow at depth. Similar to Boca Chica, the wind competes against the surface flow field. Possible explanations for the complexity of the residual flows include the increased inlet width and the increase in wind strength and H_s, as compared to Boca Chica conditions. The complex spatial structure of residual flow across the Boca Grande inlet creates conditions for unique circulation patterns to occur, which is further explored in the Discussion.

In both inlet systems, the residual maps demonstrate the influence of the wind (Figure 2-6) upon comparison of the depth-averaged flows to flows at the surface. Typically in fringing reef systems, the influence of the wind is coupled with the swells they generate, especially in relatively constant wind regimes (e.g., easterly Trade Winds) [*Coronado et al.,* 2007]. In 2007, *Coronado et al.,* showed that the generation of wind waves was the main mechanism for wind influencing circulation within the Puerto Morelos lagoon, with a minor influence on the subinertial (> 33.7 hr) currents. However, the residual flow fields demonstrate that the influence of the wind should be considered as a separate, local component that can impede or enhance lagoon flows. The influence of the wind on wave-driven currents becomes especially important when evaluating the transport mechanisms of pollutants or nutrients that are less dense that the lagoon water and are therefore strongly influenced by wind and resulting surface currents.

Discussion

Kinematics of Inlet Systems

The previous residual flow analysis described the subtidal flow fields of the two inlet systems. Even in this microtidal environment, the influence of tidal flows is relevant to the residual circulation. Intratidal kinematics are thus linked to residual recirculation structure near the inlet. Horizontal divergence (convergence) is examined, together with the vertical component of relative vorticity of the flow. Reconstructed surface flows are used for these calculations at both inlet systems. Results are markedly different from inlet to inlet.

Figure 2-8 shows the evolution of divergence and vorticity fields over a diurnal tidal cycle at Boca Grande. In the lagoon, flows are typically convergent, increasing in strength from high tide to the maximum values (-0.001 /s) at flood. As flows approach the inlet, they become divergent, decreasing in strength from high tide (0.0015 /s) to flood. Inlet flow divergence appears to be inversely related to vorticity. The relative vorticity values increase from high tide to flood, with maximum values occurring during flood, reaching ~0.0013 /s, indicating cyclonic flow. This implies that during flood, when along and across flows compete at the inlet and when divergence is weakest and vorticity is strongest, the counter-rotating gyres will be greatest.

In contrast to Boca Grande, the kinematics of Boca Chica reveals that divergence and vorticity are influenced more by the diurnal tidal cycle than the semidiurnal cycle, likely due to the muted semidiurnal signal seen in the water surface elevation in Figure 2-3B. The diurnal modulation can be seen in Figure 2-9 where flows transition from convergent (flood) to divergent (low tide) in the first semidiurnal cycle, but exhibit opposite behavior in the following semidiurnal cycle. This is also seen in the vorticity contours where flow rotation directions initially transition from counter-clockwise (flood) to clockwise and slack flows (low tide), and then switches from clockwise (flood) to counter-clockwise rotation (low tide) in the next semidiurnal cycle.

The comparison of the kinematics implies that tidal elevations modulate flow patterns, despite being a microtidal environment. By comparing the tidal range to the significant wave height, a non-dimensional parameter is established to examine the relative influence of tides versus waves, which typically drive circulation in these systems. At Boca Chica, the ratio of tidal range to significant wave height is 0.57, while at Boca Grande the ratio is 0.31. This simple comparison helps explain the behavior of the kinematics over the experiment. For Boca Grande, higher significant wave height resulted in low intratidal variability. In contrast, Boca Chica had lower wave height conditions resulting in a higher tide to wave ratio that caused the kinematics to vary intratidally. These results provide a fundamental fluid analysis of the flow patterns that are very different kinematically, despite the geographic proximity. Implications of these results suggest that even in microtidal environments, tides play a non-negligible role in determining flow behavior, even more so during low wave height conditions.

Boca Chica (200 m wide) exhibits the expected behavior of a shallow reef lagoon-inlet system. This is seen in the funneling of the intratidal inlet flows with convergence occurring during flood, or outflows, and divergence occurring during ebb, or inflows (Figure 2-4). In addition, the residual flows throughout the sampling trajectory depict seaward flows with outflow occurring throughout the inlet. However, just 1 km north, Boca Grande (700 m wide) is uniquely different in its flow patterns. At Boca Grande's sampling trajectory, flow fields are southward in the lagoon, showing recirculation near the inlet, and are spatially variable at the inlet. The differences in spatial structure of flow at the two trajectories stem from wind conditions, wave height, tidal variability, width of the inlet, and bathymetric features.

The increased significant wave height likely increased the alongshore flow in the lagoon during the Boca Grande experiment. North of Boca Grande, the wave breaking over the reef induced a setup, causing southward, or alongshore, flows in the lagoon. At the inlet, morphology and wind forcing modified the setup driven outflow, allowing a northward component of flow. The competition of the opposing alongshore flows favored conditions for counter-rotating flows that developed at the Boca Grande inlet. The strength of the alongshore flows also determined the location of the gyre. Figure 2-5B shows that the southward flow increased with respect to depth, forcing the cyclonic gyre to form further south.

The bathymetric features of the Boca Grande inlet also favored the development of counter-rotating flow. Across the inlet, the strongest flows appeared at the southern end over the deepest bathymetric pocket. Friction retarded outflows over the shallow northern end, allowing for inflow that was related to the cyclonic gyres. The documentation of inflow at the inlet and the development of recirculation patterns are unique findings that have not been reported in previous studies at coral reef breaks.

Inlet Characterization on the Basis of Dynamics

Previous studies have examined hydrodynamics of shallow tidal inlets [*Hayes,* 1979; *Hench et al.,* 2002] based on a number of factors, including: salinity, morphological dimensions, wave height, and currents. In 2002, *Hench et al.* used a form of the Rossby number to examine curvature effects for tidally driven inlets by comparing centrifugal and Coriolis accelerations through the following relation:

$$Ro = \left| \frac{U^2/_R}{fU} \right| = |U/fR| \tag{2-6}$$

where *Ro* is the "Rossby curvature number", *U* is the streamwise velocity, *R* is the flow radius of curvature, and *f* is the Coriolis parameter.

Those studies found that for narrow inlets (small inlet width, and wide reef width, comparatively) like Boca Chica, centrifugal accelerations dominate Coriolis across the inlet, indicating a cyclostrophic balance. For wide inlets (large inlet width, and small reef width, comparatively) like Boca Grande, their results show that centrifugal accelerations dominate Coriolis at the headlands (reef edges), indicating also a cyclostrophic balance; however, the balance shifts to geostrophic flow in the center of the inlet where centrifugal accelerations are weakest.

Applying Equation 2-6 to both inlets yields similar results, as presented in Figure 2-10. For Boca Chica, a narrow inlet system, a cyclostrophic balance seems to dominate the length of the inlet, but these dynamics are not influential in most of the lagoon. Boca Grande, a wide inlet system, presents cyclostrophic dynamics restricted to the inlet edges, separated by different dynamics to the north of the inlet center. The asymmetry of weaker cyclostrophic dynamics in the north versus the south is likely caused by the strength of the net alongshore flows toward the south. The results of the "Rossby curvature number" demonstrate that the numerical simulations of *Hench et al.* [2002] may also be applicable to wave-driven circulation.

However, in microtidal environments, the other terms of the momentum balance may be significant in controlling the flow. *Valle-Levinson and Guo (2009)* showed that advection and frictional effects influenced flow behavior in estuarine channels. They proposed the bottom slope as an estimate of advection to frictional dominance when compared to the coefficient of bottom drag ($C_d = 0.0025$). This ratio was applied at the two inlets. At Boca Chica, inlet depth was ~ 5 m and inlet length was ~250 m resulting in a slope of ~0.02, indicating an inertial dominance of inlet flows. At Boca Grande, inlet length was ~ 700 m with an average depth of ~5 m, producing a bottom slope of 0.007, indicating that both frictional and inertial effects contribute because the ratio is close to the canonical value of $C_d = 0.0025$. The frictional influence at Boca Grande is the likely cause of the asymmetry in inlet flow, where outflow occurs over deeper areas and inflow occurs over the shallower section (as observed in the residual flow components Figure 2-7B). Other studies have shown that the coefficient of bottom drag for rough bottoms (i.e., coral reefs) is 60-70 times higher than the canonical value of $C_d = 0.0025$ [*Lowe et al.,* 2009]. For Puerto Morelos, drag coefficients have been found to range from 0.0051 at the inlet for typical wave-driven flow conditions [*Parra et al.,* 2014] to 0.015 at the reef for storm conditions [*Coronado et al.,* 2007]. This realization suggests that although Boca Grande is likely influenced by bottom friction, Boca Chica may also have the same influence, depending on the value assigned to the bottom drag coefficient. Future work will focus on estimating the drag coefficient for the two circuit systems.

The previous dimensional comparison gives insight to the asymmetry of inlet flows at Boca Grande. To further examine the flows at the inlet based on inlet dimensions, another non-dimensional number is used. Modifying the approach of *Valle-Levinson and Guo* [2009], the bathymetry range (at the inlet) was compared to inlet length using the following relation:

$$C = \frac{\Delta H}{L} \tag{2-7}$$

where ΔH is the bathymetry range over the inlet (i.e., maximum and minimum depths of the inlet, not including the reef crest) and L is the distance across the inlet.

This simple ratio allows an initial comparison of variations in inlet behavior due to changes in bathymetry and inlet length. At Boca Chica, there is little bathymetric variation, resulting in a C = 0.0005. However, at Boca Grande C = 0.003, demonstrating that despite an increased inlet width, changes in bathymetry cause a higher C value than at Boca Chica. It is proposed that for higher C values, flows at the inlet will behave more asymmetrically. For frictionally influenced inlet systems, flows will take the path of least resistance, resulting in the strongest flows occurring over the deepest bathymetric areas.

To validate the proposed C values, dominant forcing terms are calculated for the vertically integrated horizontal momentum balance (2-4) & (2-5). At Boca Chica, the relative magnitudes of the momentum balance terms are represented as contours over the circuit area (Figure 2-11). From this depiction, it is clear that within the lagoon, bottom friction dominates with magnitudes reaching ~10^{-5} ms^{-2}. Local accelerations increase near the inlet, reaching orders of magnitude that are equivalent to frictional effects. This result suggests that local accelerations are non-negligible at the inlet. Therefore, applying only the C ratio (Equation 2-7) may still predict flow behavior in the lagoon, but may not be valid at the inlet. Advection is relatively weak in the lagoon, but dominates the other momentum balance terms across the entire length of the inlet, reaching values of ~$10^{-4}ms^{-2}$. While the influence of Coriolis is apparent in the center of the circuit, values are small in comparison with other terms (~$10^{-6}ms^{-2}$) and decrease at the inlet (~$10^{-7} ms^{-2}$). The examination of the horizontal momentum balance at Boca Chica reveals that bottom friction dominates the circuit flows, with local accelerations and advection becoming influential at the inlet.

The vertically integrated horizontal momentum balance was also applied to the Boca Grande circuit area, resulting in surprising differences. The relative magnitudes of Equations 2-4 & 2-5 for Boca Grande are presented in Tables 2-1 and 2-2 and demonstrate that advective and local accelerations compete to balance the pressure gradient throughout the lagoon, with minor influences from Coriolis and bottom friction. However, at the inlet, advection dominates the local, Coriolis, and frictional accelerations by two orders of magnitude. These results agree with the behavior predicted by the *C* value. However, they also indicate that local accelerations and nonlinear effects cannot be neglected when analyzing flow fields for wave-driven inlet systems, similar to findings of other inlet systems [e.g., *Waterhouse et al.,* 2012].

Based on the results of the momentum balance analysis, it is clear that non-linear effects (from spatial gradients in flow) dominate the flow behavior at both inlets. In addition, for both systems local accelerations increase with proximity to the inlet. To gain a spatial understanding of the dominant dynamic terms at the inlet, I propose a non-dimensional curvature number, *S*. The *S* number compares advection to local accelerations to determine the tendency toward non-linear flow behavior, analogous to the Strouhal Number (St) that describes vortex shedding oscillations. The proposed *S* number compares advective to local accelerations or inlet width to radius of flow curvature as follows:

$$S = \frac{advective}{local} = \frac{L^2/_{RT^2}}{L/_{T^2}} = \frac{L}{R} \tag{2-8}$$

where L is inlet width (meters), R is the radius of curvature with respect to the inlet edges (meters), and T is time (seconds).

Figure 2-12 demonstrates the idealized S number, for a narrow inlet system (Boca Chica) and for a wide inlet system (Boca Grande). It is clear that in both systems, nonlinear effects occur at the reef edges, similar to the results of the “Rossby curvature number”. For smaller inlet widths, these effects span the entire inlet. When S numbers are >>1 over most of the inlet, the flow will behave like a jet, with converging outflow at the inlet. However, when the inlet has high *S* numbers near the reef edges and low *S* numbers (<<1) in the center, the flow will behave non-uniformly, allowing for the formation of recirculation patterns to occur at the transition zones. To justify this claim, I compare the advective versus local accelerations for the Boca Grande inlet system in Figure 2-13. The results agree with predictions in the sense that *S* is such that advective accelerations dominate the edges of the inlet, while local accelerations appear at the center of the inlet. When the *S* number is high, flow patterns tend to be non-linear (e.g., recirculation), as indicated by the black contour line at S = 10 on a log scale. At the reef edges, nonlinearities occur due to centrifugal acceleration around the reef morphology. In addition, high *S* numbers are observed in the center and at the southwest corner of the circuit area. These regions of nonlinear behavior are confirmed upon examination of the residual flow vectors in Figure 2-6C&D. At the southwest corner, flows diverge, suggesting the dispersal of water mass. However, at the center of the circuit, the flows converge in the vortex, indicating a region that is susceptible to forming a pollutant trap.

The results of the *S* number and the advection versus local accelerations analysis have significant implications for reef health management by identifying areas of nonlinear flows that could result in increased flushing times. For instance, the residual flow patterns observed in Boca Chica suggest that the time it takes for a particle at the shore to reach the inlet is approximately 1.4 hours (Figure 2-4A). If taken symmetrically (i.e., the same time for a particle from the reef to reach the shore), this value agrees with the residence time of 3 hours calculated by *Coronado et al.,* [2007]. However, at Boca Grande particles leaving the shore could become trapped in the streamlines observed in Figure 2-4C. This could result in increased transport times from the shore to the inlet of 14.4 to over 30 hours, leading to residence times on the order of days. In addition to increased residence times, nonlinear flow behavior can reinforce development of the inlets over time. For example, Boca Grande has dynamic bathymetry that reinforces asymmetrical flows, where the strongest flows occur over the deepest bathymetric pockets. These areas of strong flows will likely impede sediment deposition as well as the formation of certain coral species. As a result, it would be expected that the asymmetric flows at Boca Grande inlet would continue to be exacerbated over time. This hypothesis was qualitatively assessed by the diver's observations of sand, hardground and sparse seagrass along the length of Boca Grande inlet. These observations highlight the absence of certain vegetation at the backreef and reef crest at Puerto Morelos, which is typically composed of 'seagrass, coral, macroalgae, sand, hardground' and 'sponges' [*Ruiz-Rentería et al.,* 1998, Table

2]. The initial observations of the absences of sponges and macroalgae suggest that inlets have remained largely uninhabited by these coral species. This reinforces the idea that reduced drag coefficients at the inlets would allow for faster flows over deeper bathymetric pockets.

Tidal and Residual Circulation Conclusions

In a fringing reef lagoon, circulation can be very different from inlet to inlet, despite geographic proximity. These differences stem from variations in tidal elevation, bathymetry, wind conditions, wave height, and inlet width. Results of two tidal cycle surveys show that tides produce spatial and temporal variability in shallow reef lagoons that should not be neglected, even in microtidal regimes. For mixed tide regions, a kinematic analysis of the flow fields can produce contrasting structures at inlets in close proximity (<1 km). The behavior of the kinematics is determined by water surface elevation (tides and waves). Comparing the tidal range to H_s can determine the relative influence of the tides. For high ratios of tidal range to H_s, flow kinematics exhibit intratidal variations. Conversely, low ratios of tides to H_s result in low intratidal variability. During high H_s conditions, the strength of the wave-driven circulation increases, reducing flushing times. In addition, semidiurnal (M2) tides generate the M4 overtide, which also influences the kinematic behavior. For mixed tides with lower significant wave heights, the kinematics can behave diurnally, resulting in a cycle period that is twice that of the semidiurnal kinematics.

Bathymetry and inlet width must also be considered when analyzing flow patterns at reef breaks. Increases in inlet width and variation in its bathymetric structure will cause relatively more complex residual flow structures at the inlet. In some cases, inflow can overcome the favored seaward flow and recirculation patterns may develop.

The findings of this study slightly modify the paradigm on circulation patterns in shallow reef systems. They highlight the asymmetry of inlet flows, identifying residual inflow that results in gyre formation, and suggesting that flushing in these systems may not be as expedient as previously expected. Furthermore, a simple approach was proposed to determine whether an inlet system is susceptible to recirculation by comparing inlet length to local radius of curvature as a proxy comparison for advection to local accelerations. While these results are only reliable near the inlet, they present a means of initial identification of inlet systems that may be susceptible to gyre formation. Nonlinearities within the lagoon-inlet system can further be identified through a direct comparison of advection to local accelerations. This comparison identifies areas in the lagoon associated with flow recirculation. The results of this study have implications for reef health management and sustainability in the form of predicting pollutant and nutrient traps as well as identifying areas of higher flushing times.

Table 2-1. BG Momentum Balance (U) Magnitudes (10^X ms^{-2})

	Leg of Transect	Local	Advection	Coriolis	Bottom Friction	Pressure Gradient
U (East-West)	1	-6	-6 to -7	-7	-7	-6
	2	-6	-4 to -5	-6 to -7	-6 to -7	-6
	3	-6	-6	-6 to -7	-6 to -7	-6
	4	-6	-6 to -7	-6 to -7	-6 to -7	-6

Table 2-2. BG Momentum Balance (V) Magnitudes (10^X ms^{-2})

	Leg of Transect	Local	Advection	Coriolis	Bottom Friction	Pressure Gradient
V (North-South)	1	-6	-6 to -7	-7	-7	-6
	2	-6	-4 to -5	-6 to -7	-6 to -7	-6
	3	-6	-6 to -7	-6 to -7	-6 to -7	-6
	4	-6	-6	-6 to -7	-6 to -7	-6

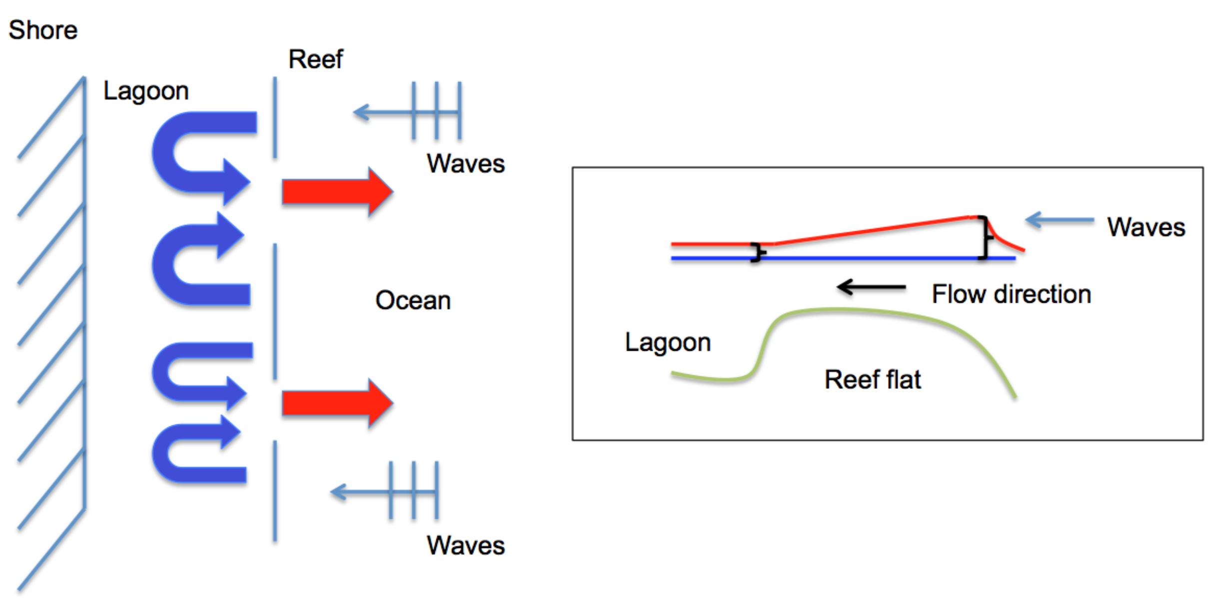

Figure 2-1. Schematic of wave-driven circulation. Top view (left), Side view (right). Inflow into the system is caused by waves breaking over the reef, creating set up induced pressure gradient that drives outflow through the reef breaks.

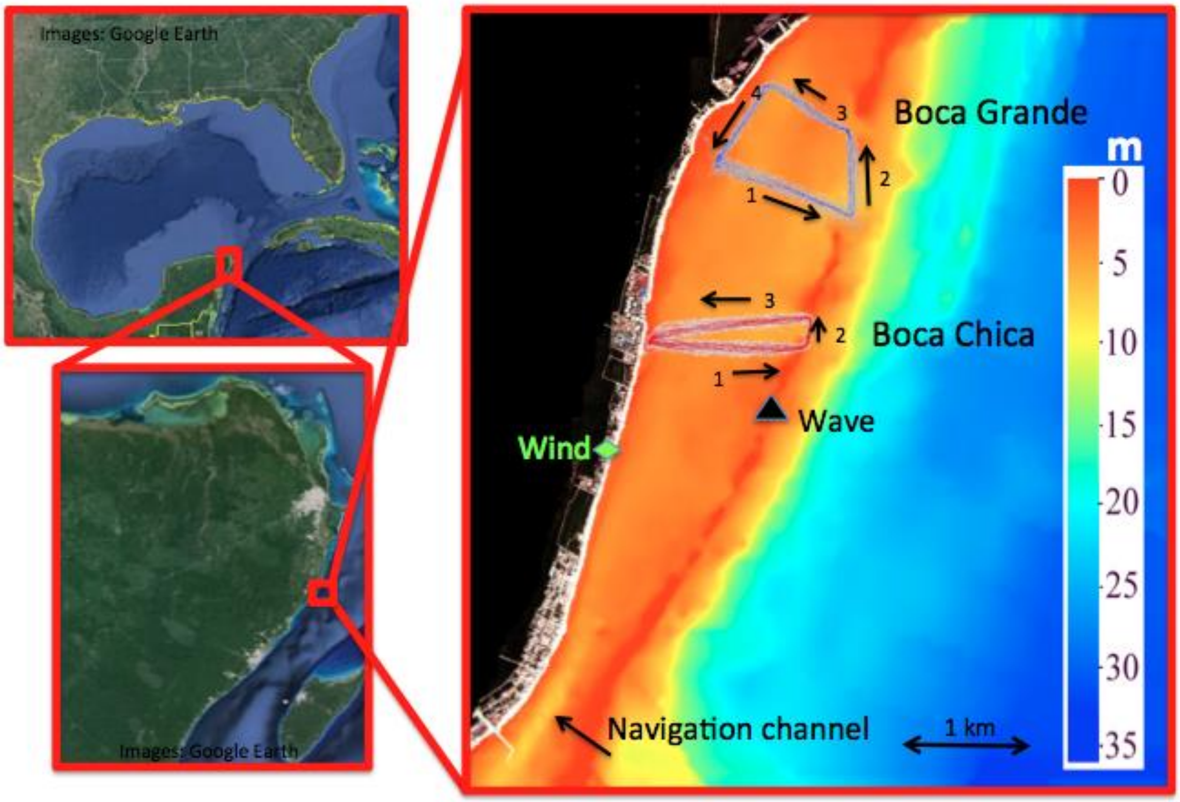

Figure 2-2. Site Location: Puerto Morelos, Quintana Roo, Mexico. The Puerto Morelos fringing reef is located on the NE coast of the Yucatan peninsula. There are two inlets: Boca Grande to the north and Boca Chica in the center of the reef. A navigation channel is located at the southern end of the lagoon. Circuit area transects of the towed ADCP paths are shown in the bathymetric map. Wave data were collected from a moored Aquadopp on the fore-reef (black triangle). Wind data were obtained from UNAM (green diamond).

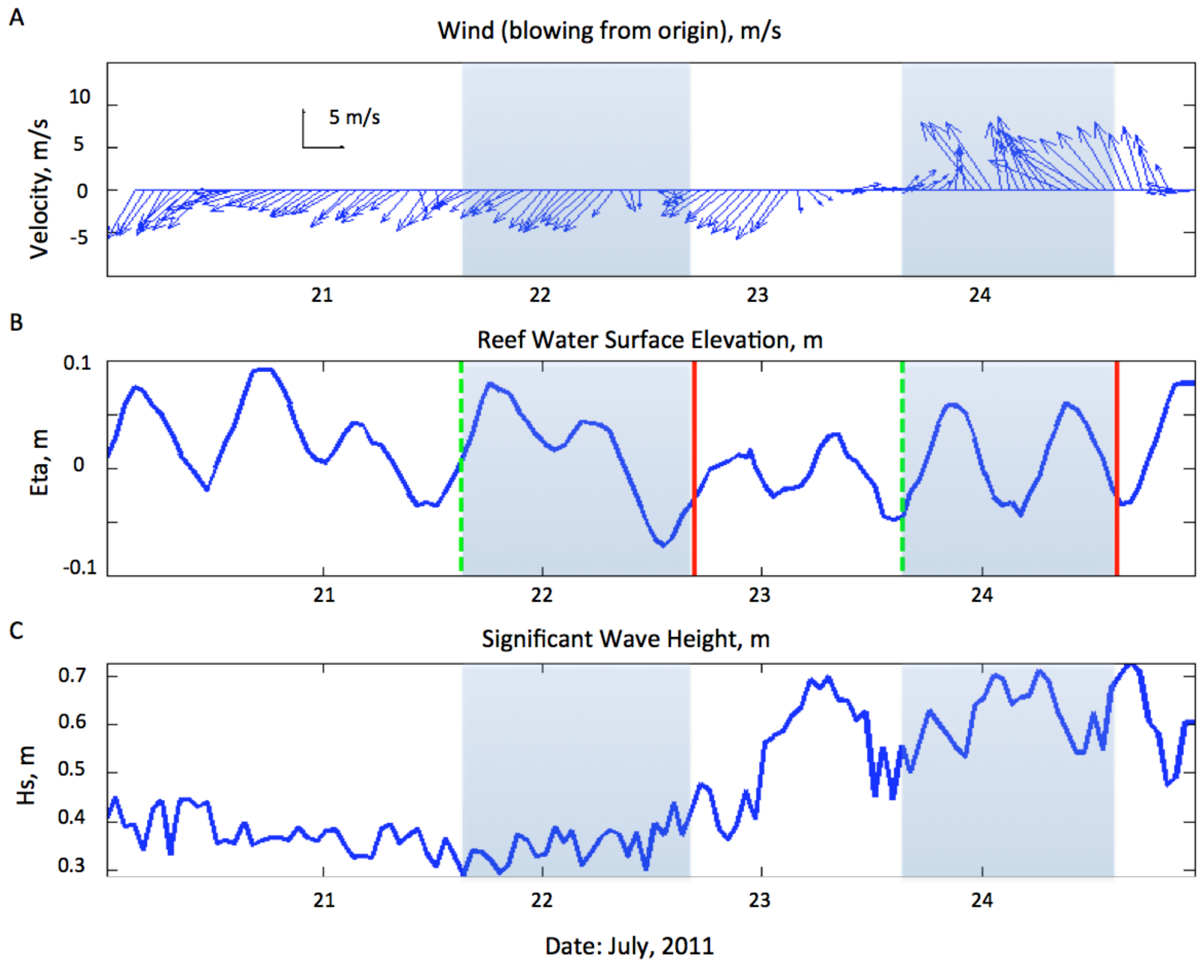

Figure 2-3. Atmospheric and oceanic forcing conditions during the experiment. A) Prevailing winds (origin), B) Water surface elevation (at the fore-reef wave data location) C) Significant wave height (calculated from the fore-reef wave data). The start of the experiment (green dashed line) and end of the experiment (red line) are indicated above. The shaded boxes highlight the conditions during each experiment. Boca Chica transects occurred from July 21-22, 2014 and Boca Grande transects occurred from July 23-24, 2014.

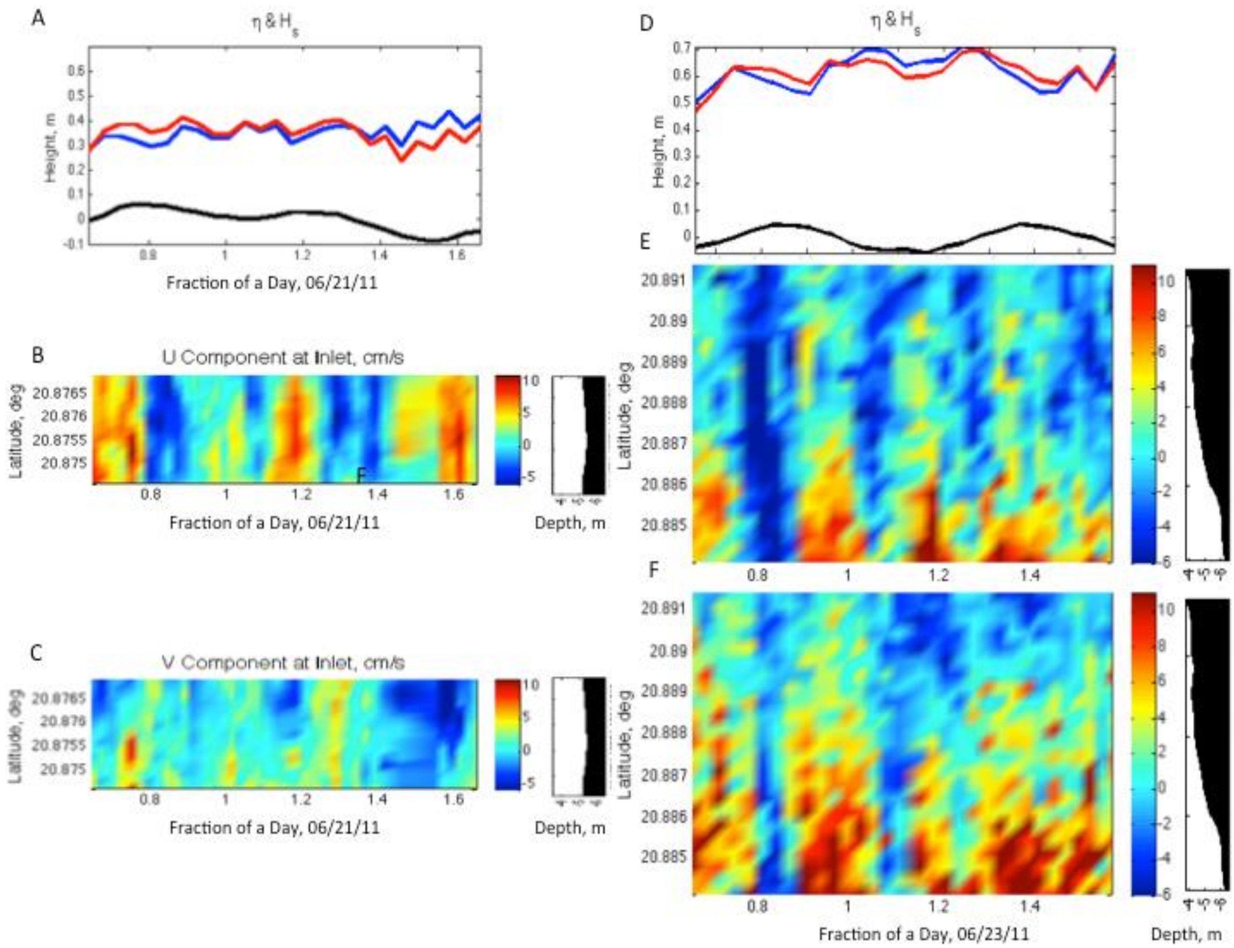

Figure 2-4. Depth averaged spatial and temporal comparison of inlet flows. Left side: Boca Chica data: A) Water surface elevations with reference to significant wave height and tidal range are presented as: the tidal elevation, eta, (black line), significant wave height (blue), and sum of the two elevations (red line). B) U component of velocity with respect to distance across the inlet and bathymetry. The color contours represent eastward outflow (positive) and westward inflow (negative). C) V component of velocity with respect to distance across the inlet and bathymetry. The color contours represent northward (positive) and southward (negative) flows. Right side: Boca Grande data: D) Water surface elevations with reference to significant wave height and tidal range are presented as: the tidal elevation, eta, (black line), significant wave height (blue), and sum of the two elevations (red line). E) U component of velocity with respect to distance across the inlet and bathymetry. The color contours represent eastward outflow (positive) and westward inflow (negative). F) V component of velocity with respect to distance across the inlet and bathymetry. The color contours represent northward (positive) and southward (negative) flows.

A B C D E F

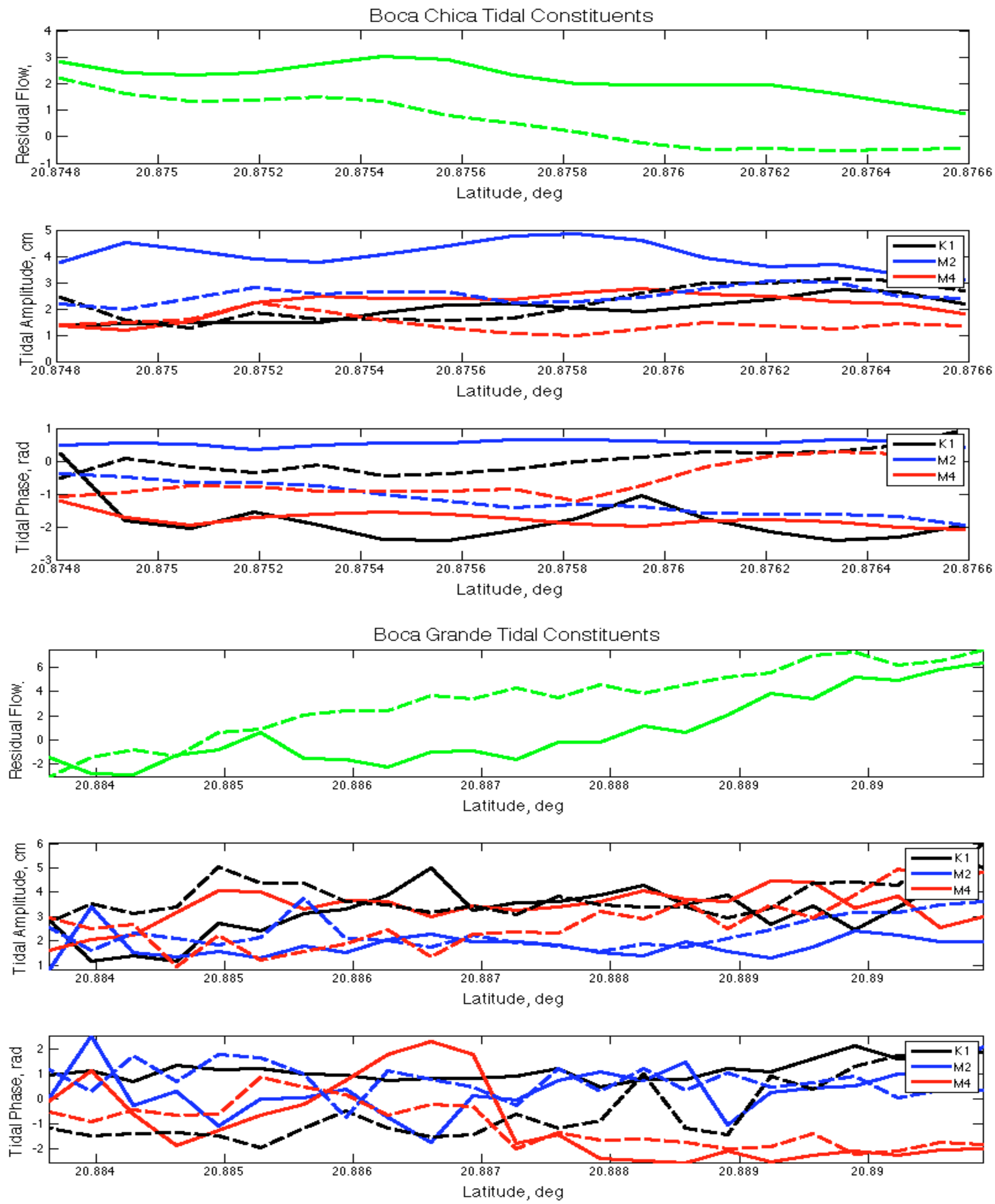

Figure 2-5. Depth averaged residual and tidal flow constituents at the inlets. The solid lines indicate the U component and the dashed lines indicate the V component. A) Boca Chica residual flow, cm/s B) Boca Chica tidal amplitude (cm) with respect to tidal harmonics: K1, M2 & M4. C) Boca Chica tidal phase (rad) with respect to tidal harmonics: K1, M2 & M4. D) Boca Grande residual flow, cm/s B) Boca Grande tidal amplitude (cm) with respect to tidal harmonics: K1, M2 & M4. C) Boca Grande tidal phase (rad) with respect to tidal harmonics: K1, M2 & M4.

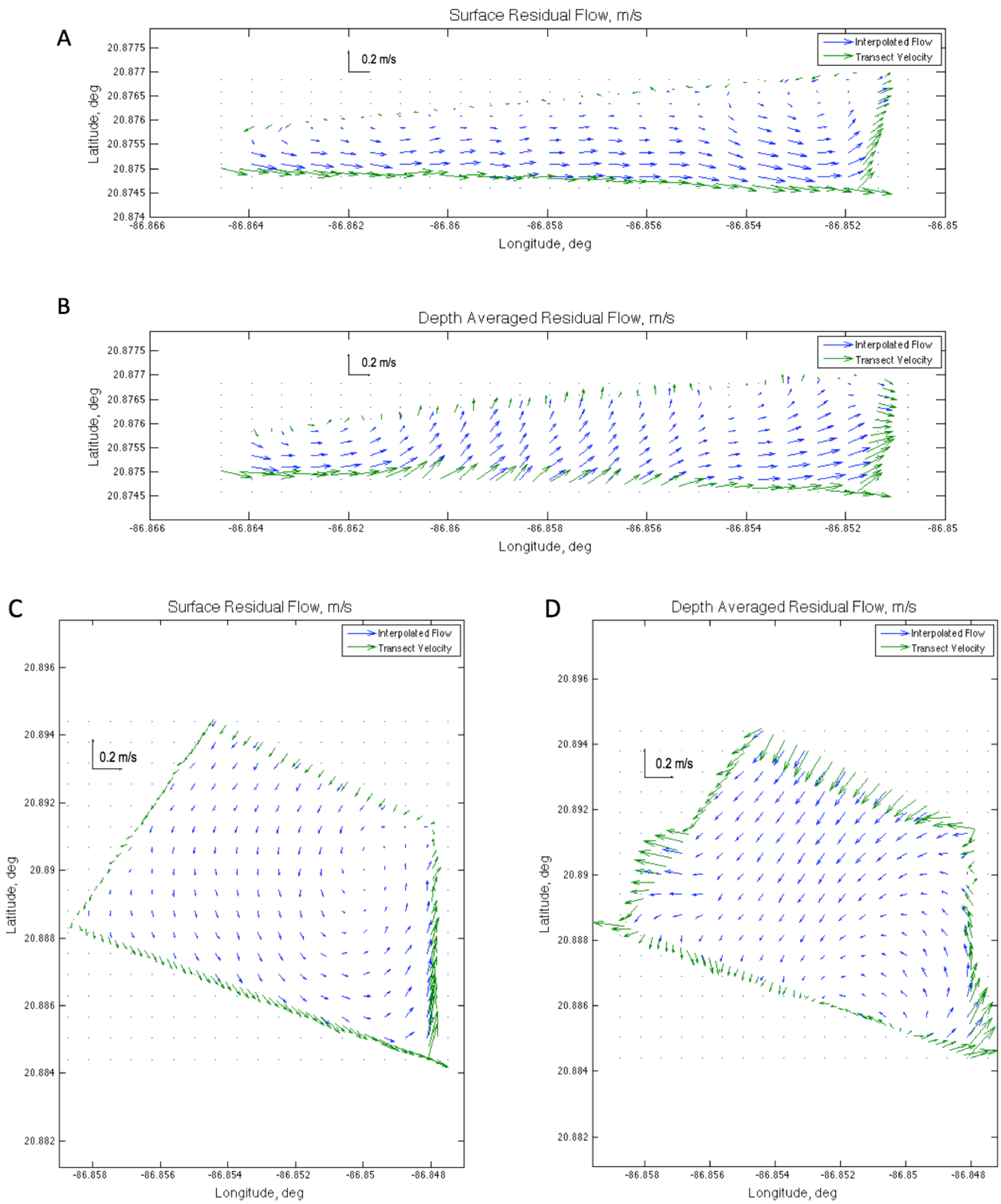

Figure 2-6. Surface and depth averaged spatial residual flows. A-B) Boca Chica Inlet flow fields, surface and depth averaged respectively. C-D) Boca Grande Inlet flow fields, surface and depth averaged respectively.

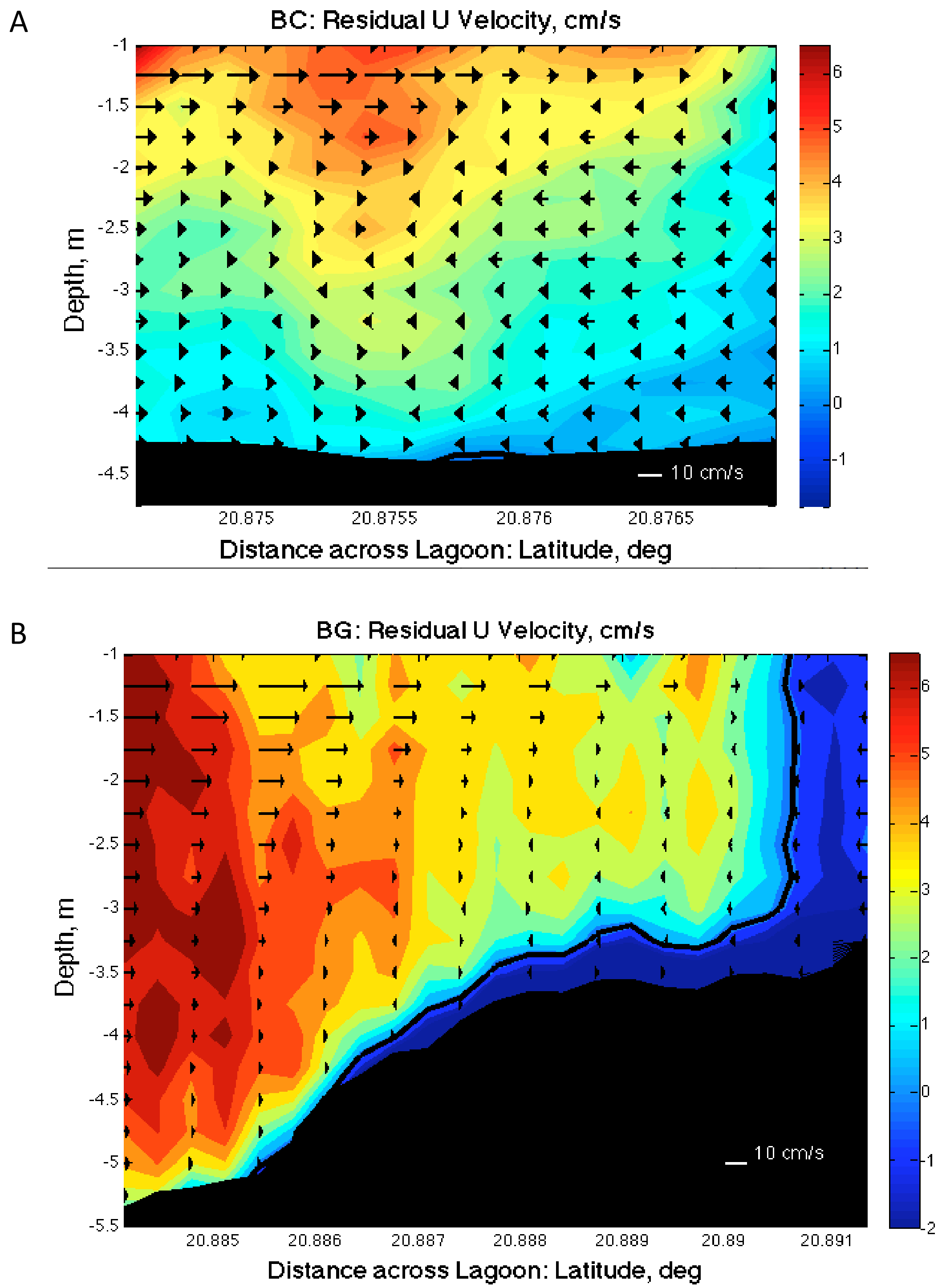

Figure 2-7. Residual flows at the inlets with respect to depth. Contours represent the East-West component of flow, where positive values (red) indicate eastward, outflow and negative values (blue) indicate westward inflow. Vectors (black) represent the North-South component of flow, rightward pointing indicates northward flow, leftward pointing indicates southward flow. A) Boca Chica and B) Boca Grande

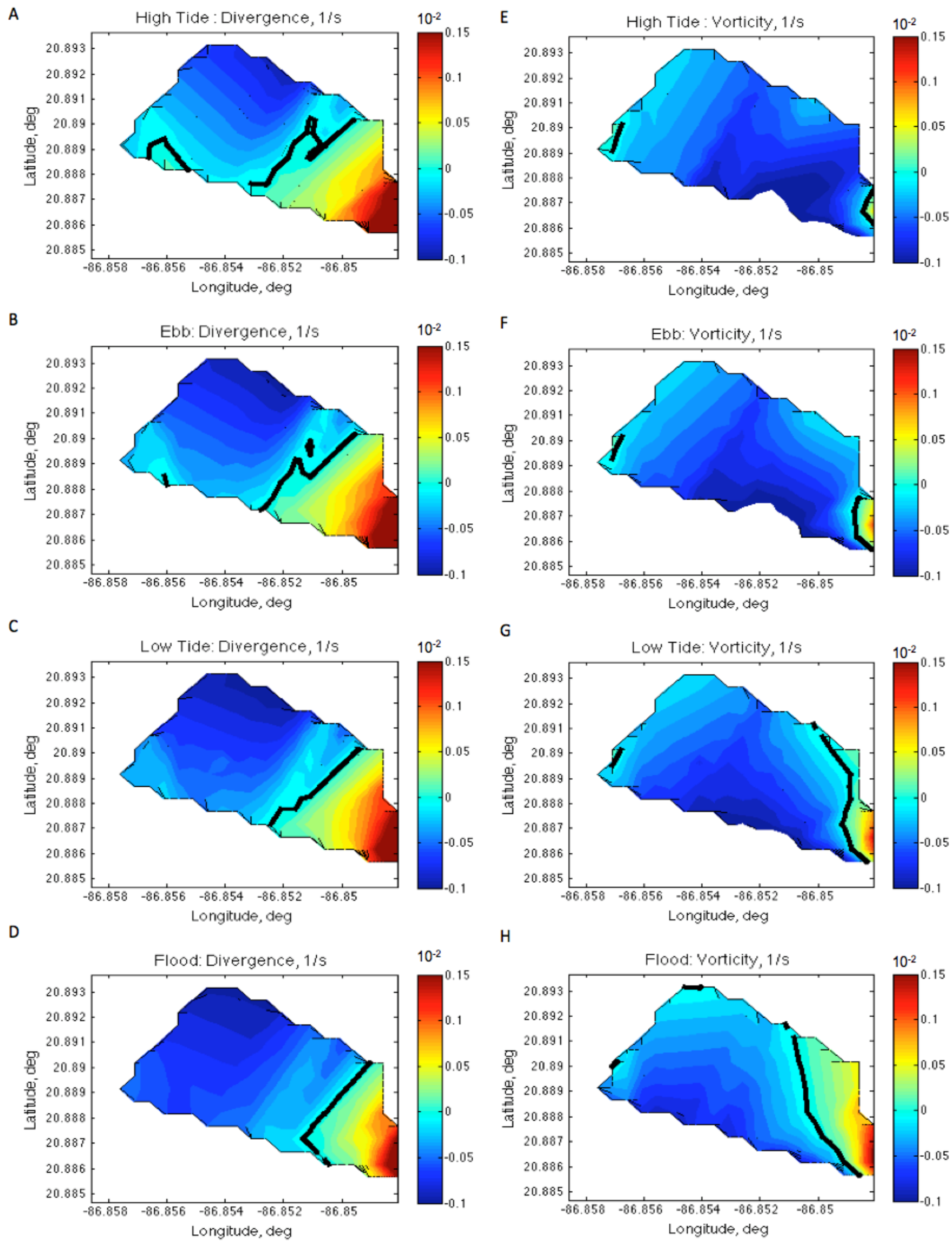

Figure 2-8. Boca Grande: Tidal evolution of horizontal divergence and vertical component of relative vorticity. A-D) Represents divergence values during the semidiurnal tidal cycle: high tide, ebb tide, low tide, and flood tide, respectively. Positive values indicate diverging flows, negative values are converging flows. E-H) Represents relative vorticity values during the semidiurnal tidal cycle: high tide, ebb tide, low tide, and flood tide, respectively. Positive values indicate counter-rotating flows, negative values are clockwise rotating flows. Highest values of divergence and vorticity are observed at the inlet.

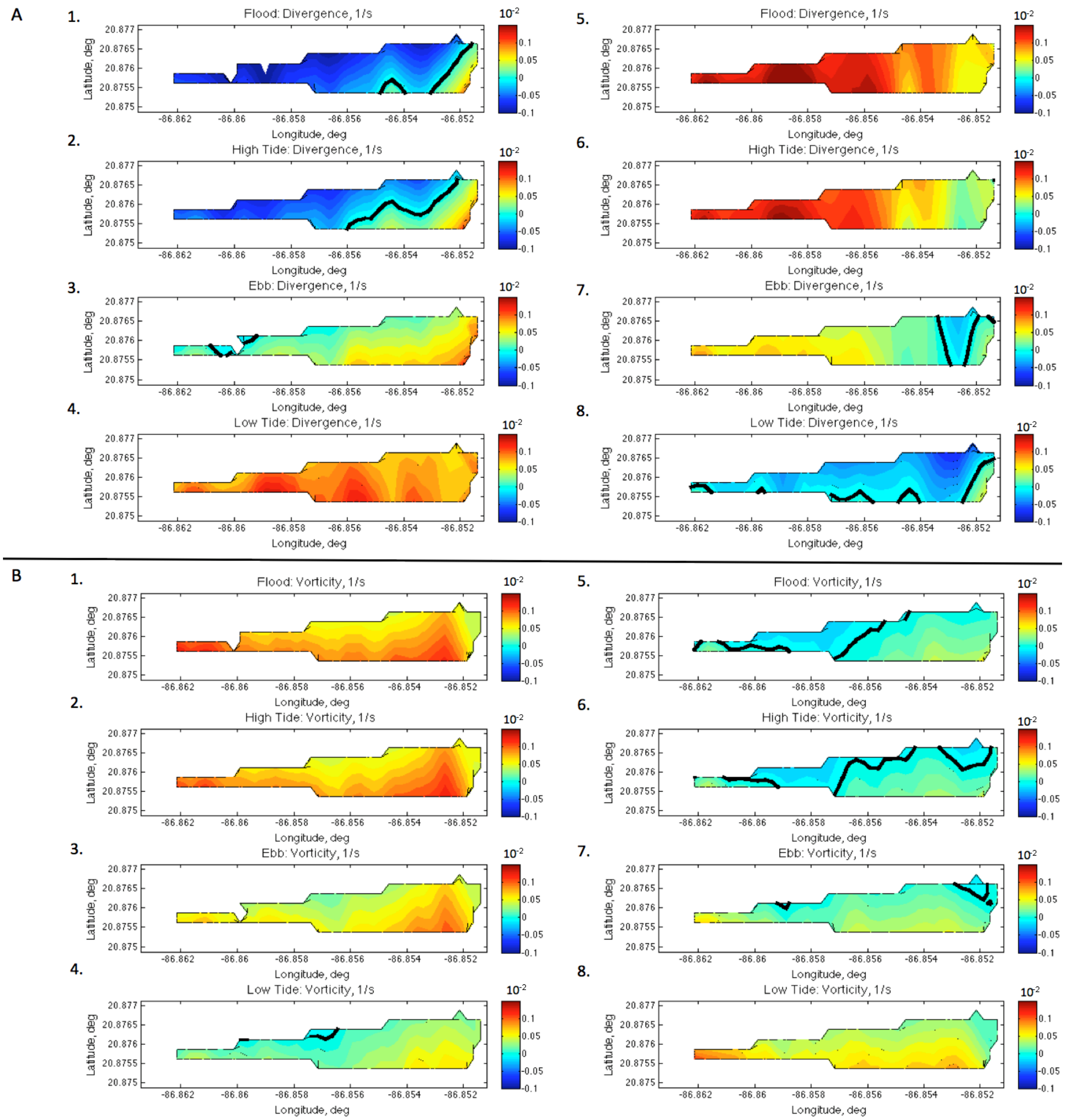

Figure 2-9. Boca Chica: Tidal evolution of horizontal divergence and vertical component of relative vorticity. A) Represents divergence values during the first semidiurnal tidal cycle (1-4): flood, high, ebb, and low tides, respectively, and during the second semidiurnal tidal cycle (5-8): flood, high, ebb, and low tides, respectively. Positive values indicate diverging flows, negative values are converging flows. E-H) Represents relative vorticity values during the first semidiurnal tidal cycle (1-4): flood, high, ebb, and low tides, respectively, and during the second semidiurnal tidal cycle (5-8): flood, high, ebb, and low tides, respectively. Positive values indicate counter-rotating flows, negative values are clockwise rotating flows.

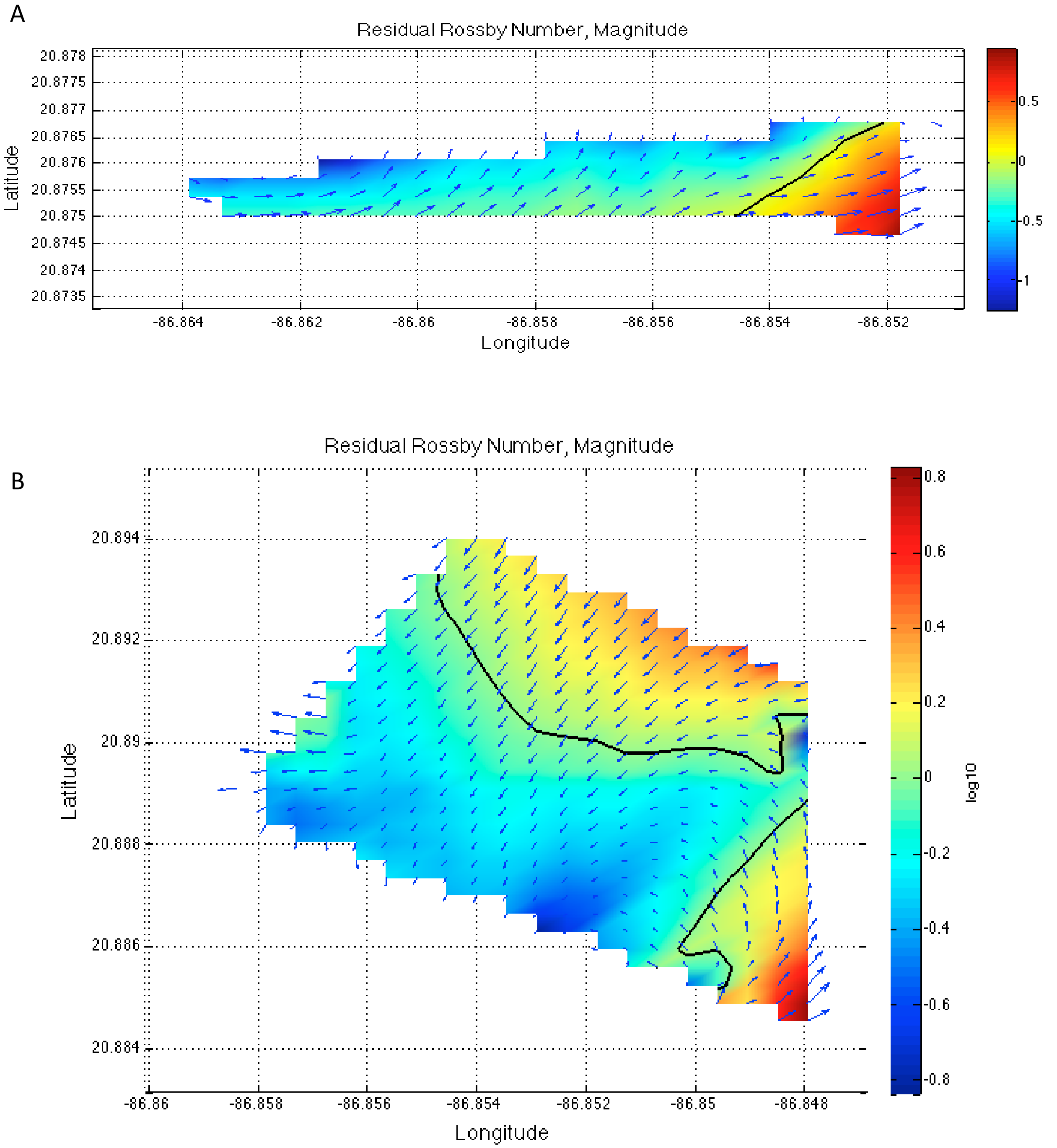

Figure 2-10. Spatial maps of the Rossby curvature number. Contours represent the Ro number on a log10 scale. Positive values indicate a cyclostropic balance with the pressure gradient and negative values indicate geostrophy. The black line represents Ro = 1. Vectors indicate the residual depth averaged flow fields for A) Boca Chica and B) Boca Grande.

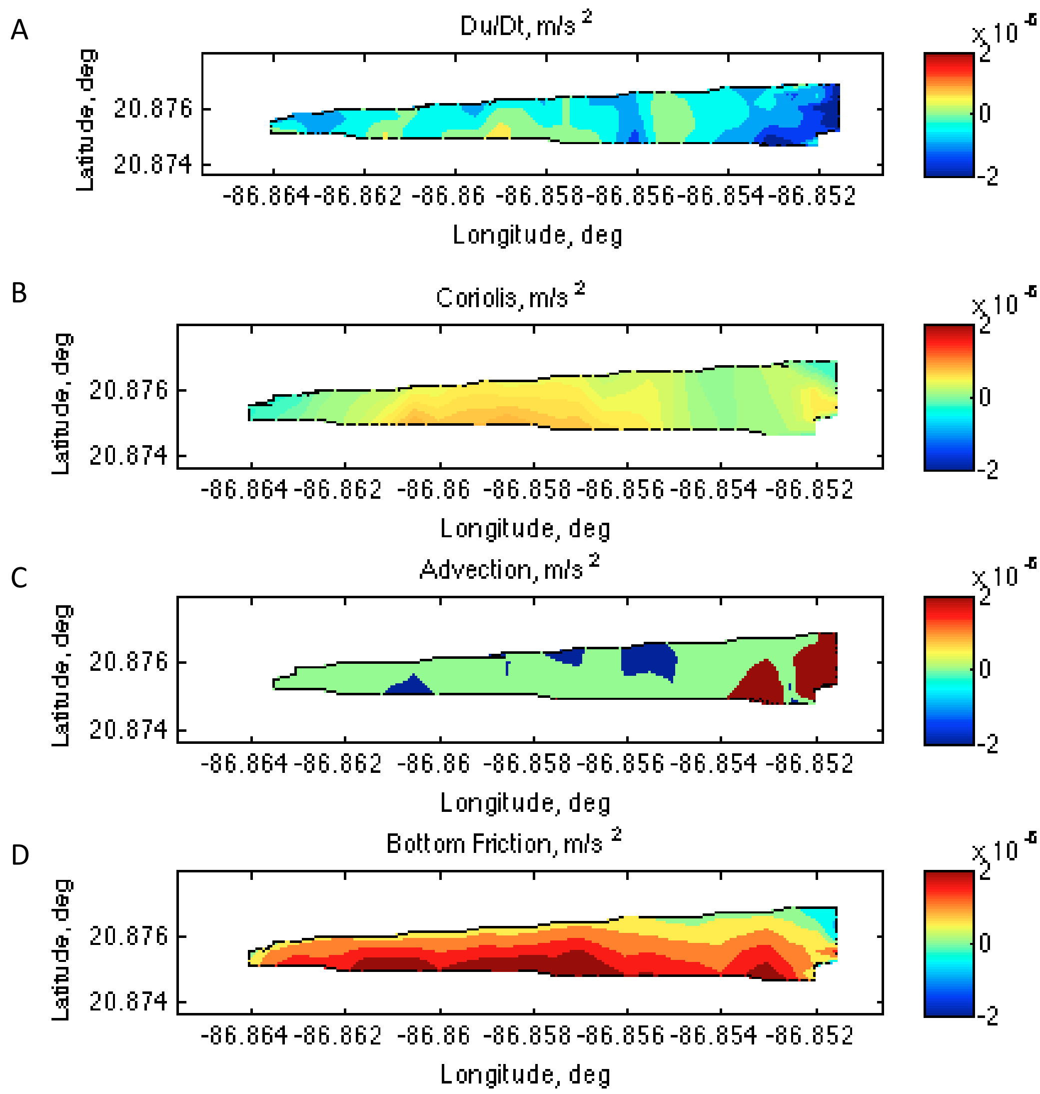

Figure 2-11. Spatial contours of horizontal momentum balance terms at Boca Chica. A) Local acceleration B) Coriolis acceleration C) Advective acceleration D) Deceleration due to bottom friction. All terms have units of acceleration (ms^{-2}).

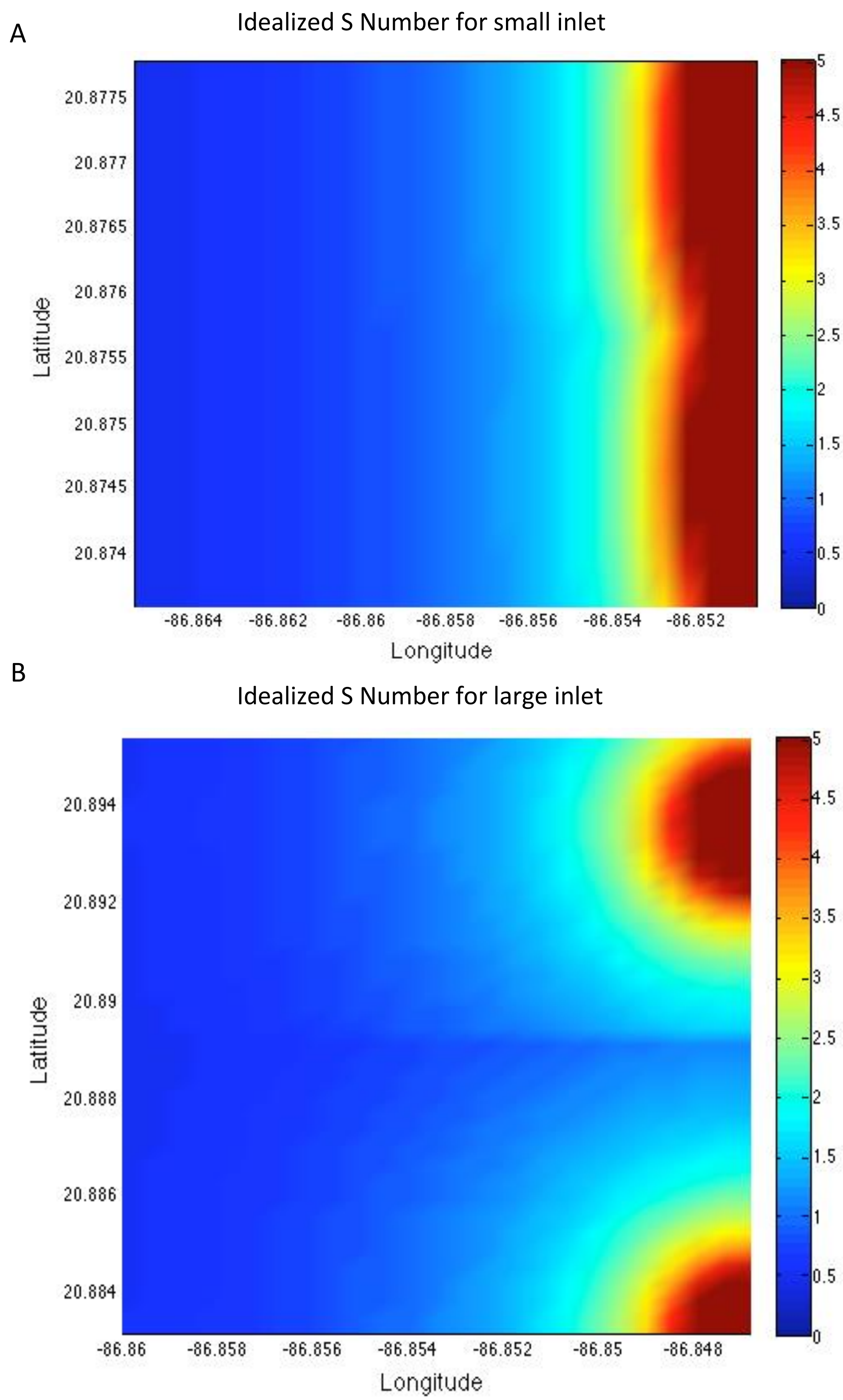

Figure 2-12. Idealized S curvature number: Comparing inlet length to spatial radius of flow curvature map with respect to inlet reef edges. Contours represent S values, where S>1 indicates non-linear (advective) dominance over local accelerations for A) Boca Chica and B) Boca Grande

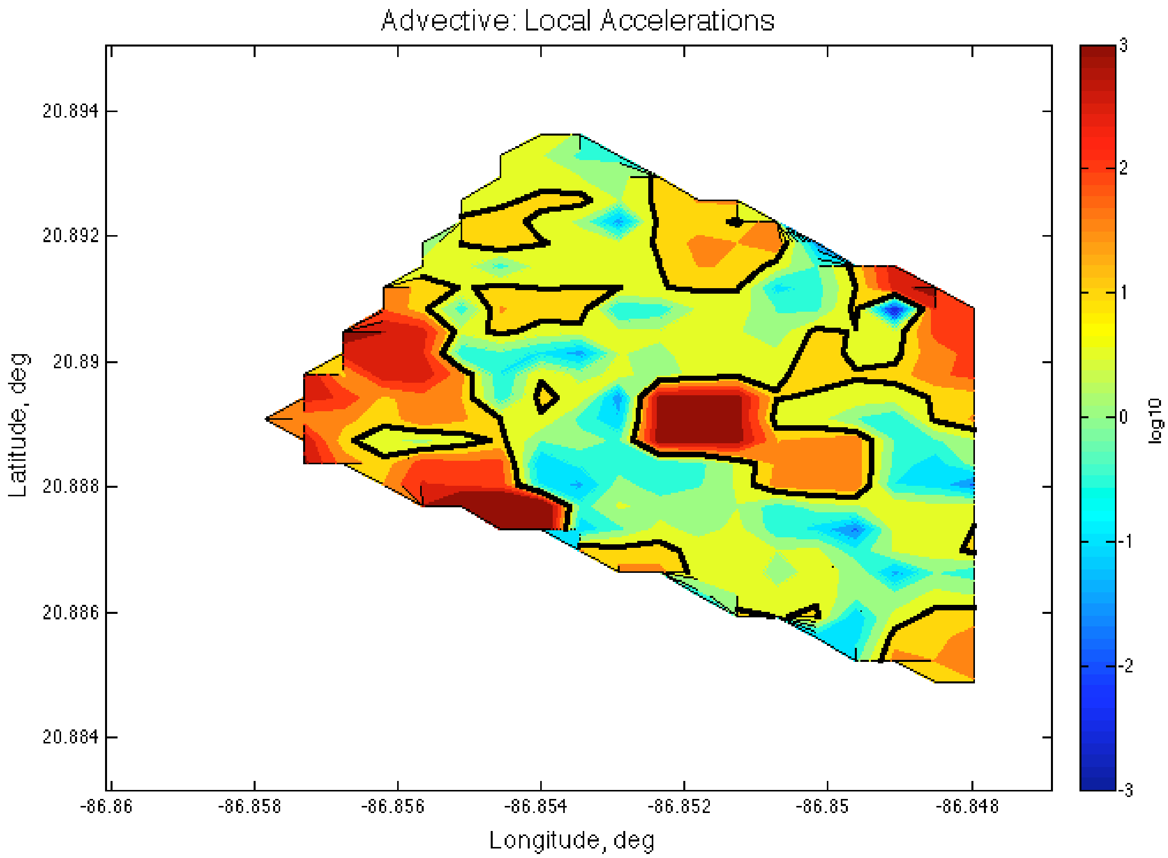

Figure 2-13. Boca Grande spatial map comparing Advective versus Local Accelerations. Contours represent S values, where log10(S) >1 indicates strong non-linear (advective) dominance over local accelerations. At the inlet, results support the S curvature number predictions with high nonlinearities at the reef edges. Other high values are observed at Lat, Lon (20.89, -86.857) and Lat, Lon (20.889, -86.852). This method identifies areas of high nonlinear flow behavior, which could indicate flow dispersal or recirculation.

CHAPTER 3
SUBMARINE GROUNDWATER DISCHARGE AND TURBULENCE BEHAVIOR

Introduction to SGD and Turbulence

Background

Submarine groundwater discharge (SGD) has become widely recognized as a critical connection between groundwater resources and the sea, playing a significant role in the global budget of dissolved materials [*Moore,* 1996; *Santos et al.,* 2008; *Valle Levinson et al.*, 2011]. Research has shown that SGDs can vary from slow diffusive fluxes (~ cm/day) through bed sediment seepage [*Paulsen et al.,* 2007; *Martin et al.,* 2007] to rapid fluxes (~1 m/s) at point sources [*Valle Levinson et al.,* 2011]. Diffusive SGDs typically occur through low-permeability media (sandy seabeds), while point SGDs are associated with highly permeable karst topography [*Burnett,* 2006; *Valle Levinson et al.,* 2011]. Although seepage sources may provide more flux by volume to the global budget, point sources, such as submarine springs, establish a rapid response relationship between groundwater resources and the ocean [*Valle Levinson et al.,* 2011; *Parra et al.,* 2014].

In coastal karst aquifers, point SGD sources are formed over time from the dissolution of limestone that creates a complex groundwater matrix of subterranean conduits [*Valle Levinson et al.,* 2011; *Parra et al.,* 2014]. In unconfined karst topography, like the Yucatan peninsula, meteoric surface water drains to subterranean cave systems *[Kaufmann,* 1999], as indicated by the absence of rivers [*Beddows et al.,* 2007]. The lack of surface water resources and the direct connection between subterranean freshwater resources and the sea makes these karst conduit systems particularly vulnerable to threats of sea level rise, pollution, and depleting water resources due to increased consumption [*Parra et al.,* 2014].

Recently, studies have made an effort to understand the hydrologic characteristics of SGDs at springs [*Peterson et al.,* 2009; *Valle-Levinson et al.,* 2011; *Exposito-Diaz et al.,* 2013; *Parra et al.,* 2014]. In these systems, the piezometric pressure heads of the inland water table and the sea surface determine water table elevation and control SGD [*Valle Levinson et al.,* 2011]. The change in sea surface elevation due to tides, wind, waves, storm surge, and set-up have been shown to modulate spring discharge based on a relative pressure (hydraulic head) gradient [*Li et al.,* 1999; *Kim and Hwang*, 2002; *Taniguchi,* 2002; *Valle Levinson et al.,* 2011; *Vera et al.,* 2012; *Parra et al.,* 2014]. When the pressure gradient between inland groundwater and the sea surface is largest, spring discharge will be greatest. When the gradient becomes less or reverses in direction, SGDs become weaker and more sensitive to even slight changes in mean sea level. Previous studies [e.g., *Valle-Levinson et al.,* 2011; *Parra et al.,* 2013] have observed that in shallow estuaries in the Yucatan peninsula, an increase in sea level can even lead to reversal of spring flow, causing salt water intrusion into the aquifer. To protect groundwater resources, it is crucial to understand the discharge behavior of the system in order to predict how it will respond in the future. This study analyzes the turbulence structure of spring flow to address this issue. Turbulence from submarine springs can enhance mixing in the water column, which influences nutrient, pollutant, and sediment transports and concentrations, impacting the health of the ecosystem.

Progress has been made in understanding turbulence in energetic tidal channels [*Rippeth et al.,* 2001; *Souza et al.,* 2004; *Thomson et al.,* 2010; *McCaffrey et al.,* 2014], and over the continental shelf [*Vermeulen, et al.,* 2011; *Palmer et al.,* 2014]. But relatively few studies have focused on turbulence of SGDs [*Peterson et al.,* 2009; *Exposito-Diaz et al.,* 2013; *Parra et al.,* 2014]. Based on previous work, the maximum values of turbulent kinetic energy (TKE), turbulence dissipation [*Parra et al.,* 2014], and turbulence production [*Exposito-Diaz et al.,* 2013] are expected to occur during low tide when the discharge and vertical velocity are at maxima. Studies at submarine springs have shown that turbulence depends on discharge intensity and the lunar tides [*Exposito-Diaz et al.,* 2013; *Parra et al.,* 2014]. However, these studies were limited in their data resolution (≤4 Hz sampling rate) and time series (~4 days). Longer studies (+10 days) have addressed fortnightly variability in seepage and point SGDs [*Kim and Hwang,* 2002; *Taniguchi,* 2002] and TKE [*Parra et al.,* 2015], but have not examined the variability of turbulence dissipation rates.

The objective of this paper is to use high-temporal resolution velocities (64 Hz) to characterize and compare turbulence and SGDs at two different point sources in close proximity (< 200m) in a fringing reef lagoon. Data collected over a distinct wet period and dry period allow interpretation of seasonal variability, as well as variability in the spring-neap tidal cycles. First, hydrographic characteristics of velocity, pressure, and temperature are analyzed for trends. Then, observations of turbulence behavior are used to classify the flow structure of the submarine springs. Finally, a method is proposed for predicting TKE dissipation rates and the work of *Parra et al.* [2014] is extended by improving SGD estimates in a karst conduit flow analysis.

Site Description

This study was conducted in the lagoon of a fringing coral reef in Puerto Morelos, Quintana Roo, Mexico (Figure 3-1), located on the northeastern coast of the Yucatan peninsula. The fringing reef at Puerto Morelos is approximately 4 km in length along the coast and creates lagoon that varies in width from 500 to 1,500 m (Figure 3-1A). The shallow (3-4 m average depth) lagoon exchanges flow with the ocean via two inlets (north and center of the reef) and a navigation channel to the south. The northern inlet is ~1,200 m wide and 6 m deep; the central inlet is ~300 m wide and 6 m deep; and the navigation channel is ~400m wide and 8m deep. Roughly 10 km offshore, the shelf edge drops to >400 m [*Ruiz-Renteria et al.,* 1998]. The reef provides a unique habitat for coral and marine life, as well as necessary shore protection by dissipating wave energy from deep-water waves. Tides in this region are microtidal with ranges <0.4 m and mixed, mainly semidiurnal with a form factor ~ 0.34. Easterly Trade Winds (typically 4-10 m/s) generate waves with an annual significant wave height of 0.8 m and a typical period of 7 seconds [*Coronado et al.,* 2007]. Circulation in this microtidal region is driven by setup caused by waves breaking over the reef, with inflow occurring over the reef and outflow occurring at the inlets [*Coronado et al.,* 2007]. The wave-driven circulation results in strongest flows occurring at the inlet (~0.7 ms^{-1} outflow) [*Chapter 2*] and a well-mixed water column.

The geology of the study area is dominated by highly permeable and soluble limestone. As a result, regional rainfall of 1,300 mm per year [*Valle-Levinson et al.,* 2011] quickly percolates into the aquifer, creating a complex maze of conduits. The head difference between the inland water table and ocean surface drives flows toward the ocean, resulting in SGDs in the form of bed seepage and point sources [*Valle-*

Levinson et al., 2011; *Null et al.,* 2014]. Puerto Morelos has numerous (10-15 identified) point source springs [*Parra et al.,* 2015] that discharge into the lagoon, allowing brackish water (~22 g/kg) to mix with lagoon water (36 g/kg). The submarine springs dominate seepage sources as the main contributor to SGD in the lagoon, accounting for roughly 79% of the total SGD [*Null et al.,* 2014].

Climate in the Yucatan peninsula is characterized by a distinct dry period from March through June and a wet period from July through October [*Parra et al.,* 2014]. During the dry period, SGD is expected to be less intense and therefore susceptible to saltwater intrusion, as a result of the decrease in hydraulic head inland due to lack of rain and recharge. However, even during the wet period when discharge should be strongest, reversals in SGDs have been observed at Pargos spring by *Parra et al.* [2015]. These results suggest that Pargos spring will be especially susceptible to salt water intrusion during the dry period, which is validated in this study.

In addition to salt intrusion, these occurrences of flow reversals (back flow events) may have significant implications on conduit dissolution and nutrient fluxes in the spring system. Previous work has shown that during flow reversals observed at a karst spring system, floodwaters were able to dissolve ‘3.4 mm of the conduit wall rock’ [*Gulley et al.,* 2011, pg. 1]. The intrusion of lagoon water can also change the chemical composition of the subterranean waters by introducing dissolved oxygen and organic carbon into the aquifer water, altering the energy sources in the conduit ecosystems [*Gulley et al.,* 2011]. The implications of flow reversals are realized in previous observations of salt intrusion, conduit enlargement, and changes in chemical composition, signifying the need to understand and monitor these events.

The experiment focuses in two springs in the Puerto Morelos lagoon: Pargos and Gorgos (Figure 3-1). Pargos spring is located ~1,200 m west of the central inlet and ~300m from the shore and has an estimated discharge of 0.4 m^3s^{-1} [*Parra et al.,* 2014]. Pargos spring is an irregularly shaped vent opening with an area of ~1.5 m^2 that is located in a protected bathymetric pocket at ~1.5m below the lagoon bed (depth ~6.5m). Gorgos spring is located ~200 m southeast of Pargos and has not been previously studied. The opening at Gorgos is ~0.85 m^2 and is located on the lagoon bed (depth ~7m), exposed to influence of dominating across lagoon flows (averaging ~0.4 ms^{-1}) due to the proximity of the central inlet (outflow) [Chapter 2].

Methodology

Data Collection

To study the fortnightly variation of SGDs and turbulence characteristics at submarine springs, a 6 MHz Nortek Vector acoustic Doppler velocimeter (ADV) sampling at 64 Hz was secured at the center of the vents at Pargos and Gorgos over a spring and neap tide period. Data for Pargos were collected during the dry period (March 22-April 2, 2014) and data for Gorgos were collected during the following wet season (September 5-17, 2014). In both collection deployments, the ADV recorded 38,400 measurements (10 minute bursts) of velocity (*u, v, w*) and pressure every half hour. This sampling scheme allowed recording of high-frequency fluctuations while maintaining sufficient memory and power over the fortnightly tidal cycle. The scheme also permitted elucidation of the minimum sampling frequency to capture the full frequency range in the inertial subrange of turbulence dissipation. These experiments provided the highest temporal resolution of velocity data for Yucatan peninsula submarine springs to date.

Wind data (2 min. averaged, every 10 min.) were collected at a meteorological station located on a pier at the National Autonomous University of Mexico (UNAM), approximately 1 km southwest of the springs. Data were obtained for the month of March 2014 and September 2014, to coincide with the period of ADV measurements.

Data Analysis

Pressure data were analyzed using a fast Fourier transform (FFT) applied to each 10-minute burst of ADV data to obtain the power spectra of the water surface elevation (WSE), η. The significant wave height was then calculated using the equation:

$$H_s = 4\sqrt{\sigma_p} \tag{3-1}$$

where s_p is standard deviation of the spectra.

For each 10-minute burst, velocity components (*u, v, w*) were separated into the mean ($\bar{u}$) and fluctuation (u') components through Reynolds decomposition as follows:

$$u = \overline{u} + u' \tag{3-2}$$

where $u = u\mathbf{i} + v\mathbf{j} + w\mathbf{k}$ represents the horizontal velocities toward the east as **i**, toward the north as **j**, and the vertical velocities as **k**. The fluctuations were used to calculate the components of the Reynold's stress tensor for both shear stresses (*u'v', u'w', v'w'*) and normal stresses (*u'u', v'v', w'w'*). To evaluate the turbulence behavior at the springs, components of the Reynold's stress tensor were used to estimate values of turbulence intensity (I), turbulent kinetic energy (TKE), and coherent turbulent kinetic energy (CTKE).

Turbulence Intensity (I) is the ratio of the standard deviation of the velocity relative to the mean and is commonly used in meteorological turbulence classification

[*McCaffrey et al.,* 2014]. Following methods by *Thomson et al.* [2010], we calculated I as follows:

$$I = \frac{\sqrt{\langle u'^2 \rangle - n^2}}{\langle u \rangle} \tag{3-3}$$

where for each 10-minute burst, $\left\langle u'^2 \right\rangle$ is the mean variance of the velocity components (u, v, w), $\left\langle u \right\rangle$ is the mean velocity, and n^2 is the squared Doppler noise for the Nortek ADV. Following *Thomson et al.* [2010], bursts were ensemble averaged to reduce n to 0.0009 m/s. Turbulence intensity examines each component of the velocity vector to highlight behavior of component fluctuations. This metric is especially useful for turbulence field classification at submarine springs that have varying vent morphology.

Coherent turbulent kinetic energy (CTKE) is another useful metric to analyze the shear tendencies of the flow. CTKE represents the magnitude of the Reynolds shear stresses and is estimated by the following [*McCaffrey et al.,* 2014]:

$$CTKE = \frac{1}{2}\sqrt{(u'v')^2 + (v'w')^2 + (u'w')^2} \tag{3-4}$$

Unlike I, which accounts for one component of velocity, CTKE captures the instances when peaks occur in multiple velocity components through the use of cross terms [*McCaffrey et al.,* 2014].

Similar in concept to CTKE, turbulent kinetic energy (TKE) is the sum of the normal stress component means. Values of TKE at the springs were calculated as follows [*Pope,* 2000; *Monismith,* 2010]:

$$TKE = \frac{1}{2}\left(\overline{u'^2} + \overline{v'^2} + \overline{w'^2}\right) \tag{3-5}$$

Wave-turbulence decomposition was neglected based on the findings of *Bricker and Monismith* [2007]. Instruments with reliable compasses, tilt and pitch sensors, like the Nortek Vector ADV, produce a more dependable power spectrum than other methods of filtering or interpolating the wave frequencies *[Parra et al.,* 2015].

The turbulence dissipation rates were estimated from power spectra of the 10-minute bursts of vertical velocity (*w*) for Pargos using a Fast-Fourier Transform (FFT) [*Reidenbach et al.,* 2006; *Monismith,* 2010]. A Hanning window was applied to the spectra with a 50% overlap between windows, resulting in 124 degrees of freedom per spectrum (e.g., Figure 3-5A). Each spectrum was then examined to determine if it followed the theoretical '-5/3' law expected for the inertial subrange of turbulence [*Kolmogorov,* 1941; *Reidenbach,* 2006]. For spectra that satisfied the -5/3 slope (within 10%), dissipation rates were calculated. The following equation was applied, which incorporates Taylor's frozen turbulence hypothesis, converting wave number space to frequency space [*Hench and Rossman,* 2013]:

$$S_{ww}(f) = \frac{18}{55}\alpha\, \varepsilon^{2/3} f^{-5/3} \left(\frac{\overline{u}}{2\pi}\right)^{2/3} \qquad \text{(3-6)}$$

In the above equation, *S(f)* is the spectrum within the inertial subrange of the -5/3 fit, α is a constant, assumed to be 2 for the vertical velocity spectrum [*Hench and Rossman,* 2013], *f* is the spectral frequency, and $\overline{u}$ is the mean velocity for each burst. For each spectrum, the upper and lower frequency limits of the fit were extracted as the inertial subrange. This method allowed description of the evolution of dissipation rates and shifts in the inertial subrange over the spring-neap cycle.

Results

Pargos Spring

Measurements were obtained during the dry period at Pargos spring, where precipitation values averaged 1.5 mm/day, for a total of ~18 mm over the sampling period (Figure 3-2D). During the onset of sampling, ~5 m/s northeasterly winds blew from March 22-25, 2014 (Figure 3-2A). On the 25th, the winds shifted southeasterly, preceding a ~11 m/s northerly wind event that occurred on the 26th-27th. This wind sequence was repeated with ~6-7 m/s northeasterly wind on the 28th, a shift to east-southeasterly wind on the 29th-30th, followed by ~10 m/s northerly wind on the 31st of March.

The shift in wind velocity on March 26th was clearly identified in significant wave height H_s (Figure 3-2B), which doubled almost simultaneously. This increase in H_s (eq. 3-1) was also represented by the water surface elevation (η) as a set up on the 26th and lasting approximately 3.5 days. The highest η was observed during this setup event, but the largest tidal ranges (~0.3 m) occurred between the 29th and 31st, during the middle of syzygy (or spring) tide. Neap tide (~0.2 m range) was captured at the start of the sampling period through the 26th of March. A clear diurnal inequality (mixed tides) was seen in the difference between tide extremes of the dominant semidiurnal signal, particularly during neap tides.

The velocity components (Figure 3-2C) demonstrate the tidal modulation of SGD, consistent with previous studies of point source SGDs [*Valle-Levinson et al.,* 2011; *Expositio-Diaz et al.,* 2013; *Parra et al.,* 2014]. The vertical velocity component was positive and dominated the SGD magnitude for the majority of the experiment.

However, during the setup event in the water elevation (March 26-29th), vertical velocities became negative as a result of the increased hydrodynamic pressure over the spring. These negative vertical velocity events that occurred during the setup high tides are indicative of lagoon water intrusion into Pargos spring. Although time series salinity data were not available at the spring vent, salt intrusion is a valid assumption because the lagoon water (36 g/kg) is more saline than the spring water (22 g/kg). Another intrusion event occurred on March 30th when a shift in wind velocity caused an increase in Hs and η. These intrusion events occurred with only slight (~10 cm) increases in the water elevation, indicating the delicate piezometric balance of the groundwater aquifer.

Temperature data also confirmed the lagoon water intrusion during the setup event. The temperature in the lagoon was warmer (~28 °C) than the subterranean spring water (~26°C), resulting in temperature increases during intrusion events (i.e., syzygy high tides) (Figure 3-2D). Temperatures in the spring depicted semidiurnal oscillations during neap tide, indicating the presence of thermally stratified brackish water in the spring cavern [*Parra et al.,* 2015].

The shifts in wind direction and strength that resulted in intrusion conditions correspond to changes in the precipitation data (Figure 3-2D). The pulses of increased precipitation precede the shifts in wind, suggesting that storm events cause the setup events. Over the sampling period, the pluvial input into the system was low (average ~1.5mm/day). Therefore, a surge in SGD magnitude or intensity was not expected from increased backpressure inland at the cenotes.

Turbulent Kinetic Energy (TKE) also demonstrated variability over the fortnightly tidal cycle (Figure 3-2E). Peaks in TKE occurred at the start of the setup event on the

26th, reaching a maximum of ~0.63 m^2s^{-2}. During neap tide, TKE values were noisy and exhibited a slight modulation by the semidiurnal tide, with higher values (~0.3 m^2s^{-2}) occurring during low neap tide, and lower values (~0.05 m^2s^{-2}) occurring during high neap tide. During the setup event, TKE was clearly modulated by the spring tide with values of TKE ranging from ~0.2 m^2s^{-2} (at syzygy low tide) to complete suppression during intrusion periods (~10^{-7} m^2s^{-2} at syzygy high tide).

Gorgos Spring

Measurements at Gorgos were obtained during the wet season, when precipitation values averaged 6.5 mm/day, for a total of ~78 mm over the sampling period (Figure 3-3D). During the beginning of the sampling period, winds were variable (Figure 3-3A), shifting from ~7 m/s northwesterly gusts to <5 m/s northerly winds. Steady, moderate (6-7 m/s) northeasterly winds appeared on September 12, 2014, and increased in strength (~10 m/s) over the experiment's duration. The pulses in the east component of wind on the 7th, 11th, and 14th of September 2014, indicate the occurrence of weather events (e.g., storms), which was confirmed by the on-site observations.

The influence of steady northeasterly winds caused setup in eta, η, during the last half of the experiment, as seen in Figure 3-3B. The tide transitioned from syzygy at the beginning of the time series to quadrature on the 12th of September. Increases in subtidal η coincided with the spikes in the westward component of wind, suggesting the origin of the setup. While Hs remained relatively constant over the observation period, a set up event (~5.5 day duration) was observed in η, starting on the 11th. As a result of the setup event, η during quadrature low tides exceeded η during syzygy high tides.

The influence of the setup event is clearly seen in the velocity components (Figure 3-3C). The magnitude of SGD decreased with increased η. Two findings become evident.

- Gorgos spring continuously discharged throughout the time period, as indicated by the positive SGD magnitude (Figure 3-3C), despite the increase in eta, η (Figure 3-3B). It is expected that for high η, SGD magnitudes will be minimum. However, although the range of SGD magnitudes decreases during the highest η (setup event), minimum discharge values are not observed during this time. This observation is likely a result of an increased backpressure due to pluvial input into the inland cenotes and aquifer.
- The horizontal (eastward) velocity component, rather than the vertical dominates the SGD magnitude (Figure 3-3C). This result suggests that the SGD at Gorgos is controlled by across lagoon flows, which are eastward dominant, favoring inlet outflow, as observed in Chapter 2. The strong influence of the lagoon currents are likely a result of the placement of the velocimeter, which was ~10 cm above the spring vent.

Water temperature exhibits diurnal oscillations ranging from ~28 to 30°C (Figure 3-3D). Drops in temperature are observed during peaks in rainfall (e.g. September 7th), indicating cooler rain input inland that discharges from the spring. It is worth noting that the pulses in rainfall correspond with the peaks in the east component of wind on the 7th, 11th, and 14th of September 2014 (Figure 3-3A) associated with storms.

Values of TKE were modulated by the semidiurnal tide and showed variability over the fortnightly tidal cycle (Figure 3-3E). During syzygy, TKE values reached maxima of >1.5 m^2s^{-2} (low tide) and minima of ~0.01 m^2s^{-2} (high tide). Over neap tide, TKE exhibited similar behavior, but had a smaller range (0.2 to 1.5 m^2s^{-2}). The setup event during quadrature caused water elevations to surpass those observed during syzygy, resulting in neap low tide to be higher than spring high tide (Figure 3-3B). Interestingly, the lowest TKE values were not observed during the highest η (neap-setup high tides). This observation confirms the notion that increased backpressure of the inland water elevation (e.g., cenote) from pluvial input causes SGD to increase in intensity, which is balanced by the increase in η from the setup event.

Turbulence Characterization

The following parameters were evaluated at the two springs: turbulence intensity (I), turbulent kinetic energy (TKE), and coherent turbulent kinetic energy (CTKE) (Figure 3-4). Upon comparison, it is clear that the discharges of the two springs behave very differently. At Pargos spring, TKE values ranged in magnitude from 10^{-5} to 10^{-1} m^2s^{-2}. Values of CTKE were two orders of magnitude lower, ranging from 10^{-7} to 10^{-3} m^2s^{-2}. In addition, the CTKE data mimic the behavior of TKE and have a nearly identical subtidal signal (i.e., Figure 3-4B&C, red line). The subtidal signals also highlight the decrease in both TKE and CTKE values during the setup event on the 26th of March (Figure 3-2B), confirming the suppression of SGD during the setup period. Furthermore, the inverse relationship between the subtidal eta (η) (Figure 3-2B) and subtidal signals of TKE and CTKE is evident for long (>24 hours) period oscillations throughout the sampling period.

At Gorgos, TKE values were greater than Pargos, with ranges in magnitude between 10^{-2} and 1 m^2s^{-2}. Values of Gorgos CTKE were noisier and smaller in magnitude than the TKE, with values ranging from 10^{-7} to 10^{-4} m^2s^{-2} (Figure 3-4B&C). When compared to the subtidal η (Figure 3-3B), the subtidal signals of TKE and CTKE do not follow an inverse relationship, particularly at the start of the setup event. An inverse relationship between η and TKE is expected since pressure head over the spring is known to modulate the discharge, and therefore turbulence parameters. However, Gorgos turbulence characteristics do not follow the subtidal η. This observation suggests that although TKE at Gorgos is modulated by the semidiurnal tides, long period oscillations (>24 hours) of TKE and CTKE are probably more dependent on pluvial input (Figure 3-3D) than η (Figure 3-3B).

At Pargos, values of intensity, *I*, for the horizontal components (*u,v*) were similar (Figure 3-4A). In addition, velocity components at Pargos had the same sign during the semidiurnal tidal modulation, indicating an isotropic turbulent field [*McCaffrey et al.,* 2015]. Isotropic turbulence was confirmed through a scatter plot comparison of velocity components (Figure 3-4D) based on turbulence theory [*Kundu et al.,* 2012]. Isotropic turbulent fields should depict well-dispersed values of u-v components, in which the average product of the u-v data equals zero [e.g., *Kundu et al.,* 2012, pg. 561]. Conversely, anisotropic turbulent fields are identified through skewed scatter plots where the average product of u-v data does not equal zero.

At Gorgos, values of *I* were inherently different for all velocity components (Figure 3-4A). The semidiurnal modulation of the horizontal components became incoherent at the start of the setup event (September 11, 2014). However, during the setup event, horizontal intensities increased at Gorgos, which contrasts with the expected behavior of decreasing turbulence intensity with increasing η (e.g., Pargos). This result suggests that the increased intensity of SGD is a result of the pluvial input into the system, which is balanced by the increase in η of the setup. The dominance of the east component of velocity intensities at Gorgos indicates that the SGD is modulated by the eastward across lagoon flows. Based on the above comparison, Pargos spring, an isotropic turbulent field, was further analyzed in the Discussion session.

Discussion

Spring Comparison

It is evident from the Results that the two spring systems are different, despite their geographic proximity (<200m). The differences stem from SGD intensity (due to pluvial recharge) and spring morphology. Precipitation during the Gorgos experiment was nearly five times that of rainfall recorded during the Pargos experiment, resulting in more intense flows and continuous outflow at Gorgos. Although the springs are inherently different, Gorgos SGD magnitudes were always greater than those at Pargos, even during the setup event. The higher SGD values at Gorgos explain the high TKE values, which are an order of magnitude higher than those observed at Pargos.

The morphology of the springs encompasses the vent orientation and surrounding bathymetry, which varied between the two sites. Pargos spring vent was oriented horizontally and located in the side of a bathymetric hollow, ~1.5 m below the lagoon floor (Figure 3-1B). The shield of the surrounding bathymetry allowed the ADV to collect data, relatively undisturbed from along and across lagoon flows that affect the bed. In contrast, Gorgos spring is located on the open bed, exposed to lagoon currents (Figure 3-1C). In addition, the Gorgos vent is flush with the lagoon's bottom, causing SDG magnitude to be dominated by the east component of flow. Due to the SGD intensity and exposure to lagoon flows, the Gorgos turbulence field was anisotropic and more complex than Pargos. As a result, the remainder of the Discussion will focus on analyzing turbulence dissipation behavior at isotropic Pargos.

Turbulence Dissipation at Pargos

The turbulence field at Pargos can be classified as isotropic, and the turbulence intensities are on average < 1. It is therefore appropriate to use Taylor's Frozen

Hypothesis method when calculating dissipation rates [*Monismith,* 2007; *Walter et al.,* 2011]. Dissipation rates and inertial subrange frequencies were calculated for each 10-minute burst's power spectrum of vertical velocity that followed the '-5/3' law (e.g., Figure 3-5A). Figure 3-5B presents the evolution of the inertial subrange over the spring-neap cycle. Over the experiment length, the inertial subrange varied in frequency from 0.01 to 6 Hz. During neap tide (March 21-25th), the '-5/3' law was followed predominantly at low vertical velocities (high η), resulting in a banded temporal evolution. However, during spring tide (26 March – 02 April), inertial subranges were observed throughout the tidal cycle. At high vertical velocities (low η), the inertial subrange shifted to higher frequencies, according to Nasmyth spectra [*Nasmyth,* 1970].

Dissipation values calculated from the inertial subranges varied from $\sim 10^{-7}$ to 10^{-3} m^2s^{-3} (order of magnitude) and were on average $\sim 10^{-4}$ m^2s^{-3}, similar to findings obtained by *Parra et al.,* [2014]. For most of neap tide, dissipation rates remained relatively low and occurred at high tide. However, during spring tide, extreme lows in η (Figure 3-5C) resulted in sustained high vertical velocities (~0.2 m/s) (Figure 3-5D), which allowed dissipation to fully develop, reaching maximum rates (Figure 3-5E). During these events (syzygy low tide), shifts to higher frequencies were observed in the inertial subrange (Figure 3-5B).

It is well known that turbulence dissipation is balanced by production, transport, and buoyancy production [*Monismith,* 2010; *Expositio-Diaz et al.,* 2013; *Parra et al.,* 2014; *Lueck,* 2015]. Dissipation rates at Pargos were of the same order of magnitude as production values obtained at another submarine spring in the Yucatan peninsula by *Expositio-Diaz et al.,* [2013]. Furthermore, Pargos dissipation values were similar in magnitude to production values found in active mixing environments, such as tidal channels [*Rippeth et al.,* 2002]. This result is not unexpected since the ratio of the vertical to horizontal velocity components is higher at a SGD point source than in tidal channel flow [e.g., *Souza et al.,* 2004].

For submarine groundwater discharges like Pargos, a clear relationship exists between discharge velocity, water elevation, and turbulence dissipation rates (Figure 3-5). At low η, discharge velocity and dissipation reach maximum values. To further explore this relationship, a scatter diagram between discharge velocity *w* and dissipation ε was examined, with references to η linkages (Figure 3-6A). Indeed, a relationship was established between *w* and ε, indicating that higher w (lower η) was related to ε increase (Figure 3-6A). The behavior of dissipation follows a hyperbolic curve with minimum values occurring between -0.05 and 0 m/s discharge velocities. However, it is important to note that flow fields will vary with respect to the venturi-like constriction of the spring vent. Positive discharges will result in expansion of flow as it leaves the constriction, while negative discharge will result in convergence of flow as it enters the spring vent. This flow behavior results in varying turbulence fields based on the discharge velocity direction. Therefore, it is appropriate to focus on the expanding flow behavior to establish a relationship between positive w and ε. (Figure 3-6B), as follows:

$$log_{10}(\varepsilon) = 8.3w - 4.1 \tag{3-7}$$

The resulting R^2 value of 0.85 indicates the improved fit and validity of the proposed relationship. This relationship between positive w and ε supports the findings of *Parra et al.,* [2014], which present an exponential fit to scatter of TKE and η. The link between η and TKE is useful in understanding turbulence behavior at SGDs. However, the connection between w and ε is a more valuable metric, since additional variables influence SGD intensity, and in turn, turbulence behavior (e.g., rain recharge).

Predicting SGD and Dissipation

In karst coastal aquifers, submarine groundwater discharge is driven by a hydraulic pressure gradient between the inland water table (e.g., cenote) and η [*Valle-Levinson et al.,* 2011]. The momentum balance associated with this scenario emulates communicating vessels and may be approximated through a Bernoulli balance modified by friction [e.g., *Parra et al.,* 2015]. While karst conduits are highly variable in diameter and roughness, numerical models have simulated laminar and turbulent flow through them using pipe flow fundamentals [*Kaufmann and Braun,* 1999]. Field observations have also successfully applied Bernoulli dynamics to estimate SGD *[Parra et al.,* 2015]. Following the approach of *Parra et al.* [2015], SGD was approximated using the following equation:

$$\left(g\rho_1 h_1 + \frac{\rho_1 w_1^2}{2}\right)_{cenote} = \left(g\rho_2 h_2 + \frac{\rho_2 w_2^2}{2}\right)_{spring} + \rho_2 h_L \qquad (3\text{-}8)$$

where g is gravitational acceleration (9.81 ms^{-2}), ρ is the water density (ρ_1 = 1000 kgm^{-3} and ρ_2 = 1022 kgm^{-3}), h is the water surface elevation (h_1= cenote and h_2= spring), w is the velocity (w_1 = cenote and w_2 = SGD magnitude), and h_L is the energy transfer to friction in the system. Friction was estimated using the Darcy-Weisbach equation for losses in pipe flow [*Parra et al.,* 2015]:

$$h = \frac{fLw_2^2}{2D} \qquad (3\text{-}9)$$

where f is the dimensionless friction factor, L is the distance from the cenote to spring, and D is spring vent diameter. *Parra et al.* [2015] did not have available cenote data, and so they neglected the velocity term w_1 and values of h_1. Values of f were obtained through minimization of the root mean square error (RMSE) between observed and predicted w_2 (resulting R^2 values of 0.55 & 0.72). To improve their estimates of SGD, cenote water level data were collected over the sampling period of Pargos and incorporated into Equation 3-8. Pressure data were collected from March 23rd through April 1, 2014, at cenote CTC, located approximately 13 km west of Pargos. Cenote velocity, w_1, was estimated as the change in pressure head over the sampling time interval (5 minutes) and was found to be negligible.

Using Equation 3-8, the friction factor was optimized through a minimization of the RMSE between observed and calculated w_2. In doing so, a friction factor of $f = 0.012$ was obtained for the cenote-spring system. While this number appears intuitively small for rough, turbulent pipe flow, it falls within the range predicted by the karst conduit numerical models of *Kaufmann and Braun* [1999]. The friction factor applies to the total aquifer distance between the spring and cenote, in which the conduits vary from constrictions <1 m to wide underground rivers (10 m) [*Beddows et al.,* 2007]. In the large conduit sections of the aquifer, it is expected that frictional effects due to karst wall roughness will be minimized. In addition, the calculated friction factor matches values observed at karst aquifers in the Yucatan peninsula [e.g. *Springer,* 2004; *Parra et al.,* 2015]. Figure 3-7 depicts the results of the improved SGD calculations through a comparison of calculated versus observed w_2. During the beginning and end of the time series (quadrature and syzygy, respectively), the predicted values overestimate the actual discharge magnitude. However during the 3.5-day setup event starting on the 26th, discharge velocities are underestimated at negative velocities (high η). Nevertheless, the R^2 value of 0.82, as observed in the scatter trend in Figure 3-7B, provides confidence in the idea that the discharge is mainly governed by 'leaky' or 'frictional' Bernoulli dynamics.

The improved prediction of w_2, through the incorporation of inland η, has key implications for determining the behavior of other variables in the spring-cenote system. For instance, once a friction factor is known for a system, velocities at the spring can be reliably predicted with only a pressure head gradient between the cenote and spring. Utilizing this concept, spring velocities were estimated from the time series of pressure data at the cenote and spring. The predicted velocity values were then substituted into the linear relationship found between w and ε (Figure 3-6B). Remarkably, the behavior of ε was captured quite well (Figure 3-8). The predicted values of ε tend to underestimate observed peaks in ε. This result is likely due to the linear fit (Figure 3-6). Regardless, the predicted values of ε match the behavior of observed values, with explained variance of $R^2 = 0.60$.

SGD and Turbulence Conclusions

Despite geographic proximity, SGD behavior can vary widely between springs. The results of this chapter support the relevance of the pressure gradients driving discharge. Changes in recharge (due to rain or anthropogenic consumption) determine whether saltwater intrusion events (backflow) could occur based on relatively small changes (<0.3 m tidal range) in the water surface, η.

Seasonal precipitation cycles affect SGDs by controlling recharge. During the dry season (Pargos), water elevation (η) was the dominating mechanism for SGD, TKE, and temperature modulation on tidal and subtidal time scales. During the wet season (Gorgos), semidiurnal oscillations in η modulated SGD and TKE on shorter time scales (~12.42 hr), but pluvial input and across lagoon flows became influential factors in the subtidal signal. In addition to pluvial input, the spring morphology plays a role in SGD and turbulence behavior. In bathymetrically protected springs, like Pargos, turbulence fields are isotropic, and allowed to develop relatively free from the influence of currents in the lagoon. Conversely, SGDs at unprotected springs are subject to lagoon flows, resulting in anisotropic turbulence fields.

For Pargos (isotropic turbulence), dissipation behavior increases exponentially with increasing SGD velocity. Peaks in dissipation occur at maximum vertical velocities (syzygy low tide). During these periods, the inertial subrange shifted to higher frequencies. The high sampling rate of the ADV allowed the highest frequencies of the inertial subrange shifts to be captured. This result suggests that for future research, a sampling rate of at least 16 Hz is needed to fully capture the inertial subrange behavior over the spring-neap cycle.

A novel approach to estimate turbulence dissipation rates has been presented, using only pressure data at a spring and inland source. Future studies in the area should consider implementing this method when instrumentation for other methods of calculating turbulence dissipation is unavailable. This method would be especially useful for evaluating dissipation behavior over significantly longer time scales (~months).

The global significance of these findings will help classify and predict discharge and turbulence behavior at coastal SGD sources. Understanding the relationship between these processes is of vital importance to the health of the system. It predicts occurrences of backflow (into the spring), determining when saltwater intrusion may pose a threat to fresh groundwater resources. In addition, mixing via SGD and turbulence gives valuable insight to the transport and concentrations of nutrients, pollutants, and microbial species in the lagoon. Whether SGDs need to be monitored for intrusion events or investigated as potential energy sources, it is vital to monitor and understand these systems.

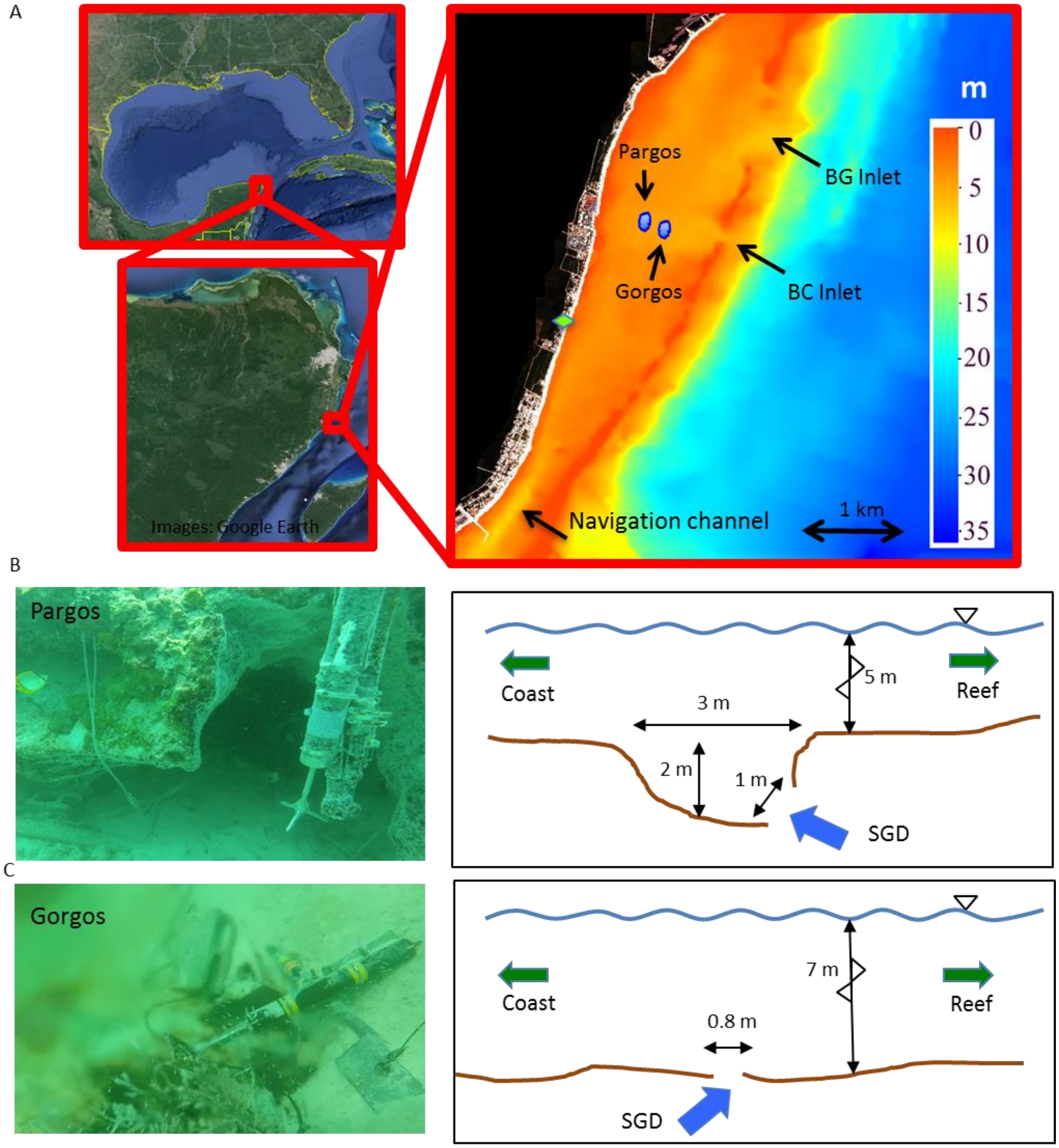

Figure 3-1. Site location and instrument location A) Geographic reference: Puerto Morelos, Quintana Roo, Mexico. The Puerto Morelos fringing reef is located on the NE coast of the Yucatan peninsula. There are two inlets: Boca Grande to the north and Boca Chica in the center of the reef. A navigation channel is located at the southern end of the lagoon. B) Pargos instrument placement and spring bathymetry/dimensions C) Gorgos instrument placement and spring bathymetry/dimensions

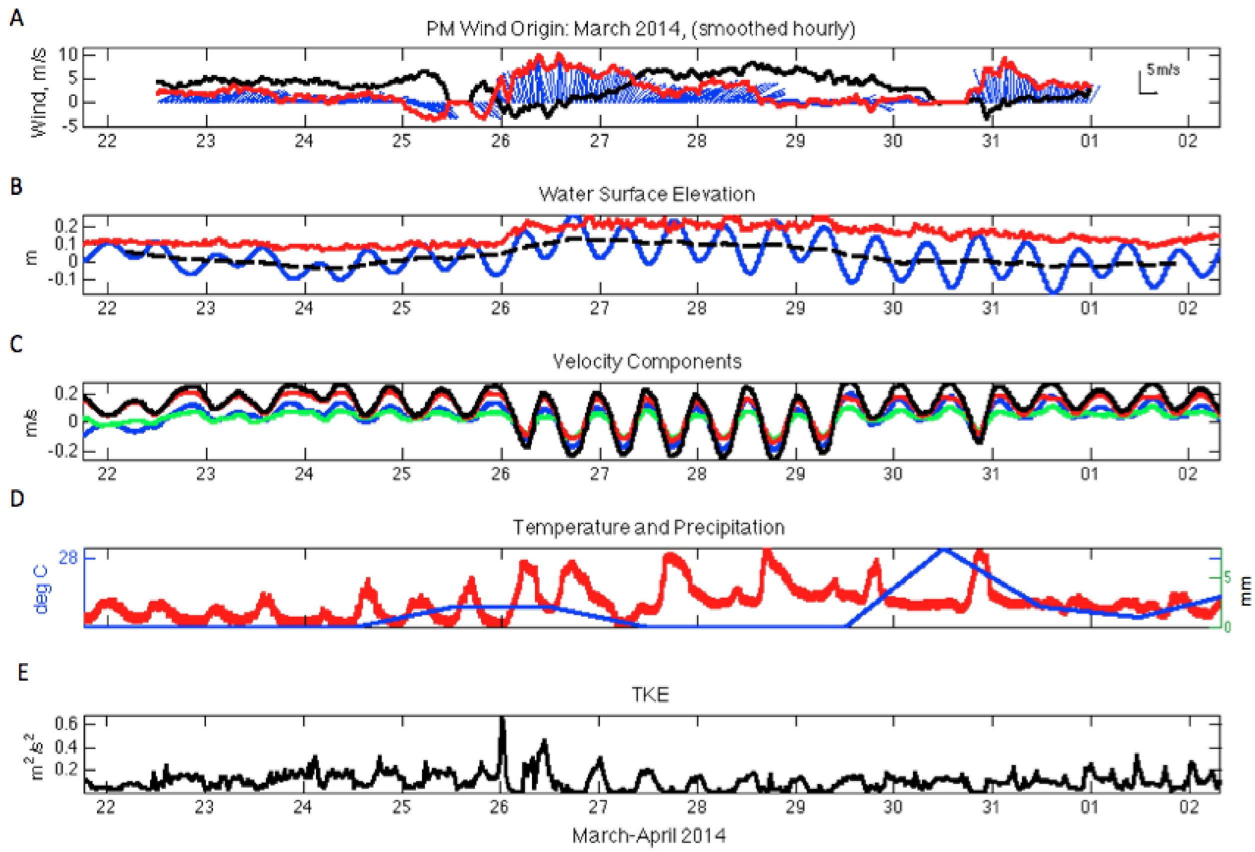

Figure 3-2. Atmospheric and oceanic forcing conditions at Pargos. A) Wind vectors (origin) and magnitude of East-West (black line) and North-South (red line) components. Note: no wind data were available at the start and end of the experiment. B) Water surface elevation (demeaned, blue line) indicates a semidiurnal tidal signal. The black line is the sub-tidal signal, and the red line is a reference to variations in pressure (as 4*standard deviation of η). Both highlight the setup event (March 26-29, 2014). C) Velocity components at the spring, where the blue line is the U component (East-West), the green line is the V component (North-South), the red line is the vertical component (up-down), and the black line is the magnitude of the three velocity components. D) Temperature at the spring is shown by the red line, and precipitation values in mm (right side y axis) are shown by the blue line. E) Turbulent Kinetic Energy (TKE) is depicted by the black line.

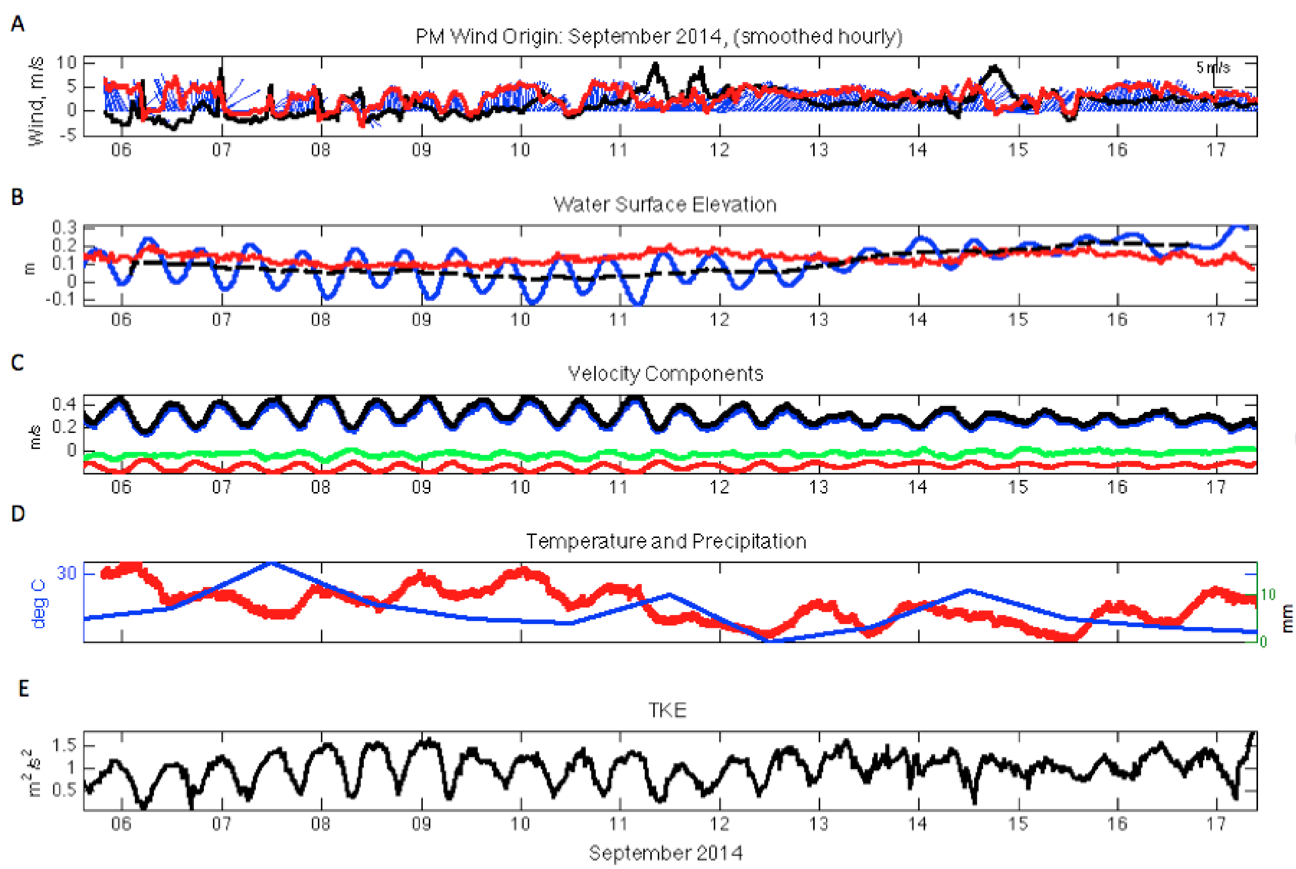

Figure 3-3. Atmospheric and oceanic forcing conditions at Gorgos. A) Wind vectors (origin) and magnitude of East-West (black line) and North-South (red line) components. B) Water surface elevation (demeaned, blue line) indicates a semidiurnal tidal signal. The black line is the sub-tidal signal, and the red line is a reference to variations in pressure (as 4*standard deviation of η). C) Velocity components at the spring, where the blue line is the U component (East-West), the green line is the V component (North-South), the red line is the vertical component (up-down), and the black line is the magnitude of the three velocity components. D) Temperature at the spring is shown by the red line, and precipitation values in mm (right side y axis) are shown by the blue line. E) Turbulent Kinetic Energy (TKE) is depicted by the black line.

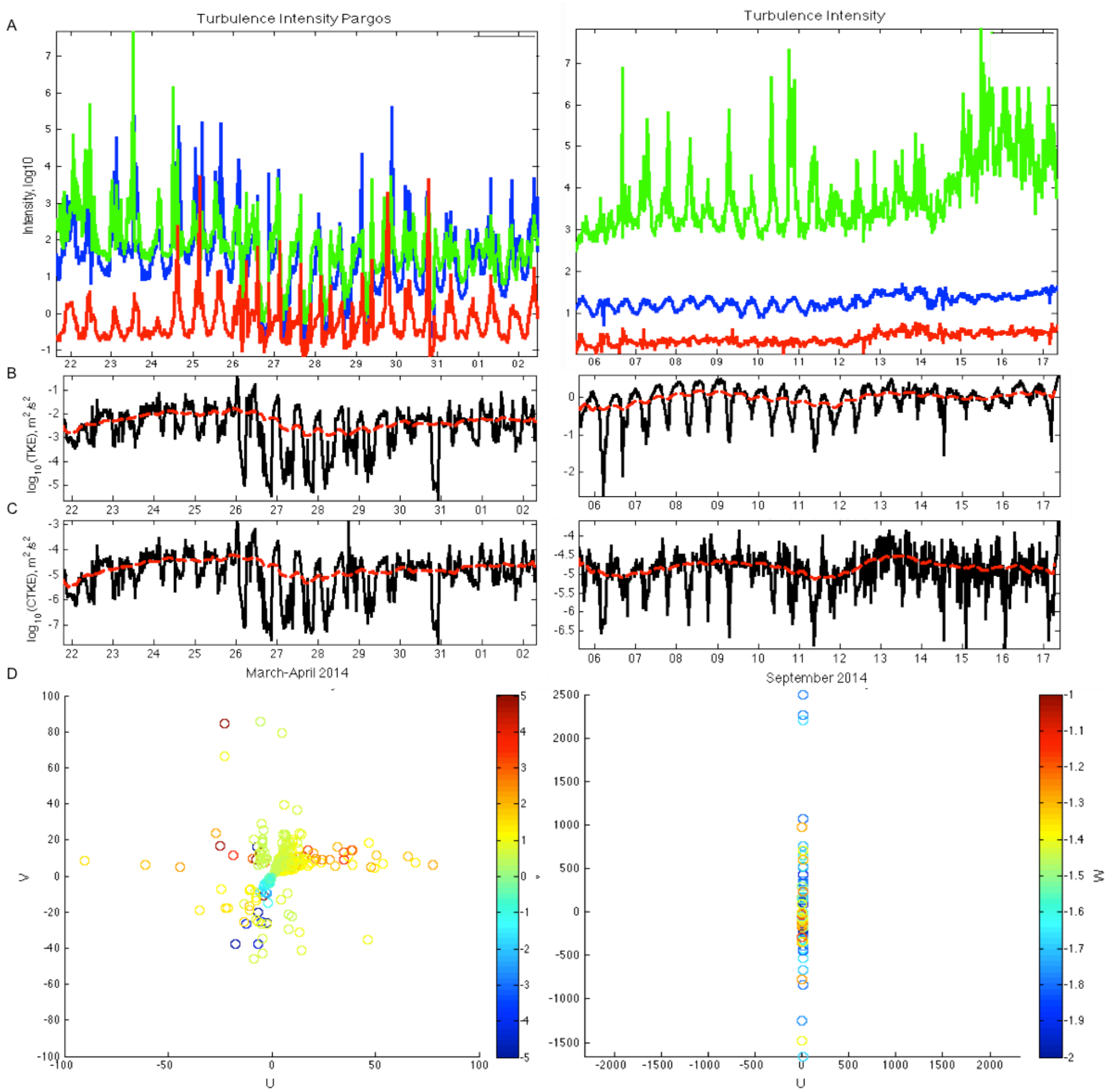

Figure 3-4. Turbulence characterization comparisons of Pargos and Gorgos. A) Demonstrates the Intensity (I) of the velocity components: U (blue line), V (green line), and W (red line). B) TKE values are shown plotted on a log10 scale (black line) with subtidal signal shown in the red line. C) CTKE values are shown plotted on a log10 scale (black line) with subtidal signal shown in the red line. D) Demonstrates the scatter of u-v components. The well-spread scatter of Pargos indicates an isotropic turbulence field. The linear scatter of Gorgos indicates an anisotropic turbulence field [*Kundu et al.,* 2012].

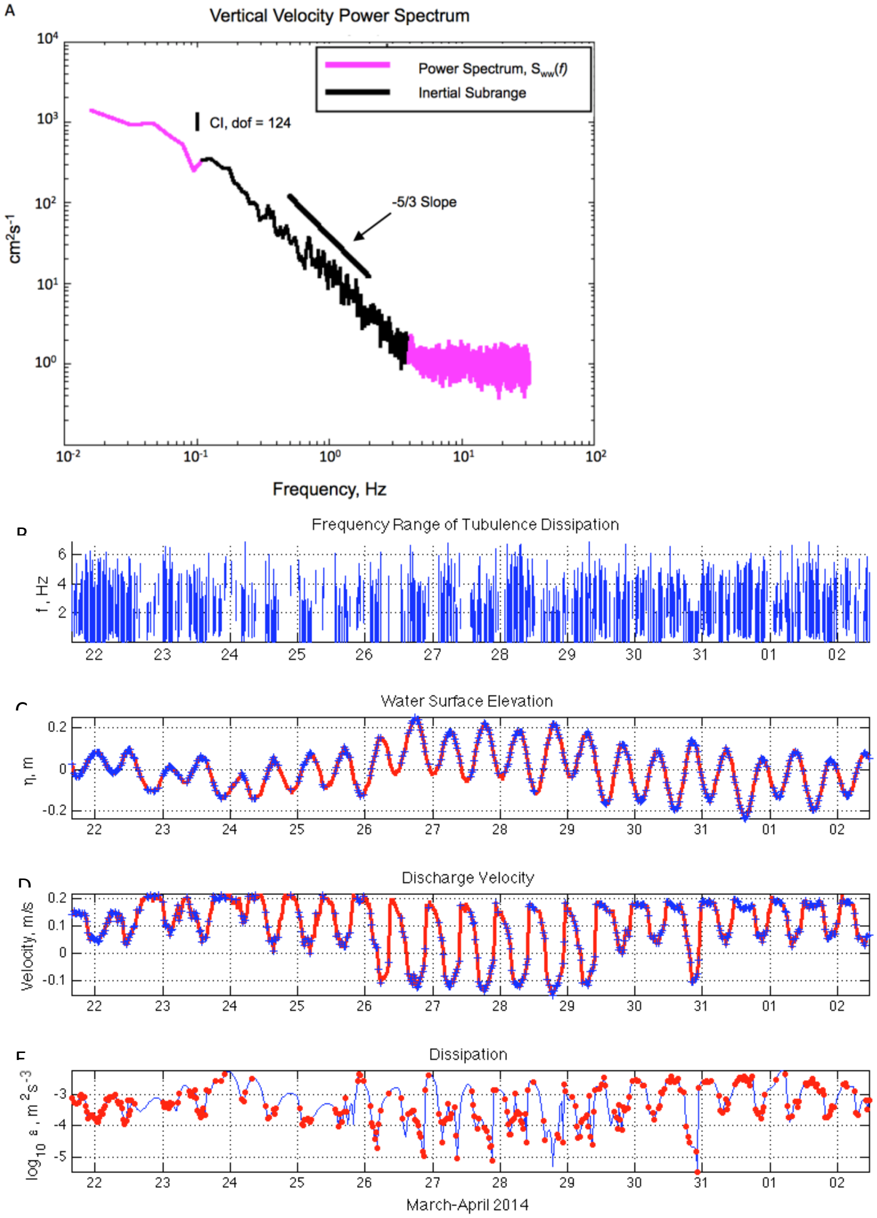

Figure 3-5. Behavior of TKE Dissipation at Pargos. A) Power spectrum example of a 10-minute burst of vertical velocity data. The black line over the power spectrum signal demonstrates the period of the spectrum that follows Kolmogorov's Law. The upper and low frequencies represent the limits of the inertial subrange B) Frequency range of dissipation represents the evolution of the inertial subrange over the sampling period. C) The water surface elevation, η, is plotted in red, with blue crosses that demonstrate instances when Kolmogorov's Law was followed. D) The discharge velocity is plotted in red, with Kolmogorov behavior indicated by the blue crosses. E) Dissipation rates obtained from the spectra and Equation 3-6 are indicated by the red dots. The blue line is the interpolated time series, predicting dissipation values for spectra that did not follow Kolmogorov's Law.

A

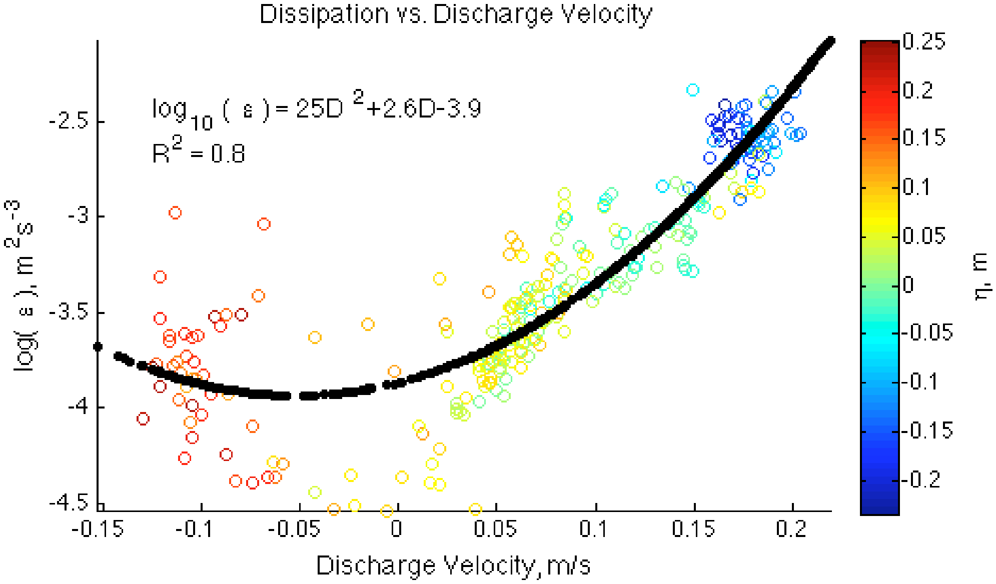

B

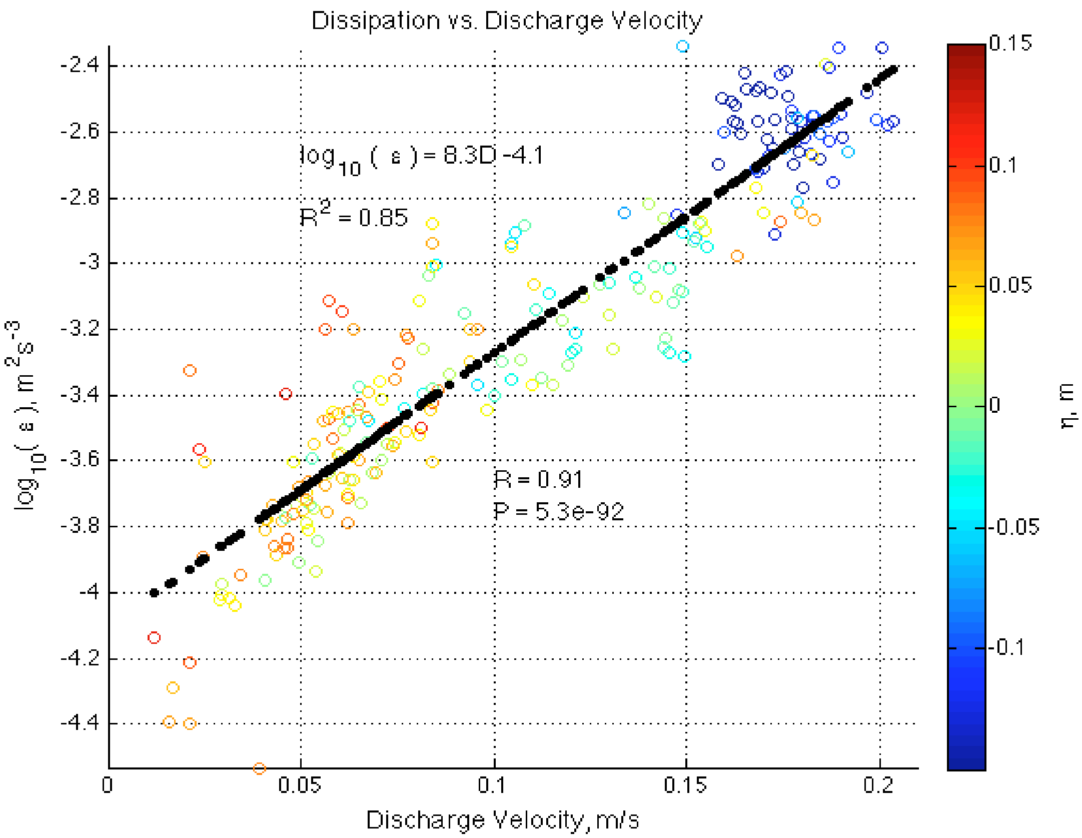

Figure 3-6. Relationship between dissipation, discharge velocity, and water surface elevation at Pargos. A) Demonstrates the second-degree polynomial fit of discharge velocity to the log10 of dissipation. The scatter references values of eta (η), as indicated by the colorbar. B) Depicts the linear relationship between positive discharge velocities and dissipation rates.

A

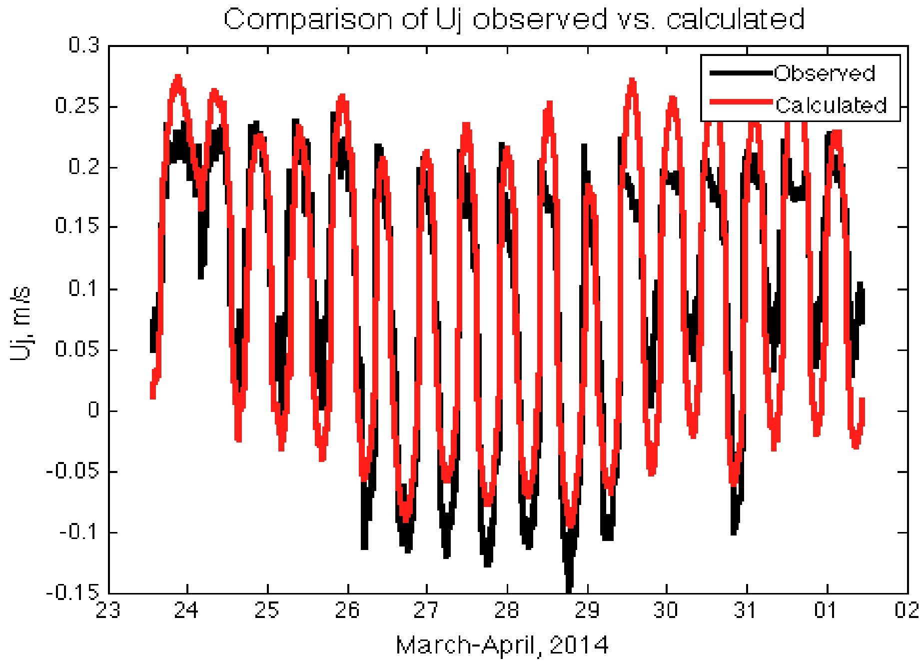

B

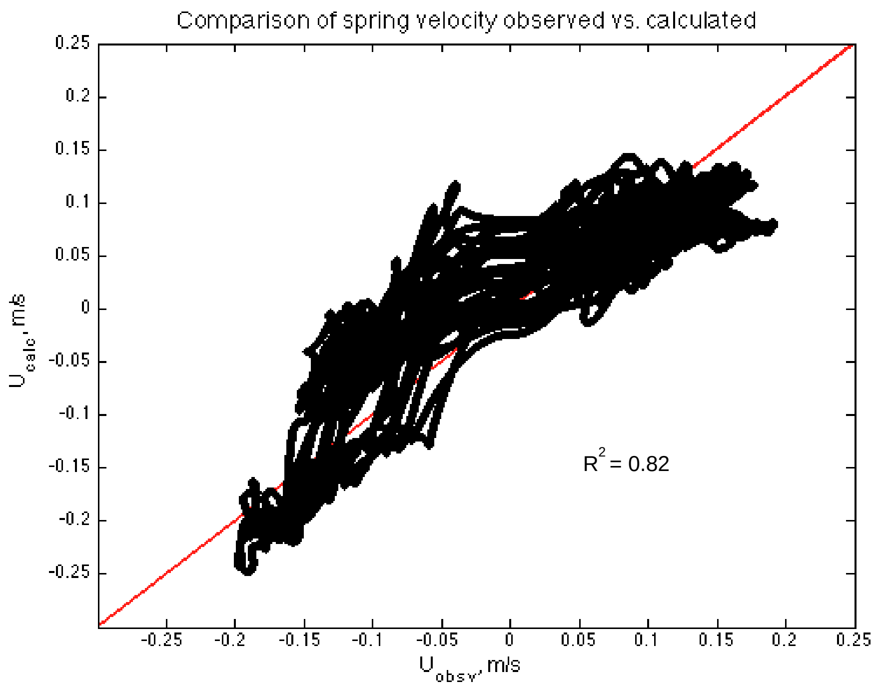

Figure 3-7. Applied Bernoulli dynamics to estimate submarine groundwater discharge. A) Calculated versus Observed comparison of discharge velocity. B) Scatter plot of calculated versus observed values, with an R^2 = 0.82. These figures demonstrate the improvement of the SGD estimation method by incorporating water level variations at the cenote.

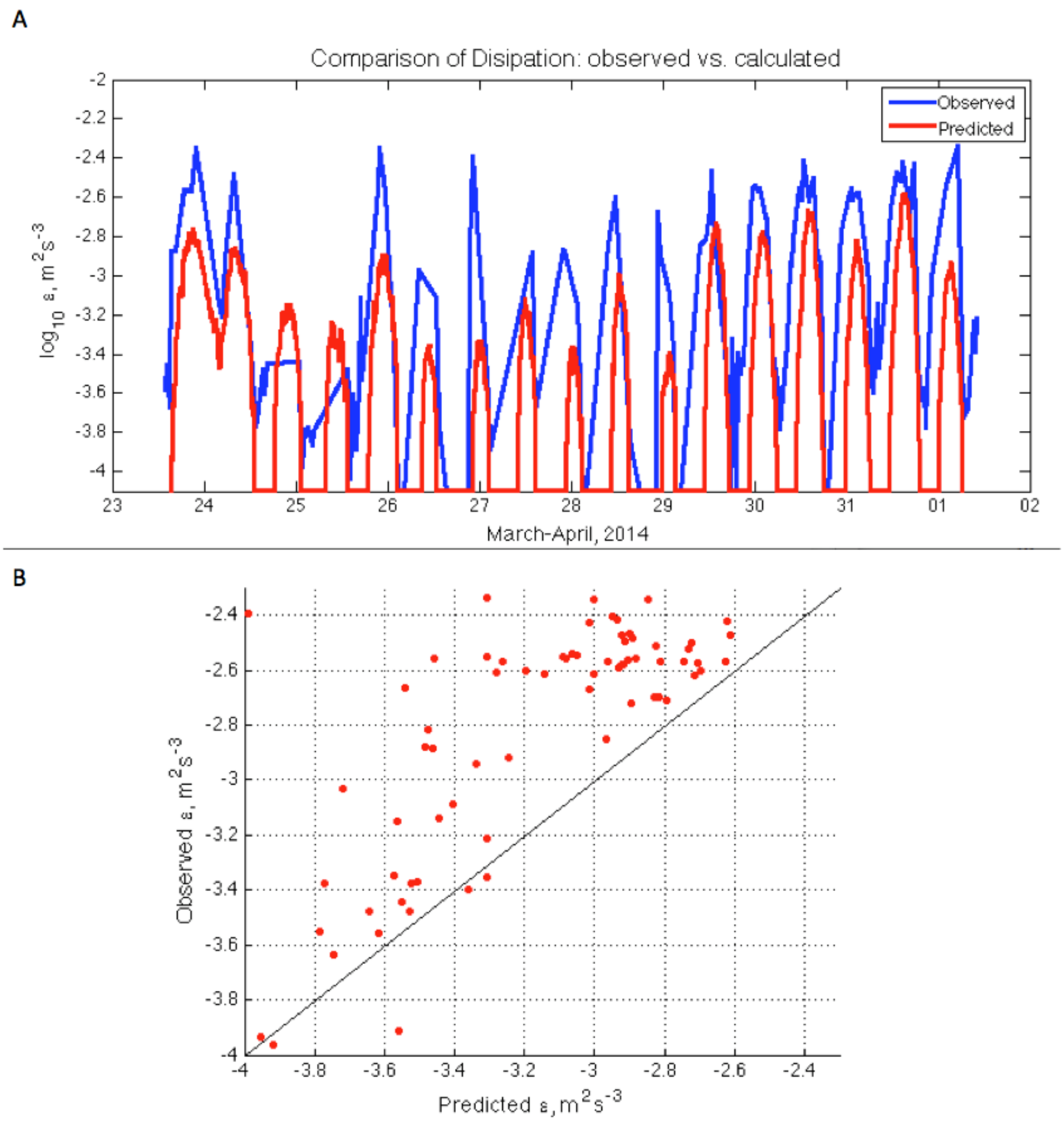

Figure 3-8. Observed versus predicted dissipation rates calculated from two pressure heads. A) Time series of values B) Scatter plot showing R squared correlation of 0.6. The proposed method of predicting dissipation underestimates the observed values, but matches the behavior. Note: A log10 value of -4.1 establishes the floor of the fit as a result of the zero intercept in Equation 3-7.

CHAPTER 4
LAGOON AND SGD INTERACTIONS

Introduction to Circulation and SGD Processes

Background

It is widely accepted that the hydrodynamics of coral reefs determine the ecological efficiency and health of these systems [*Monismith,* 2007; *Hearn,* 2011; *Hench and Rosman,* 2013]. The spatial scales of coral reef hydrodynamics can vary from several kilometers (regional scales) [e.g., *Hench et al.,* 2008; *Lowe et al.,* 2009] to less than a millimeter (molecular scales) [*Hearn and Hunter,* 2001]. In addition, hydrodynamics associated with lagoon-reef flows vary temporally at time scales that occur instantaneously (<1s), daily (tidal), weekly (fortnightly and subtidal), monthly, annually, and interannually. Furthermore, the highly variable scales (temporal and spatial) of physical phenomena associated with reef hydrodynamics are interconnected [e.g., *Hearn and Hunter,* 2001]. However, as the number of physical processes that are studied increases, the ability to resolve dependent and independent mechanisms becomes more difficult. Nevertheless, it is important to consider the relation of individual processes with respect to the system as a whole for scientific investigations [e.g., *Hearn and Hunter,* 2001].

Overall circulation in lagoon-reef systems is driven by wave breaking, tides, winds, and buoyancy [*Monismith,* 2010]. In turn, the comparative influence of these forcing mechanisms in the shallow reef system depends on climate and morphology [*Lowe et al.,* 2009; *Taebi et al.,* 2011]. Previous research via numerical models [e.g., *Gourlay and Colleter,* 2005; *Symonds et al.,* 1995] and field experiments [e.g., *Hench et al.,* 2008; *Lugo-Fernandez et al.,* 2004] has focused mainly on barrier and atoll reef geomorphologies [*Weins,* 1962]. Only recently have studies began focusing on shallower, coastal reef environments known as fringing reefs [*Coronado et al.,* 2007; *Hench et al.,* 2008; *Lowe et al.,* 2009b; *Taebi et al.,* 2011]. Fringing reefs [*Weins,* 1962] grow adjacent to the coast and have shallow lagoons that exchange flow with the ocean at reef breaks [*Kennedy and Woodroffe,* 2002]. It is well recognized that circulation in these systems is driven by wave breaking over the reef, particularly when the tidal range is small (<0.5 m). The wave breaking action at the reefs generates radiation stress gradients and setup in the lagoon that drives outflow at the reef breaks [*Longuet & Stewart,* 1964;*Coronado et al.,* 2007; *Hench et al.,* 2008*; Taebi,* 2011].

The reef acts as a barrier by dissipating incoming wave energy, resulting in decreased significant wave height within the lagoon. However, long period (> 25 s) infragravity (IG) waves do not break at the reef due to their length with respect to water depth [*Munk*, 1949]. As a result, IG waves are able to propagate into the lagoon [*Torres-Freyermuth,* 2012]. IG waves can carry equivalent energy to gravity waves, despite their lower amplitude, because of their longer wavelength (i.e., linear wave theory). Previous studies have demonstrated increased coastal flooding as a result of resonance-generated IG waves [*Pequignet et al.,* 2009; *Torres-Freyermuth,* 2012], highlighting the need to understand their role in fringing reef environments.

Fringing reefs can be located in tropical regions [*Torres-Freyermuth,* 2012] where karst topography is common in coastal aquifers [*Shoemaker et al.,* 2008; *Parra et al.,* 2014]. These karst landscapes are comprised of mainly calcium carbonate (e.g., limestone), which dissolves over time to form a complex maze of subterranean conduits (water filled caves). These conduits can hydraulically connect coastal aquifers to the sea resulting in discharge at the seabed [*Valle Levinson et al.,* 2011; *Parra et al.,* 2014]. This connectivity determines the mixing characteristics of the 'subterranean estuary' [*Moore,* 1996].

Submarine groundwater discharge (SGD) has become widely recognized as a critical connection between fresh groundwater resources and the sea, influencing the global budget of dissolved materials [*Moore,* 1996; *Santos et al.,* 2008; *Valle Levinson et al.,* 2011]. Research has shown that SGDs can vary from slow diffusive fluxes (~ cm/day) through bed sediment seepage [*Paulsen et al.,* 2004; *Martin et al.*, 2007] to rapid fluxes (~1 m/s) at point sources [*Valle Levinson et al.,* 2011]. Recently, studies have made an effort to understand the hydrologic characteristics of SGDs at springs (point-sources) [*Peterson et al.,* 2009; *Valle-Levinson et al.,* 2011; *Exposito-Diaz et al.,* 2013; *Parra et al.,* 2014]. In these systems, the piezometric pressure heads of the inland water table and the sea surface balance the groundwater matrix and control SGD [*Valle Levinson et al.,* 2011]. The change in sea surface elevation due to tides, wind, waves, storm surge, and set-up have been shown to modulate the spring's discharge by influencing the relative pressure gradient [*Li et al.,* 1999; *Kim and Hwang,* 2002; *Taniguchi,* 2002; *Valle Levinson et al.,* 2011; *Vera et al.,* 2012; *Parra et al.,* 2014].

Previous studies have highlighted the significance of SGDs to the quality of the groundwater and its dispersion (and resulting impact) on the coastal ecosystems [e.g., *Hernandez-Terrones*, 2010]. In karst terrains like the Yucatan peninsula, groundwater can become polluted by rain runoff, resulting in increased chemical (phosphorus and nitrogen) fluxes to lagoon reefs via SGD [*Mutchler et al.,* 2007; *Young et al.,* 2008; *Hernandez-Terrones*, 2010]. These increases in nitrogen and phosphorus in the lagoon can alter the ecosystem's health (e.g., seagrass) [*Carruthers et al.,* 2005] and cause phytoplankton and macroalgae blooms that change aquatic habitats [*Valiela et al*., 1990]. In addition, SGDs are typically more buoyant than lagoon waters due to their lower salinity. As a result, buoyant plumes discharging at the seabed rise quickly to the surface and are transported by lagoon flows. While these plumes can be monitored by dye or chemical tracers, the variability of their location within the water column has made it difficult to monitor their physical properties.

As a result, previous studies have focused on either lagoon circulation or submarine groundwater discharge. To date, studies have not investigated the interaction between lagoon flows and the SGD plume in the water column. The aim of this study is to address this limitation by identify mixing characteristics that can occur at fringing reefs as consequence of the interaction between two processes. A method is proposed to capture SGDs with respect to lagoon flows using a Sentinel V ADCP at a spring to evaluate the evolution of flow structures. To further investigate the energy associated with mixing in the water column, a turbulence analysis is conducted to close the turbulent kinetic energy (TKE) conservation equation. In addition, the role of water elevation in determining plume movement is assessed. The results of this study are the first of its kind to be presented for a shallow reef system.

Site Description

This study was conducted in a fringing reef lagoon in Puerto Morelos, Quintana Roo, Mexico (Figure 4-1), located on the northeastern coast of the Yucatan peninsula. The fringing reef at Puerto Morelos is approximately 4 km long along the coast and encloses a lagoon that varies in width from 500 to 1,500 m (Figure 4-1A). The shallow (3-4 m average depth) lagoon exchanges flow with the ocean via two inlets (north and center of the reef) and a navigation channel to the south. The northern inlet is ~1,200 m wide and 6 m deep; the central inlet is ~300 m wide and 6 m deep; and the navigation channel is ~400m wide and 8m deep. Roughly 10 km offshore, the shelf edge drops to >400 m [*Ruiz-Renteria et al.,* 1998]. The reef provides a unique habitat for coral and marine life, as well as shore protection by dissipating wave energy from deep-water waves. Tides in this region are small (<0.4 m range) and mixed, mainly semidiurnal with a form factor ~ 0.34. Easterly Trade Winds (typically 4-10 m/s) generate waves with an annual average significant wave height of 0.8 m and a typical period of 7 seconds [*Coronado et al.,* 2007]. Circulation in this microtidal region is driven by wave setup as waves break over the reef, with inflow occurring over the reef and outflow occurring at the inlets [*Coronado et al.,* 2007]. The wave-driven circulation results in strongest flows occurring at the inlet (~0.7 ms^{-1} outflow) and a well-mixed water column [*Coronado et al.,* 2007; *Chapter 2*].

Puerto Morelos bedrock lithology is dominated by highly permeable and soluble limestone. As a result, regional rainfall of 1,300 mm per year [Valle-Levinson et al., 2011] quickly percolates into the aquifer. Dissolution from the rain creates a maze of conduits. The elevation difference between the inland water table and ocean surface drives flows toward the ocean, resulting in SGDs in the form of bed seepage and point sources [*Valle-Levinson et al.,* 2011; *Null et al.,* 2014]. Puerto Morelos has numerous (10-15 identified) point source springs [*Parra et al.,* 2015] that discharge into the lagoon, allowing brackish water (~22 g/kg) to mix with lagoon water (36 g/kg). The submarine springs dominate seepage sources as the main contributor to SGD in the lagoon, accounting for roughly 79% of the total SGD [*Null et al.,* 2014]. The spring discharge depends on the water surface elevation (pressure head at spring), recharge due to pluvial input (pressure head inland), and morphology (surrounding bathymetry, depth, and orientation) of the spring vent [*Valle-Levinson et al.,* 2011; *Chapter 3*]. In Puerto Morelos, SGD has been observed to vary inversely with the semidiurnal microtide [*Valle-Levinson et al.,* 2011; *Parra et al.,* 2014 & 2015; *Chapter 3*], emphasizing the delicate balance between the aquifer and mean sea level.

Methodology

Data Collection

To study the interaction between lagoon flows and SGD, a Sentinel V20 (1000kHz) acoustic Doppler current profiler (ADCP) was secured next to a spring vent, locally known as Gorgos. Data were collected from September 11 to 17, 2014, during the wet period. The Sentinel V recorded velocity profiles (*u, v, w*) and pressure in 10-minute bursts at a sampling rate of 2 Hz every half hour with a 0.3 m vertical (bin) resolution. The fifth beam of the Sentinel V allowed vertical velocity to be captured directly along the z plane, as opposed to the horizontal velocities that are calculated from beam averaging. This unambiguous, high-resolution vertical velocity data allowed us to calculate turbulence in the water column near a SGD point, which has not been accomplished before.

Wind data (2 min. averaged, every 10 min.) were obtained from a meteorological station located on a pier at the National Autonomous University of Mexico (UNAM), approximately 1 km southwest of Gorgos.

Data Analysis

Pressure data were used to estimate one-dimensional wave spectra for each 10-minute data burst. The spectra were calculated using Welch's averaged periodogram method [e.g., *Emery and Thomson,* 2011], using Hanning windows with 50% overlap to reduce spectral leakage [e.g., *Pomeroy et al.,* 2012]. From these spectra the significant wave heights were calculated using the equation:

$$H_s = 4\sqrt{\sigma_p} \tag{4-1}$$

where σ_p is variance of the pressure spectrum. Significant wave heights were calculated for both short wave bands (frequency 0.04-0.2 Hz or period 5-25 s) and infragravity wave bands (frequency 0.004-0.04 Hz or period 25-250 s) according to *Roelvink and Stive,* [1989] and *Pomeroy et al.,* [2012].

In addition, burst velocity components (*u, v, w*) were separated into the mean ($\overline{u}$) and fluctuation (u') components through Reynolds decomposition as follows:

$$u = \overline{u} + u' \tag{4-2}$$

where $u = u\mathbf{i} + v\mathbf{j} + w\mathbf{k}$ represents the horizontal velocities toward the east as **i**, toward the north as **j**, and the vertical velocities as **k**. The fluctuations were used to calculate the components of the Reynolds stress tensor for both shear stresses (*u'v', u'w', v'w'*) and normal stresses (*u'u', v'v', w'w'*). To evaluate the turbulence behavior at the spring and in the water column, the components of the Reynolds stress tensor were used to estimate values of turbulent kinetic energy (TKE), turbulence production (P), and turbulence dissipation (ε).

Turbulence describes the irregular motion of velocity components with respect to space and time [*Trevor et al.,* 1998] and consequently helps explain mixing in near-shore environments [*Monismith,* 2010]. For this reason, the turbulent kinetic energy (TKE) associated with the flow fields is examined. The transfer of TKE is described by the components of its conservation equation as follows [*Pope,* 2000]:

$$\frac{Dk}{Dt} + \nabla \cdot T' = P - \varepsilon \quad \text{(4-8)}$$

where $\frac{Dk}{Dt}$ is the rate of change of TKE, *P* is TKE production, ε is TKE dissipation, and the second term is TKE transport (including buoyancy).

Turbulent kinetic energy (TKE) is defined as the sum of the mean squared velocity fluctuations (normal stresses) and represents kinetic energy per unit mass associated with turbulent flow eddies. Values of TKE at the springs were calculated as follows [*Pope*, 2000; *Monismith,* 2010]:

$$TKE = \frac{1}{2}\left(\overline{u'^2} + \overline{v'^2} + \overline{w'^2}\right) \quad \text{(4-3)}$$

Wave-turbulence decomposition was neglected based on the findings of *Bricker and Monismith* [2007]. Instruments with reliable compasses, tilt and pitch sensors, like the Sentinel V ADCP, produce a more dependable power spectrum than other methods of filtering or interpolating the wave frequencies [*Parra et al.,* 2015].

Rates of turbulence production and turbulence dissipation are two components of the TKE budget that determine transport of turbulent energy. Turbulence production values were estimated using raw beam velocity values according to the Variance Method [*Lu and Lueck,* 1999; *Stacey et al.,* 1999; *Rippeth et al.,* 2002; *Souza,* 2007]. This method calculates components of the Reynolds stress as:

$$\frac{\tau_x}{\rho} = -\overline{u'w'} = \frac{\overline{b_1'^2} - \overline{b_2'^2}}{4 sin\theta cos\theta} \quad \text{(4-4)}$$

$$\frac{\tau_y}{\rho} = -\overline{v'w'} = \frac{\overline{b_3'^2} - \overline{b_4'^2}}{4 sin\theta cos\theta} \quad \text{(4-5)}$$

where θ is the angle of the ADCP beam with the vertical (25 degrees for the Sentinel V). Using the Reynolds stresses, we calculate the rate of TKE production by multiplying terms from Equations 4-4 & 4-5 by the shears as follows [*Stacey et al.,* 1999]:

$$P = -\rho\left(\overline{u'w'}\frac{\partial\overline{u}}{\partial z} + \overline{v'w'}\frac{\partial\overline{v}}{\partial z}\right) \tag{4-5}$$

Rates of turbulence dissipation were estimated using a second order structure function used by *Wiles et al.,* [2006] as follows:

$$D(z,r) = \overline{(w'(z) - w'(z+r))^2} \tag{4-6}$$

where *D(z,r)* is the mean-square difference in velocity fluctuations at two points separated by a distance *r* (in meters). Previous applications of this equation have only used along-beam velocity data from the Janus (4-beam) ADCP configuration when studying ocean flows [e.g., *Wiles et al.,* 2006; *Souza* 2007]. A new way to apply the structure function (Equation 4-6) is proposed by using the fifth beam of the ADCP (along-beam velocity in the vertical axis), which allows direct computation of the vertical velocity fluctuation (*w'*) component of turbulence.

The length and velocity scales of isotropic eddies can be related using the Taylor cascade theory as follows [e.g., *Souza,* 2007]:

$$D(z,r) = C_v^2\varepsilon^{2/3}r^{2/3} \tag{4-7}$$

where C_v^2 is a constant (~2.1 for radar meteorology studies) [*Sauvageot*, 1992]. In addition to innovatively applying the vertical beam data to the structure function (Equation 4-6), this study uniquely calculates TKE dissipation rates at a point submarine groundwater discharge source for the first time to date.

Results

Atmospheric and Oceanic Conditions

Measurements at Gorgos were obtained during the Yucatan peninsula's wet season, when precipitation values averaged 6.5 mm/day, for a total of ~42 mm over the sampling period [*Chapter 3*]. Winds were moderate (7-8 m/s) and predominantly from the northeast, with the exception of an easterly pulse on September 14, 2014 (Figure 4-2A).

The influence of steady northeasterly winds coincides with the setup in the water surface elevation (η), as seen in the semidiurnal tidal signal in Figure 4-2B. The set up event (~5.5 day duration) was observed in the tidal elevation, starting on the 13th to the end of the sampling period. The tides transitioned from syzygy (spring) to quadrature (neap) on the 12th of September. However, as a result of the setup event, quadrature low tides exceeded syzygy high tides.

The atmospheric pressure oscillates at a 12-hour frequency, indicating the presence of atmospheric tides (Figure 4-2B). The difference in frequency between the oceanic tides (12.42 hours) and atmospheric tides (12 hours) causes the two pressures to be out of phase in the beginning of the experiment and in phase at the end. In addition, the atmospheric signal follows the setup observed in the water surface, η. This indicates that a weather event is likely the cause of the observed setups.

Significant wave heights varied between 0.2 and 0.4 meters during the experiment (Figure 4-2C). Periods of increased significant wave heights (>0.3 m) occurred on September 11-12th and September 14th-16th, which suggest periods when wave-driven circulation will be stronger.

Lagoon Flows and SGD

Discharge leaving the point source at the seabed is immediately affected by lagoon flows, particularly if the surrounding bathymetry does not provide protection [*Chapter 3*]. As a result of plume movement via lagoon flows, it is difficult to capture the SGD plume with only one instrument. For this reason the velocity profiles are first examined to determine when the ADCP captured the SGD plume and when the plume was out of range of the instrument. By examining the contours of velocity components (Figure 4-2), positive pulses in the vertical velocities are observed that are associated with the SGD, indicating moments when the plume is captured (e.g., Figure 4-2F). These pulses of positive vertical velocity also at times coincide with pulses seen in the horizontal components (Figure 4-2D&E).

The pulses observed in the velocity components do not occur at a specific frequency or appear to be modulated by the wind, water elevation, atmospheric pressure, or significant wave height signals (Figure 4-2). It is therefore necessary to examine the reason behind the intermittency of their behavior. To accomplish this, the depth-averaged velocities (smoothed 10 hours) are analyzed with respect to significant wave height (Figure 4-3A&B). Increased significant wave heights (>0.3 m) result in dominantly eastward-northeastward flows in the lagoon (September 11-12th and September 14th-16th). During these wave-driven periods, positive pulses in vertical velocity were only observed during relatively stronger (>0.1m/s) southeastward flows (blue boxes in Figure 4-3C-E). This observation suggests that during periods of wave-driven flows, the SGD plume is only captured when the flow is southeastward as a result of the ADCP being located to the southeast of the spring vent (confirmed by divers).

However, during periods of decreased significant wave height, flows in the lagoon became more susceptible to forcings other than wave-breaking induced (pressure gradient) setup. By examining periods of low Hs (September 13-14th and September 17th), it can be observed that the depth averaged flow components behaved erratically with respect to wave heights (Figure 4-3A&B). During these periods, positive pulses in vertical velocity reached maximum values and were present throughout the water column (Figure 4-2F). Figure 4-3C-E presents these pulses with respect to the depth-averaged components of flow (indicated by the red boxes). The depth-averaged vertical velocities reach maximum values when horizontal flows are minimum (e.g., September 17th). This result indicates that the SGD plume is fully captured by the ADCP during ‘slack’ tidal flows in the lagoon.

A schematic of the plume movement with respect to lagoon flows is presented in Figure 4-4. During periods of increased significant wave height (> 0.3 m), wave-driven circulation increases, causing the SGD plume to be captured by the instrument at depth, but carried away by the lagoon flows at the surface. During periods of decreased wave-driven lagoon flows (i.e., decreased Hs conditions), the SGD plume remains over the spring and is captured throughout the water column. Establishing conditions for SGD plume movement allowed for the further exploration and comparison of the mixing behavior of the lagoon flows and discharge flows. Turbulence parameters can help characterize flow behavior and are discussed in the following section.

Turbulence

To quantify the mixing characteristics in the water column the evolution of turbulent kinetic energy is analyzed (Figure 4-5B). Values of TKE range from 0.01 to >0.1 m^2s^{-2} with maximum values occurring near the bed (i.e., spring source), as expected due to the turbulent nature of SGDs. Values near the bed decrease as the subtidal η increases, indicating that SGD is modulated by the η setup (e.g., Chapter 3 Results & Conclusions). During the 'slack' lagoon flow conditions, high TKE (0.04 m^2s^{-2}) values are observed throughout the water column, coinciding with upward vertical velocity pulses (September 13-14th). During southeastward lagoon flows, high TKE (0.03 m^2s^{-2}) values are also observed in the water column, but overall, are weaker than during slack conditions (e.g., September 16th). This observation indicates that the SGD plume is significantly more turbulent (twice as much) than even strong (0.2 ms^{-1}) lagoon flows.

Values of TKE production varied throughout the experiment, with orders of magnitude ranging from 1 to 10^{-3} Wm^{-3} (Figure 3-5C). Peaks in TKE production are observed near the bed, where SGD is most likely to be captured by the ADCP. Peaks in production are also seen at the surface, which could indicate turbulence production from the wind or waves. However, the strongest surface values occur when the SGD plume is fully captured (i.e., during slack conditions). This result indicates that the SGD plume is the cause of the spikes in production rather than wind or wave input at the surface. It is worth noting that strong lagoon flows increase TKE production near the bed, as seen by the pulses of production on the 15th and 16th of September. The production values at Gorgos are in agreement with values estimated by *Exposito-Diaz et al.,* [2013] for another submarine spring in the Yucatan peninsula. They observed maximum production values of 0.98 Wm^{-3} during the dry season and predicted increased production values during the rainy season. The results at Gorgos confirm this hypothesis, with maximum production of ~1.5 Wm^{-3}, higher than the maxima observed by *Exposito-Diaz et al.* [2013].

Dissipation of TKE ranged from 0.5 to 10^{-3} Wm^{-3} (order of magnitude) over the experiment duration (Figure 3-5D). Strongest dissipation occurred at the bed, but was less than the values of TKE production. This indicates that the transport forcing term is needed to close the TKE budget (Equation 4-8). The imbalance between production and dissipation is exacerbated during periods of slack flows when the SGD plume is fully captured (e.g., September 13-14th). This heightened imbalance indicates that the transport mechanism of the TKE budget is likely increased due to the buoyant effects of the SGD plume that aid dissipation in balancing production. The relationship between production, dissipation, and buoyancy will be further explored in the Discussion.

The backscatter anomaly (BSA) represents the relative concentration of suspended material in the water column. Values of BSA are most intense near the bed, indicating high concentrations of suspended particles due to SGD. Pulses of increased BSA are also observed at the surface due increases in suspended material and bubbles from wind and wave action. The BSA at the bed is lower during periods of increased significant wave height (Hs) and higher during low Hs periods. Previous studies have shown that spring discharge is modulated by the semidiurnal tide, but have not shown the influence of changes in significant wave heights. However, the BSA results demonstrate the SGD plume dependency on the subtidal Hs rather than the subtidal water elevation, η. Indeed, upon examination of BSA with respect to the semidiurnal tidal signal (Figure 4-2B), it is clear that the BSA and vertical velocities are not inversely modulated by the semidiurnal tide as observed in Chapter 3 Results and Discussion.

This realization is likely due to the fact that the ADCP blanking distance prevents the instrument from capturing flows at the opening of the vent. As a result, the SGD plume is modulated more by Hs than tidal elevations once it leaves the constriction of spring vent, which modulates the discharge behavior through the piezometric balance (Chapter 3). With this in mind, it is valuable to explore the role of SGD modulation via changes in η on shorter time scales (e.g., minutes and seconds), which is discussed in the following section.

Discussion

Lagoon Flows and SGD

Analysis of the Results of the depth averaged flows (Figure 4-3) compared to the contours of flow with depth (Figure 4-2D-F) allow the following assumptions to be made:

1. Lagoon flows are typically dominated by eastward flows, due to east-west (u) magnitudes that are twice as high as the north-south flow magnitudes (v). This dominant flow pattern is due to the spring's proximity to the inlet, which favors outflow to the east (i.e., Chapter 2 Results & Conclusions).
2. During periods of high significant wave heights, the SGD plume is captured at depth when lagoon flows are strongly southeastward (as a result of instrument placement to the southeast of the spring vent). However, the plume is not observed at the surface because the strong eastward flows carry it out of the range of the instrument (i.e,, Figure 4-4 schematic).
3. During periods of lower significant wave heights, the SGD plume is still captured near the bed during strongly southeast flows. However, during slack lagoon flows, the SGD plume is observed throughout the water column, indicating that it remains over the spring (i.e,, Figure 4-4 schematic).

The above assumptions allow us to qualitatively hypothesize the movement of the SGD within the lagoon based on current conditions. For idealized inlets like the Boca Chica Inlet near Gorgos, lagoon circulation is driven by wave breaking induced setup that results in residual outflow at the inlet (Chapter 2 Results). In this scenario, the SGD (with very different chemical and biological composition than lagoon water) will be swiftly carried out of the lagoon via inlet outflows. However, it has been shown that asymmetry due to inlet length and dynamic bathymetry can cause inflow at the inlet, resulting in recirculation patterns within the lagoon (Chapter 2). These recirculation patterns imply the possibility of SGDs becoming trapped within the lagoon. The nutrient and pollutant rich SGDs can result in algae blooms and changes in lagoon pH that can potentially affect the corals at the reef. For these reasons, it is imperative to monitor SGD movement within lagoon systems that may be susceptible to recirculation patterns and increased flushing times.

Turbulence

Turbulence is a critical process that controls the vertical exchange of momentum within the water column [*Rippeth et al.,* 2001]. Understanding turbulence at SGDs is particularly essential because vertical exchanges are more intense due to buoyancy effects that contribute to turbulent flows. For the Gorgos experiment, it is expected that buoyancy forcing will play a significant role in mixing in the water column, particularly when the SGD plume remains over the spring. Unfortunately, density data were not available to calculate buoyancy forces during the experiment. However, results from the production and dissipation values allow the testing of the hypothesis of increased buoyancy during slack conditions when the SGD plume is fully captured.

Upon comparison of production to dissipation of SGD near the bed (Figure 4-5), it is clear that production values are larger than dissipation values. The following can mitigate the discrepancy between the two mechanisms:

- Buoyancy effects play a non-negligible role due to the salinity, and therefore, density differences between SGDs and the lagoon waters. Buoyancy will support dissipation in balancing production in the TKE balance [e.g., *Lueck,* 2015], and buoyant effects are expected to enhance the transport term in Equation 4-8, particularly when the SGD plume is fully captured.

- Values of C_V^2 are based on meteorological studies and tend to underestimate the dissipation rates [e.g., *Wiles et al.,* 2006; *Souza*, 2007]. This would also result in dissipation rates being underestimated with respect to production rates.

From Equation 4-8 the remaining transport term is estimated, which should be dominated by buoyancy [*Osborn and Cox*, 1972]. The result theoretically resolves the TKE budget and is presented in Figure 4-6. High values of transport are estimated near the bed to compensate for strong production of TKE. In addition, high transport values are derived at the surface, where wind and wave influence is the strongest. More importantly, at the surface, peaks in transport occur during periods of positive vertical velocity in the water column (Figure 4-6A). It is proposed that these peaks in the transport mechanism are a result of the buoyancy force that is theoretically strongly present in the SGD plume. This assumption aligns with observations of estuarine environments where the rate of change of TKE is driven by production, dissipation, and buoyant forcing [*Monismith*, 2010; *Osborn and Cox*, 1972; *Lueck*, 2015].

Role of Water Elevation in SGD Plume Movement

From the above results and discussion, it is clear that water surface elevation determines the behavior of SGD (e.g., Chapter 3). Studies have shown that SGDs at the spring are inversely related to tidal elevations, η, with strongest discharges occurring during low tides [*Parra et al.,* 2014; *Chapter 3*]. In these studies, η was shown to modulate SGD, with observations of high spectral energy in the gravity (<25 second period) and infragravity (>25 second period) frequency bands [*Parra et al.,* 2014; *Chapter 3*]. In addition, momentum forces are known to be influential at the spring vent as a result of the piezometric balance between pressure head gradients (Chapter 3) [*Chen and Rodi*, 1980; *Parra et al.,* 2014]. These studies, however, have not considered the behavior of plume movement once the SGD leaves the vent constriction. In the results section, it was observed that the plume becomes controlled by lagoon flows and buoyant forces play an increased role in turbulence mixing once the plume leaves the vent. To determine if the plume is still influenced by gravity and infragravity oscillations after leaving the vent, the relative spectral power in the water elevation and vertical velocities were examined. The results are presented in Figure 4-7.

The water surface elevation (η) spectrograph revealed high spectral energy in the swell (~12-20 second period) and infragravity (~30-120 second period) frequency bands. During periods of increased significant wave height (i.e., strong lagoon flows), the infragravity signal increased in strength and leaked to longer periods (~256 seconds) (e.g., September 15th). This result is expected since it is well known that an increase in water depth over the reef will allow an increase in the IG waves that propagate into the lagoon [*Pequignet et al.,* 2009; *Pomeroy et al.,* 2012; *Torres-Freyermuth,* 2012]. To confirm the presence of these low frequency IG waves, pressure data collected at the reef crest four days prior to the experiment at Gorgos were examined. Data were collected using an Aquadopp sampling at 2 Hz in 17-minute bursts every half hour. The power spectrum of η at the reef crest (Figure 4-8) demonstrates the modulation of IG waves by changes in water depth over the reef. During semidiurnal high tide, leakage occurred in the spectrum, allowing longer period IG waves to propagate into the lagoon.

Infragravity waves can be generated as a result of variations in radiation stresses associated with wave groups [*Longuet-Higgins and Stewart,* 1964] or by nonlinear interactions between incident swell and bathymetry [*Munk,* 1949; Herbers *et al.,* 1995]. Recent studies have further classified infragravity waves in the nearshore zone as “shoaling bound waves” [*Battjes et al.,* 2004] or “breakpoint-generated waves” [*Baldock,* 2012]. Shoaling bound waves are generated by nonlinear sea/swell waves (triad) interactions and are released from the wave group envelope during wave breaking [*Longuet-Higgins and Stewart,* 1962; *Pomeroy et al.,* 2012]. Breakpoint infragravity waves are generated by the variation in the breaking point (or intensity) within a wave group, resulting in changes in the radiation stresses that cause a dynamic setup that oscillates over time [*Symonds et al.,* 1982; *Pomeroy et al.,* 2012]. In addition, *Pomeroy et al.,* [2012] identified that IG waves generated by the “breakpoint variation” mechanism propagated shoreward and dominated short waves within the lagoon.

The relative dominance of the two generation mechanisms depends on the normalized slope parameter of the fore-reef [*Baldock,* 2012; *Pomeroy et al.,* 2012]. Research has shown that shoaling bound waves dominate mild slope (~1:70) beaches [*Janssen et al.,* 2003], while breakpoint-generated waves dominate steep slope (~1:10) beaches [*Baldock,* 2012; *Pomeroy et al.,* 2012]. The slope parameter for the fore-reef at Puerto Morelos varies from ~1:35 to ~1:75, as seen in the bathymetric map in Figure 4-1A. This suggests that the IG waves in Puerto Morelos are more likely generated by the breakpoint variation mechanism in steeper sloped areas. However, more data are needed to verify the infragravity wave generation mechanism at Puerto Morelos.

Regardless of the generation mechanism, infragravity waves at Puerto Morelos are present in the lagoon and provide a non-negligible contribution to the conservation energy balance [e.g., *Henderson et al.,* 2006]. IG waves are also dependent on water level changes over the reef [*Pomeroy et al.,* 2012]. As the water depth over the reef increases, energy at IG frequencies increases and leaks to lower frequency ranges (as seen in Figure 4-7 & Figure 4-8). In addition to increasing water depth over the reef, resonance can play a role in enhancing the energy associated with IG waves.

Previous work has shown that resonance can amplify the signals of incoming IG waves for wavelengths that are a multiple of the basin length [e.g., *Lugo-Fernandez et al.,* 1998; *Pequignet et al.,* 2009]. This basin resonance phenomenon [*Proudman,* 1953; *Mei*, 1983] results in the excitation of basin resonance modes similar to the IG oscillation periods [e.g., *Lugo-Fernandez et al.,* 1998]. Resonance excitation can also occur on coral reef platform scales as well as the longer shelf scales [e.g., *Lugo-Fernandez et al.,* 1998; *Pequignet et al.,* 2009]. To further analyze the potential influence of resonance excitation, the natural resonance period of the shelf and reef can be estimated and compared to IG frequencies observed in the η power spectrum at the reef crest and vertical velocities at the spring. The resonance period is estimated as follows [e.g., *Lugo-Fernandez et al.,* 1998]:

$$T = \frac{4L}{\sqrt{gh}} \tag{4-9}$$

where *L* is the length of the reef or shelf, *g* is the gravitational acceleration, and *h* is the depth of the reef or shelf. With *L*= 2900 m and *h*= 50 m, the shelf resonance period is approximately 8.7 minutes (~520 seconds). Using a varying reef width of 80 to 100 m and a depth of 1.7 m, the natural period of the reef varies between 78 and 98 seconds. In Figure 4-8, it can be observed that just before the start of the experiment, oscillations at the natural resonance period of the shelf and reef propagate into the lagoon. The IG waves may be excited by the modes of the natural resonance periods of the shelf and of the reef, which would result in their amplification.

With the confirmation of infragravity wave presence in the lagoon, it should be evaluated how these low frequency oscillations affect SGD plume movement. To determine the IG influence, the spectral power of vertical velocity was examined (Figure 4-7B-D). The spectral energy of the vertical velocity was calculated for the surface, middle of the water column, and near the bed. Since lagoon flows influence plume movement, the periods of higher significant wave height and stronger wave-driven lagoon flows were examined first (September 11-12th and September 14-16th). During these periods, the increase in IG frequencies near the bed (Figure 4-7D) corresponds to the increase in IG frequencies observed in η (Figure 4-7A). However, in the middle of the water column (Figure 4-7C) and near the surface (Figure 4-7B), IG frequencies are almost entirely absent. An explanation for this behavior is seen in the vertical velocity values, where values near the bed are greater than the depth averaged and surface values (Figure 4-3E). This realization indicates that the ADCP captures SGD near the bed even during periods of high significant wave height. Therefore the IG oscillations seen closest to the spring are a result of the SGD plume oscillating at low frequencies.

This hypothesis is confirmed when 'slack' lagoon conditions are evaluated, which allow the SGD plume to develop over the spring. As expected, IG oscillations are observed in the SGD plume in the middle and near surface of the water column (September 13-14th and September 17th). However, upon closer examination of the vertical velocity spectral power, it is clear that the IG signal in the water elevation does reach the low frequencies (>256 second period) observed in the IG signal in the plume.

To offer an explanation as to why the plume oscillates at low frequencies that are not observed in η, buoyancy forcing is examined with respect to turbulent jet behavior.

The Puerto Morelos point discharge sources can be classified as ‘buoyant jets (forced plumes)’ according to *Chen and Rodi,* [1980]. For these types of discharge sources, the forced jet behave like a non-buoyant jet at the spring vent, but develops into a buoyant plume through an ‘intermediate region’ [*Chen and Rodi,* 1980]. To calculate the length of this intermediate region, the following equation was applied according to the similarity and scaling laws proposed by *Chen and Rodi,* [1980] (pg. 25):

$$0.5 \leq F^{-2/3}\left(\frac{\rho_0}{\rho_a}\right)^{-1/3}\frac{x}{D} \leq 5 \tag{4-10}$$

where *F* is Froude number that compares inertial to buoyant forces [*Chen and Rodi,* 1980, pg. 9], ρ_0 is the density of water at the spring vent, ρ_a is the ambient (lagoon) water density, and *D* is the diameter of the jet opening.

The Froude number used in Equation 4-10 was calculated from the following equation [*Chen and Rodi,* 1980, pg. 9]:

$$F = \frac{U_0^2}{gD(\rho_a - \rho_0)/\rho_0} \tag{4-11}$$

where *U* is the jet velocity, *g* is gravitational acceleration, and the other terms remain the same. Equation 4-11 inputs were a velocity of 0.4 m/s (according to the velocity data obtained from the ADV in Chapter 3), a diameter of 0.8 m, an ambient density of 1026 kgm^{-3}, and a spring density of 1015 kgm^{-3}. This results in a Froude number for Gorgos of 1.88 (for the maximum discharge velocity of 0.4 m/s). Applying this Froude number to Equation 4-10, the limits for the intermediate region of the plume were calculated, resulting in a transition zone between 0.61 and 6.1 meters.

Upon comparing the established length thresholds of the intermediate region to the water column depth, it is obvious that the transition zone occupies the majority of the water column. For this reason, it is appropriate to assume that the integral length scale of the eddies in the SGD plume can reach lengths of the full water column depth ~6 m [*Chen and Rodi,* 1980; *Lueck,* 2015]. As a result, the over-turning time of eddies associated with SGD can be calculated by dividing the integral length scale (~6 m) by the velocity near the spring. The vertical velocities ranged from 0.025 to 0.15 m/s in the SGD plume (Figure 4-4A), resulting in an overturning time ranging between 40 to 240 seconds. It is therefore proposed that the low frequency oscillations observed in the vertical velocity power spectra (Figure 4-7B-D) result from the SGD plume overturning due to buoyant effects.

Mixing Time Scales

The previous discussion has focused on circulation and mixing at subtidal timescales. While it is important to determine the overall behavior of the system, mixing on shorter timescales give insight to other mechanisms that modulated SGD movement. In particular, if the focus remains on periods when the SGD plume is fully captured in the water column, the IG modulation of the plume at high temporal resolutions can be examined. To accomplish this, vertical velocity and backscatter anomaly (BSA) were compared to a low pass (60 second) filter of η for a 10-minute burst of data (September 13, 2014, 02:00) when the SGD plume is captured (Figure 4-9). Upon comparison, it is evident that the SGD plume is modulated by the infragravity oscillations in the η. During transition periods from wave trough to wave crest, positive vertical velocity values extend further in the water column. Conversely, during the transition from wave crest to wave trough, positive vertical velocities remain closer to the bed. This behavior is also observed in the BSA contours.

This circulation pattern contrasts the typically expected η modulation of spring discharge. As previous research has shown, discharge at the spring vent reaches maximum values during low η and minimum values during high η due to the pressure gradient between the inland water elevation and sea level. However, once the plume has left the constriction of the spring vent, it is no longer modulated by a pressure head gradient. Instead, results in Figure 4-9 suggest that the particle motion caused by a progressive leftward propagating IG wave modulates the SGD plume. To illustrate this notion, Figure 4-9D presents a schematic of a particle motion under a progressive, linear wave. Previous work has shown that IG wave propagation in fringing reef lagoons is predominantly shoreward [e.g., *Pomeroy et al.,* 2012]. This is due to frictional dampening over the reef, which decreases the strength of reflected seaward IG waves. Based on this result, it is reasonable to propose that the SGD plume movement will be modulated by shoreward propagating IG waves. Indeed, the periodicities of pulses in vertical velocity match the periods of high IG oscillations in the η spectrograph on September 13th (Figure 4-7).

This burst analysis demonstrates that the SGD plume movement is modulated by IG waves in η. In addition, longer period infragravity oscillations are observed in the SGD plume on a subtidal scale. These results demonstrate the importance of considering low frequency modulation of SGD plume movement within a fringing reef lagoon.

Lagoon and SGD Interaction Conclusions

For wave-driven circulation systems, significant wave height is the main cause of SGD movement within a fringing reef lagoon. During periods of high Hs, lagoon flows are dominantly wave-driven, which carry the SGD plume toward the sea via inlet outflows. When wave height decreases, so does the wave-driven circulation, which allows the SGD plume to remain over the discharge source. In these moments, turbulence generated as a result of SGD is stronger than turbulence generated by lagoon flows, resulting in higher mixing of nutrient rich SGDs. Mixing via turbulent kinetic energy was dependent on production, dissipation, and transport (i.e., buoyant forcing). While momentum forces may dominate the SGD at the vent, buoyant forces likely become non-negligible turbulence transport mechanisms past the vent opening. It is suggested that future studies examine the impact of this component in the TKE conservation equation. In addition, the agreement found using the Variance Method to calculate production and Structure Function to calculate dissipation demonstrates the reliability of the findings with a 5 beam ADCP to capture SGD in future fieldwork.

This study highlighted the importance of infragravity and low frequency oscillations in modulating SGD plume movement. Infragravity waves were observed at the spring and had similar frequencies to modes of shelf and/or reef resonance frequencies that propagated past the reef crest during elevated water depth. These shoreward propagating IG waves seen in the water elevation were found to move the SGD plume water mass according to linear wave theory. In addition to IG waves in the lagoon, low frequencies oscillations were observed in the SGD plume itself as a result of eddy overturning due to buoyancy. These results demonstrate that low frequency oscillations modulate of SGD plume movement within a fringing reef lagoon.

It is critical to understand the transport of SGDs at a local (spring discharge point) scale and at a basin scale (lagoon-inlet system). For idealized inlets like the Boca Chica Inlet near Gorgos, lagoon circulation is driven by wave breaking induced setup that results in residual outflow at the inlet. In this scenario, the nutrient (or pollutant) rich SGD will be swiftly carried out of the lagoon via inlet outflows. However, if the lagoon-inlet systems have recirculation patterns (e.g., Boca Grande, Chapter 2), SGDs can become trapped within the lagoon. The nutrient and pollutant rich SGDs can result in algae blooms and changes in lagoon pH that can potentially kill the corals at the reef. For these reasons, it is imperative to monitor SGD movement within lagoon systems, particularly those that may be susceptible to recirculation patterns and increased flushing time

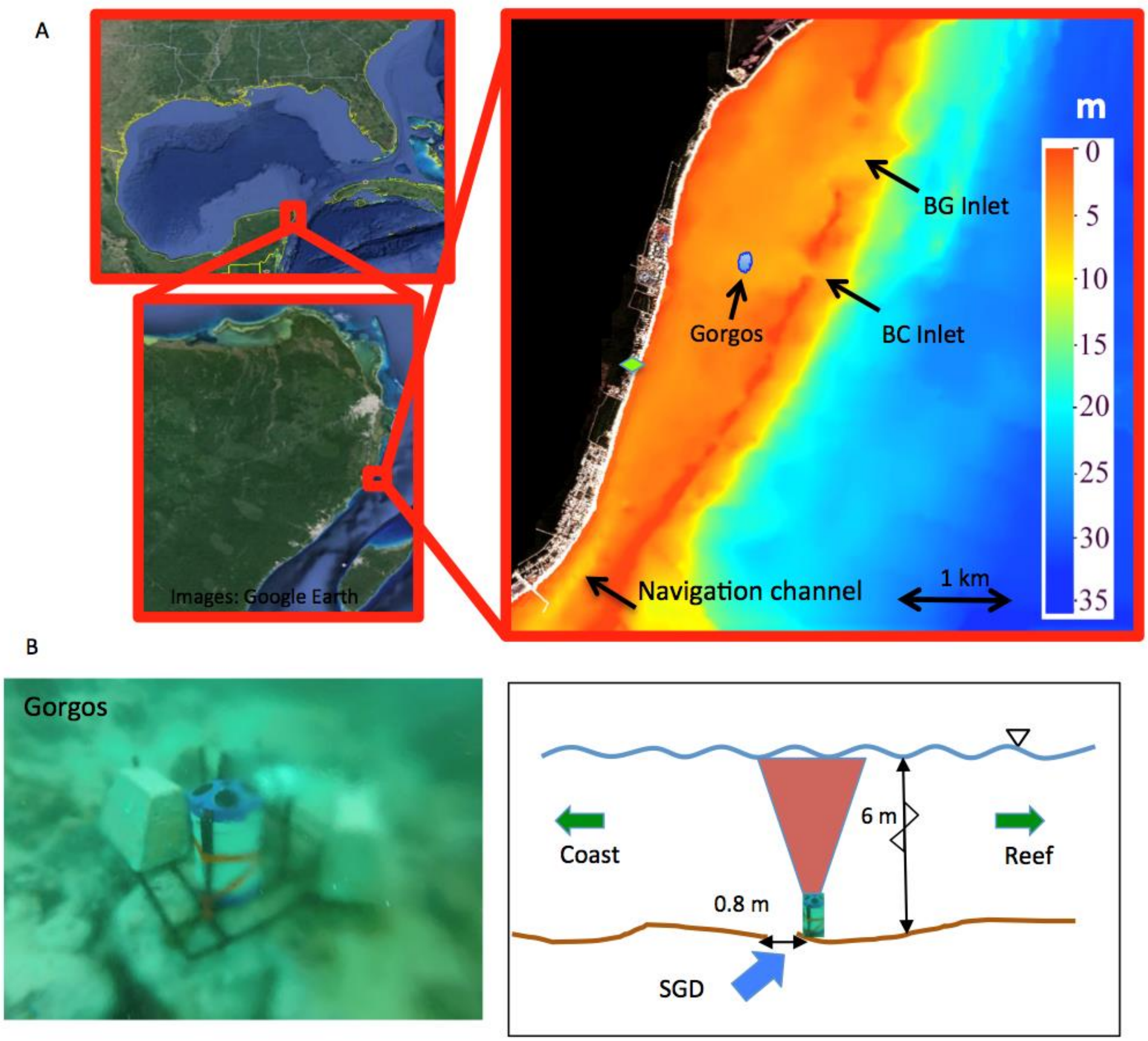

Figure 4-1. Site location and instrumentation configuration. A) Geographic reference: Puerto Morelos, Quintana Roo, Mexico. The Puerto Morelos fringing reef is located on the NE coast of the Yucatan peninsula. There are two inlets: Boca Grande to the north and Boca Chica in the center of the reef. A navigation channel is located at the southern end of the lagoon. B) Gorgos instrument placement (left) with reference to spring bathymetry/dimensions (right).

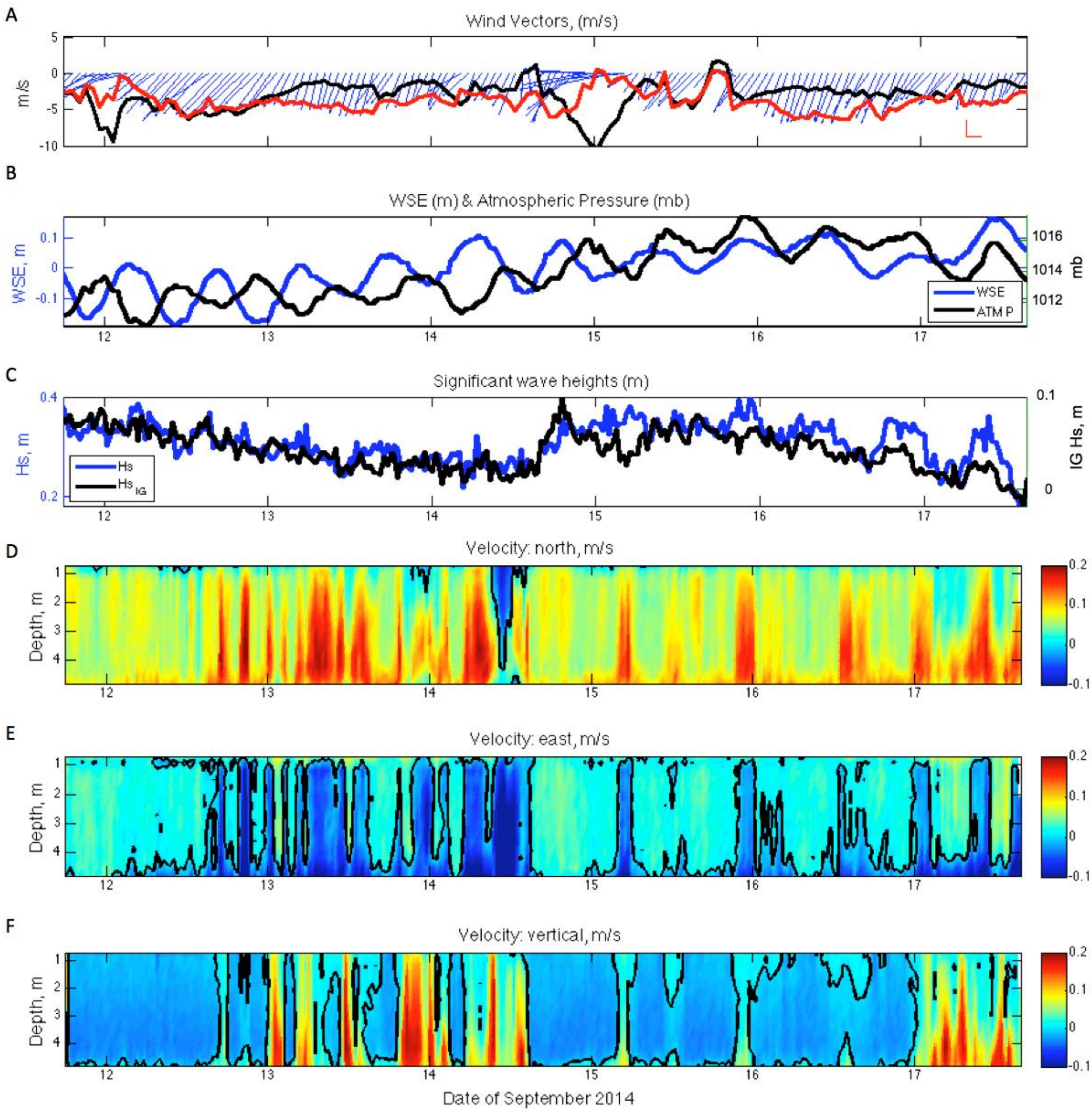

Figure 4-2. Atmospheric and oceanic conditions during experiment. A) Wind conditions: vectors (blue), East-West magnitude (black line), North-South magnitude (red line) demonstrate wind origin. B) Water surface elevation (left axis) and atmospheric pressure (right axis). C) Significant wave height (Hs) of swell (5-20 seconds) indicated by the blue line (left axis) and Hs of infragravity waves (25-200 seconds) indicated by the black line (right axis). (D) U (East-West) velocity component contour (East, positive) E) V (North-South) velocity component contour (North, positive) F) Vertical velocity component (up, positive).

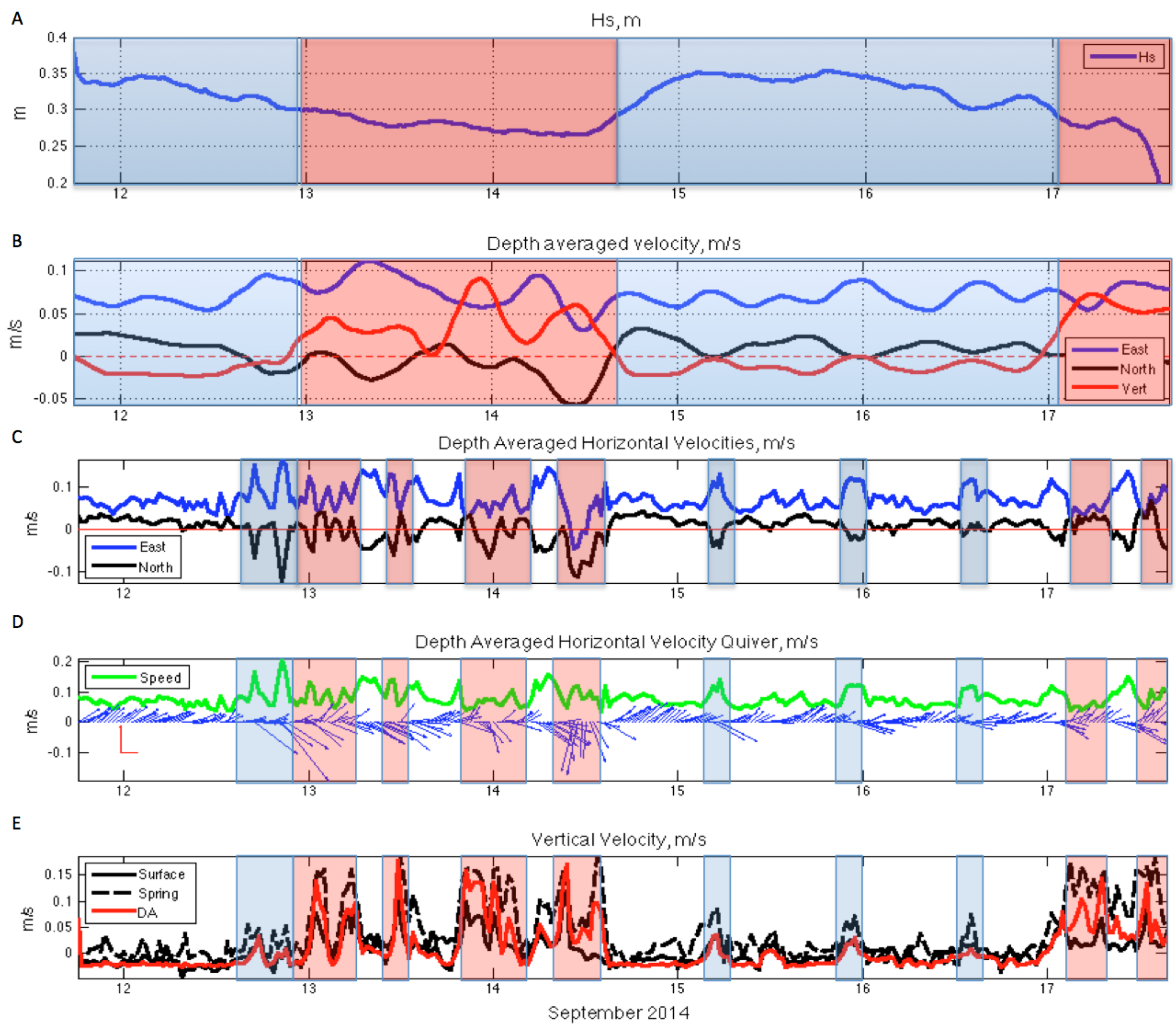

Figure 4-3. Wave-driven circulation conditions. Comparison of (A) Subtidal (30-hour smoothed) significant wave height to (B) Subtidal depth averaged velocity components. Blue shaded boxes indicate Hs> 0.3 m (strongly wave-driven circulation). Red shaded boxes indicate Hs< 0.3 m (weakly wave-driven circulation. Subplots C-E present a comparison of horizontal velocity components to the vertical velocity component. (C) Shows the depth averaged U (blue) and V (black) components of flow. (D) Presents the horizontal vectors and magnitude (E) Displays the vertical velocity at the surface (solid black line), near the spring (dashed black line), and averaged with respect to depth (red line). The red and blue boxes in C-D indicate moments when the discharge plume is captured, as indicated by the high positive vertical velocity values in E.

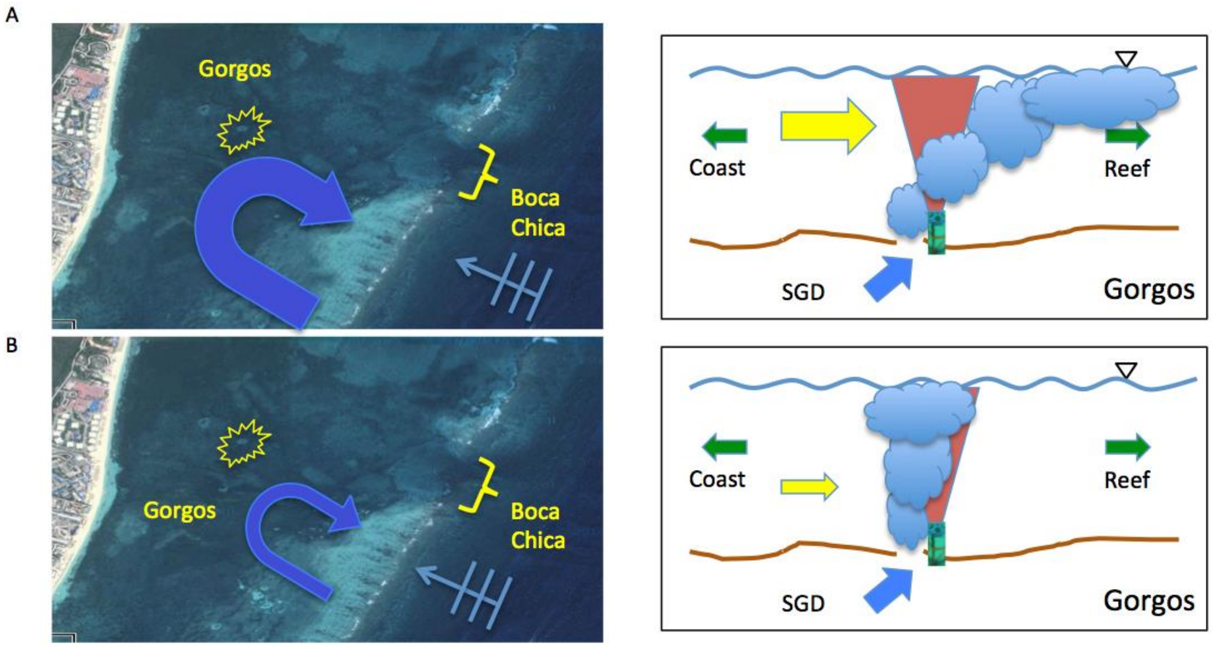

Figure 4-4. Wave-driven circulation conditions that control SDG plume movement. A) High significant wave height conditions (Hs > 0.3 m) result in the submarine groundwater discharge (SGD) plume being carried away from the spring. B) Low significant wave height conditions (Hs < 0.3 m) result in the SGD plume to remain over the spring, allowing the ADCP to capture the plume as it develops in the water column.

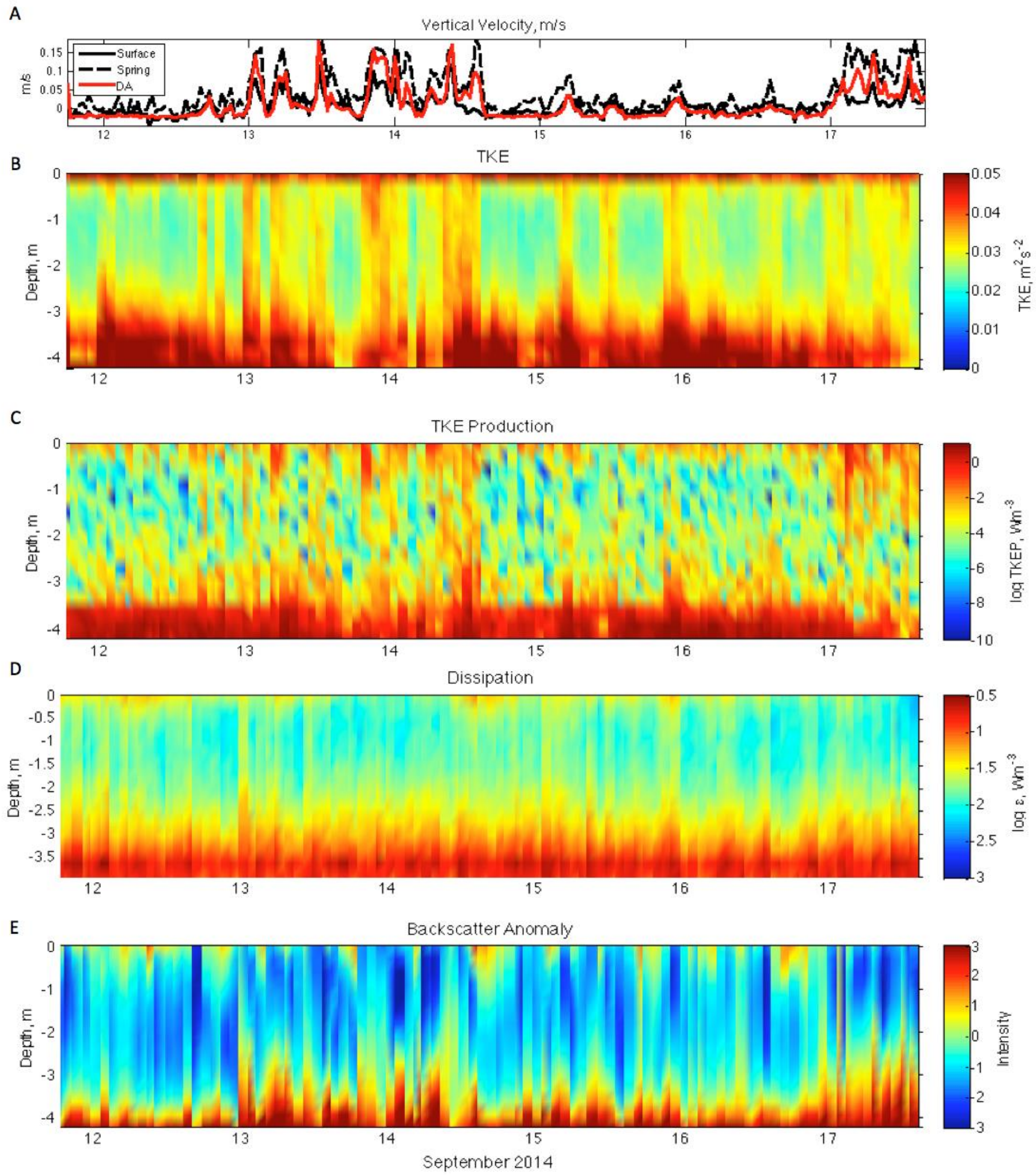

Figure 4-5. Turbulence characteristics. A) Presents a reference to vertical velocities at the surface, near the spring, and depth-averaged. The following are contour plots with respect to water column depth. B) Turbulent Kinetic Energy (TKE). C) TKE Production D) TKE Dissipation E) Backscatter Anomaly. Highest values are observed near the bed, closest to the discharge point. Influence from winds/waves create periods of increased turbulence at the surface.

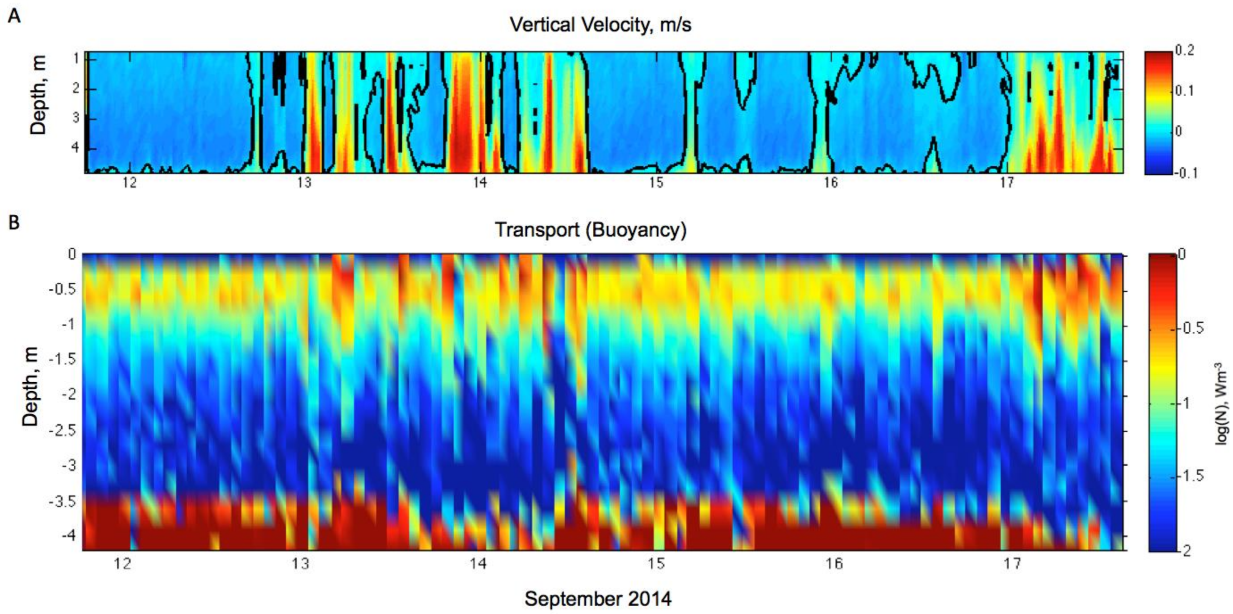

Figure 4-6. Estimate of buoyancy transport term from closing the TKE conservation equation. (A) Presents vertical velocity contours to highlight periods when the discharge plume is captured, indicated by strong positive values (red). (B) Demonstrates the closure of the TKE conservation equation. High transport values are observed at near the bed as a result of proximity to the discharge source. High values are also seen at the surface during moments when the plume is fully captured, confirming the expectation that buoyancy dominates the transport term [*Pope,* 2000; *Lueck,* 2015].

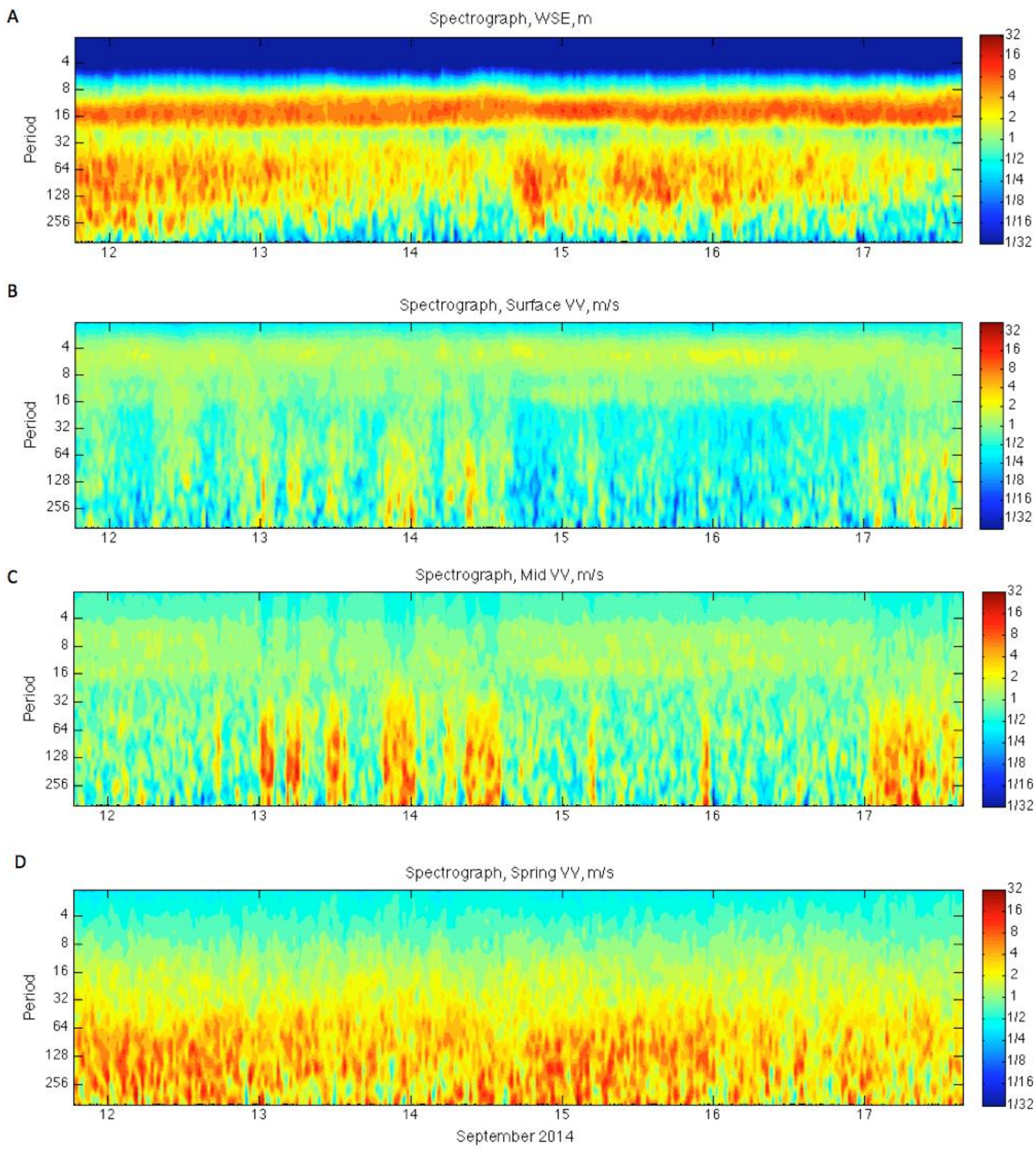

Figure 4-7. Spectrograph of Water Surface Elevation (WSE) η and vertical velocities. The following subplots demonstrate the relative power in the signals with respect to frequency (periods in seconds) and experiment duration. A) Spectrograph of η indicating high energy in the swell (10-20 s period) and infragravity (> 30 s period) bands. B-D) Vertical velocity spectrographs at the surface (B), mid-water column (C), and near the spring bed (D). High energy (red) at infragravity frequencies (> 60 s period) is observed during 'slack' lagoon flow conditions throughout the water column.

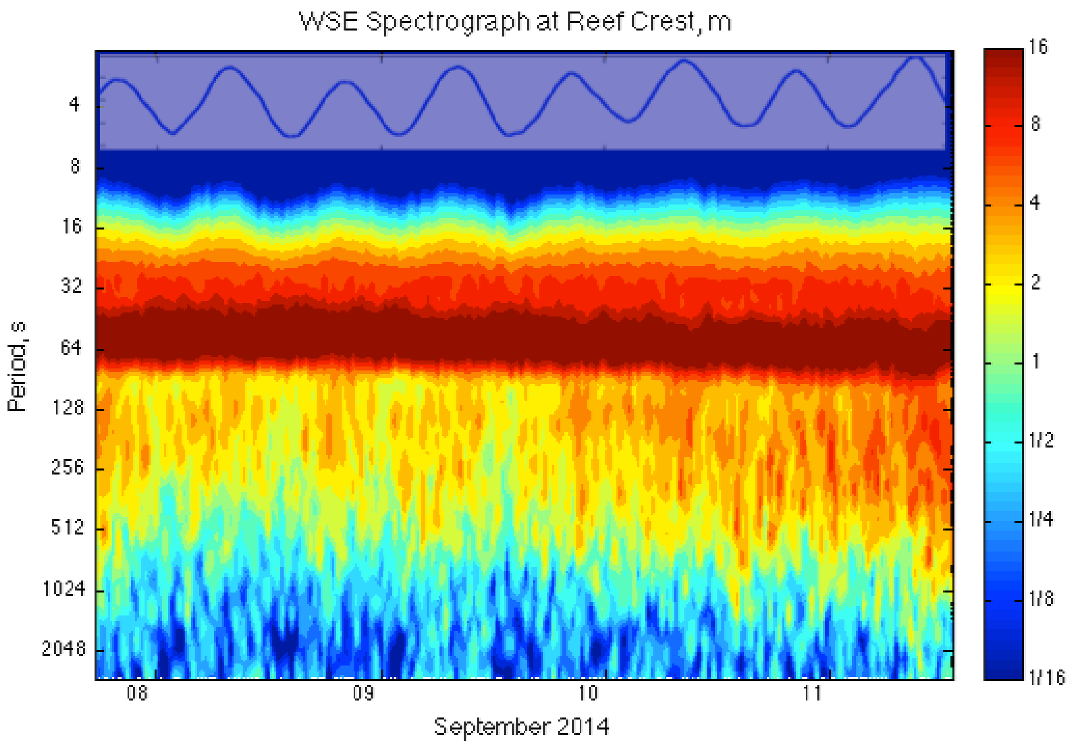

Figure 4-8. Spectrograph of the water surface elevation at the reef crest. The spectrograph illustrates high energy in the infragravity wave frequencies (40-80 s periods). Spectral leakage to lower frequencies is observed starting on September 10th that corresponds to an increase in depth over the reef. The light blue line (top) represents the tidal range that appears to modulate the spectral leakage.

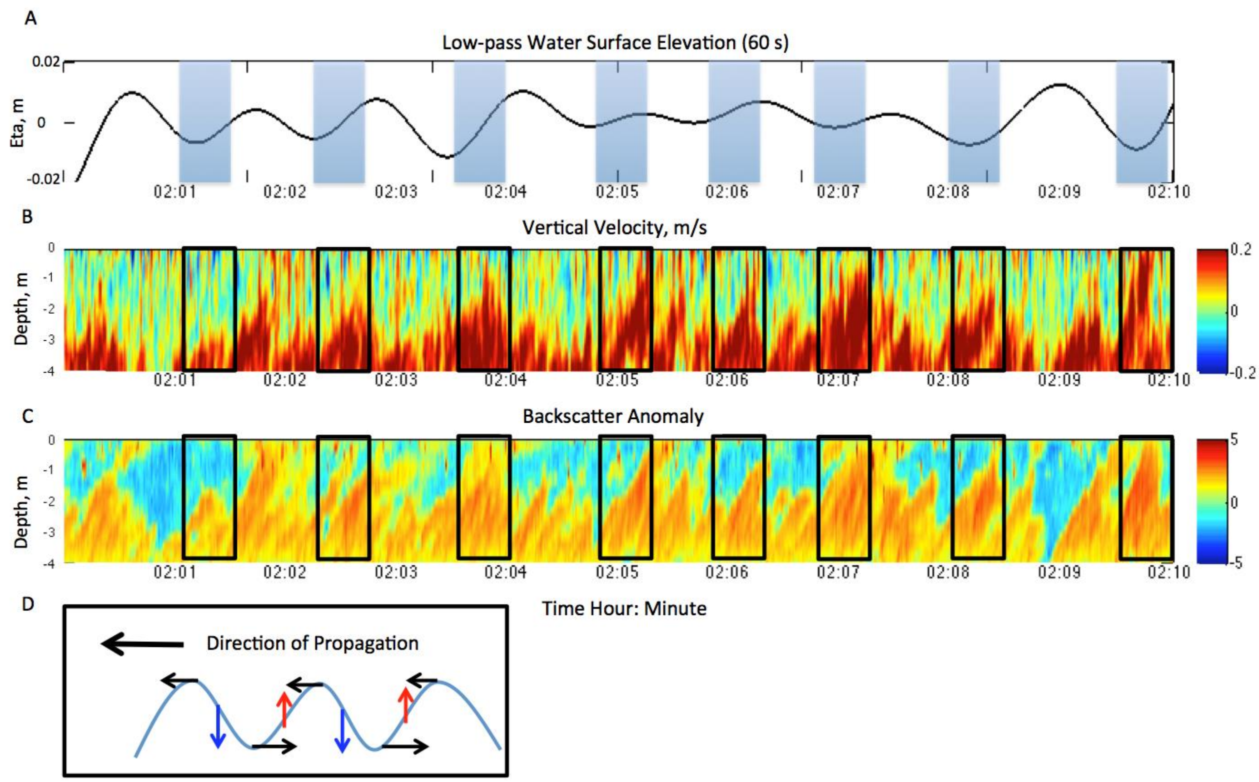

Figure 4-9. Infragravity wave influence on discharge plume movement. Analysis of 10-minute data burst of A) Water surface elevation (low pass filtered, 60 s) B) Vertical velocity C) Backscatter anomaly (BSA) on September 13, 2014. The black boxes in the BSA and vertical velocity show the movement of the SGD plume mass (high vertical velocities and high BSA values). The plume movement precedes the surface wave crest as indicated by the blue boxes. To explain this behavior a D) Schematic of particle motion under a progressive linear wave is presented. Once the plume leaves the constriction of the jet, the water mass will behave according to linear wave theory. In this case, modulated by the shoreward propagating infragravity waves in the lagoon-reef system.

CHAPTER 5
CONCLUSIONS

Tidal and Residual Circulation

Inlet circulation in the same larger lagoon system can behave very differently, despite geographic proximity. These notable differences stem from variations in tidal water surface elevation, bathymetry, wind conditions, wave height, and inlet width. The results of the two experiments show that tides can significantly influence the circulation patterns observed in shallow reef lagoons, even in microtidal regimes. For mixed tidal regions, a kinematic analysis of the flow fields can produce different results for inlets in close proximity (<1 km) based on the total water surface elevation, including tides and waves. Bathymetry and inlet width must also be considered when analyzing flow patterns at reef breaks. Increases in inlet width and variation in its bathymetric structure will cause more complex vertical structure of flow at the inlets. In some cases, inflow can overcome the favored seaward flow and recirculation patterns have the opportunity to develop.

The findings of these studies modify the typically accepted circulation patterns in shallow reef systems by identifying inflow at an inlet edge and lagoon recirculation patterns in the residual flows of Boca Grande, a long-narrow inlet. Furthermore, a simplistic approach to determine whether an inlet system is susceptible to cyclonic formation was proposed by comparing inlet length to local radius of curvature as a proxy comparison for advection to local accelerations. While these results are only reliable near the inlet, they present a means of classifying inlet systems that may be susceptible to gyre formation. A method of identifying areas of non-linear flow behavior has also been presented by comparing the spatial calculations of advection to local accelerations, indicating areas of recirculation or dispersion. This concept has significant implications for reef health management and sustainability in the form of predicting pollutant and nutrient traps as well as identifying areas of higher flushing times.

SGD and Turbulence

Despite geographic proximity, submarine groundwater discharge (SGD) behavior can vary widely between springs. The results of this paper support the significance of the pressure head gradient driving discharge. Changes in recharge (due to rain or anthropogenic consumption) determine if saltwater intrusion events (backflow) could occur based on relatively small changes (<0.3 m tidal range) in the water surface elevation, η.

Seasonal climate patterns affect SGDs by controlling recharge. During dry seasons (Pargos), water elevation was the dominating mechanism for SGD, TKE, and temperature modulation on tidal and subtidal time scales. During the wet season (Gorgos), semidiurnal oscillations in the water elevation modulated SGD and TKE on shorter time scales (~12.42 hr), but pluvial input and across lagoon flows became influential factors in the subtidal signal. In addition to pluvial input, the spring geomorphology plays a significant role in SGD and turbulence behavior. In geologically mature springs, like Pargos, turbulence fields develop relatively free from the influence of currents in the lagoon. Conversely, SGDs at unprotected spring vent geomorphology are subject to lagoon flows that can result in an anisotropic turbulence field.

For Pargos (isotropic turbulence), dissipation behavior increases exponentially with increasing SGD velocity. Peaks in dissipation occur at maximum vertical velocities (syzygy low tide). During these periods, the inertial subrange shifted to higher frequencies. The high sampling rate of the ADV the resolution to capture the highest frequencies of the inertial subrange shifts. This result suggests that for future research, a sampling rate of at least 16 Hz is needed to fully capture the inertial subrange behavior over the spring-neap cycle.

A novel approach was presented to estimate turbulence dissipation rates, using only pressure data at a spring and inland source. Future studies in the area should consider implementing this method when instrumentation for other methods of calculating turbulence dissipation is unavailable. This method would be especially useful for evaluating dissipation behavior over significantly longer time scales (~months).

The global significance of these findings will help classify and predict discharge and turbulence behavior at coastal SGD sources. Understanding the relationship between these processes is of vital importance to the health of system. It predicts occurrences of backflow (into the spring), determining when salt intrusion may pose a threat to fresh groundwater resources. In addition, mixing via SGD and turbulence gives valuable insight to the transport and concentrations of nutrients, pollutants, and microbial species in the lagoon. Whether SGDs need to be monitored for SWI or investigated as potential energy sources, it is vital to understand these systems

Lagoon and SGD Interactions

For wave-driven circulation systems, significant wave height is the main cause of SGD movement within a fringing reef lagoon. During periods of high Hs, lagoon flows are dominantly wave-driven, which carry the SGD plume toward the sea via inlet outflows. When wave height decreases, so does the wave-driven circulation, which allows the SGD plume to remain over the discharge source. In these moments, turbulence generated as a result of SGD is significantly stronger than turbulence generated by lagoon flows, resulting in higher mixing of nutrient rich SGDs. Mixing via turbulent kinetic energy was dependent on production, dissipation, and transport (e.g., buoyant forcing). While momentum forces may dominate the SGD at the vent, buoyant forces become non-negligible turbulence transport mechanisms past the vent opening. It is suggested that future studies examine the impact of this component in the TKE conservation equation. In addition, the agreement found using the Variance Method to calculate production and Structure Function to calculate dissipation demonstrates the reliability of our findings and promotion for using a 5 beam ADCP to capture SGD in future fieldwork.

These study highlighted the importance of infragravity and low frequency oscillations in modulating SGD plume movement. The discharge plume oscillated at low frequencies due to the overturning time of eddies created by the forced buoyant spring jet. In addition, shoreward propagating IG waves seen in the water elevation were found to move the SGD plume according to linear wave theory. These results demonstrate that low frequency oscillations modulate of SGD plume movement and should be considered in future field studies in fringing reef lagoons.

It is critical to understand the transport of SGDs at a local scale (spring discharge point) and at a basin scale (lagoon-inlet system). For idealized inlets, like the Boca Chica Inlet near Gorgos, lagoon circulation is driven by wave breaking induced setup that results in residual outflow at the inlet. In this scenario, the nutrient (or pollutant) rich SGD will be swiftly carried out of the lagoon via inlet outflows. However, if the lagoon-inlet systems have recirculation patterns, SGDs can become trapped within the lagoon. The nutrient and pollutant rich SGDs can result in algae blooms and changes in lagoon pH that can potentially kill the corals at the reef. For these reasons, it is imperative to monitor SGD movement within lagoon systems, particularly those that may be susceptible to recirculation patterns and increased flushing times.

APPENDIX
EQUATION REFERENCES

Lateral Momentum Balance Terms, (U, V)

Local Acceleration: $\frac{\partial u}{\partial t}$, $\frac{\partial v}{\partial t}$ (a)

Advective Acceleration: $u\frac{\partial u}{\partial x} + v\frac{\partial u}{\partial y}$, $u\frac{\partial v}{\partial x} + v\frac{\partial v}{\partial y}$ (b)

Coriolis Acceleration: $-fv$, uf (c)

Where, $f = 2\Omega\sin(\varphi)$,

and φ is the reference latitude and Ω is the planetary rotary frequency

Bed Frictional Acceleration: $C_d UV$, $C_d VU$ (d)

LIST OF REFERENCES

Andrews J. C., and G. L. Pickard (1990), The physical oceanography of coral reef systems, In Ecosystems of the World, *Coral Reefs*, ed. Z. Dubinsky, 11–45, Amsterdam: Elsevier, 550 pp.

Baldock, T. E. (2012), Dissipation of incident forced long waves in the surf zone—Implications for the concept of “bound” wave release at short wave breaking, *Coastal Eng.*, 60, 276–285, doi: 10.1016/ j.coastaleng.2011.11.002.

Battjes, J. A., H. J. Bakkenes, T. T. Janssen, and A. R. van Dongeren (2004), Shoaling of subharmonic gravity waves, *J. Geophys. Res.,* 109, C02009, doi:10.1029/2003JC001863.

Beddows, P. A., P. L. Smart, F. F. Whitaker, and S. L. Smith (2007), Decoupled fresh–saline groundwater circulation of a coastal carbonate aquifer: Spatial patterns of temperature and specific electrical conductivity*, J. Hydrol.,* 346(1), 18–32.

Bricker, J. D., and S. G. Monismith (2007), Spectral wave-turbulence decomposition, *J. Atmos. Oceanic Technol.,* 24(8), 1479–1487.

Carruthers T. J. B., B. I. van Tussenbroek, and W. C. Dennison (2005), Influence of submarine springs and wastewater on nutrient dynamics of Caribbean seagrass meadows, *Est Coast Shelf Sci.,* 64:191−199.

Chen C. J., and W. Rodi (1980), *Vertical turbulent buoyant jets: a review of experimental data*. Pergamon, Oxford.

Coronado, C., J. Candela, R. Iglesias-Prieto, M. Sheinbaum, M. López, F. J. Ocampo-Torres (2007), On the circulation in the Puerto Morelos fringing reef lagoon, *Coral Reefs* (26):149–163, doi 10.1007/s00338-006-0175-9.

Dean, R. G., and R. A. Dalrymple (1991), *Water Wave Mechanics for Engineers and Scientists, Adv. Ser. Ocean Eng*., vol. 2, World Sci., Hackensack, N. J.

Emery, W. J., and R. E. Thomson (2001), *Data Analysis Methods in Physical Oceanography,* 1st ed., Elsevier, N. Y.

Enriquez, C., I. Marino-Tapia, A. Valle-Levinson, A. Torres-Freyermuth, and R. Silva-Casarin (2012), Mechanisms driving the circulation in a fringing reef lagoon: a numerical study, In: *Book of Abstracts of the Physics of Estuaries and Coastal Seas Symposium*, edited by B. Chant and R. Geyer, 29 pp., N. Y.

Exposito-Diaz, G., M. A. Monreal-Gomez, A. Valle-Levinson, and D. A. Salas-de-Leon (2013), Tidal variations of turbulence at a spring discharging to a tropical estuary, *Geophys. Res. Lett*., 40, 898–903, doi:10.1002/grl.50194.

Gargett, A. E. (1999), Velcro measurement of turbulence kinetic energy dissipation rate epsilon, *J. Atmos. Oceanic Technol.,*16 (12), 1973–1993.

Gonzalez-Herrera, R., I. Sanchez-y-Pinto, and J. Gamboa-Vargas (2002), Groundwater-flow modeling in the Yucatan karstic aquifer, Mexico, *Hydrogeol. J.,* 10(5), 539–552.

Gourlay, M. R. (1994), Wave transformation on a coral reef, *Coastal Eng.,* 23, 17–42, doi:10.1016/0378-3839(94)90013-2.

Gourlay, M. R., and G. Colleter (2005), Wave-generated flow on coral reefs- an analysis for two-dimensional horizontal reef-tops with steep faces, *Coastal Eng.,* 52, 353–387.

Gulley, J., Martin, J. B., Screaton, E. J., and P. J. Moore (2011), River reversals into karst springs: A model for cave enlargement in eogenetic karst aquifers. *Geological Society of America Bulletin,* 123, 467, doi: 10.1130/B30254.1.

Hansen, D. V., and M. Rattray (1966), New dimensions in estuary classification, *Limnology and Oceanography,* 11 (3), 319–326.

Hardy, T. A., and I. R. Young (1996), Field study of wave attenuation on an offshore coral reef, *J. Geophys. Res*., 101(C6), 14,311–14,326, doi:10.1029/96JC00202.

Hayes, M. O., (1979), Barrier island morphology as a function of tidal and wave regime, *Leatherman, S.P. (Ed.), Barrier Islands from the Gulf of St. Lawrence to the Gulf of Mexico*. Academic Press, New York, pp. 1–27.

Hearn, C. J. (1999), Wave-breaking hydrodynamics within coral reef systems and the effect of changing relative sea level*, J. Geophys. Res.,* 104, 30,007–30,019, doi:10.1029/1999JC900262.

Hench, J. L., B. O. Blanton, and R. A. Luettich Jr. (2002), Lateral dynamic analysis and classification of barotropic tidal inlets, *Continental Shelf Research* 22, 2615–2631.

Hench, J. L., J. J. Leichter, and S. G. Monismith (2008), Episodic circulation and exchange in a wave-driven coral reef and lagoon system*, Limnol. Oceanogr.,* 53, 2681–2694, doi:10.4319/lo.2008.53.6.2681.

Hench, J. L., and J. H. Rosman, (2013), Observations of spatial flow patterns at the coral colony scale on a shallow reef flat, *Journal of Geophysical Research (Oceans)*, 118 (3): 1142-1156.

Herbers, T. H. C., S. Elgar, R. T. Guza, and W. C. O'Reilly (1995), Infragravity-frequency (0.005–0.05 Hz) motions on the shelf. Part II: Free waves, *J. Phys. Oceanogr.,* 25(6), 1063–1079, doi:10.1175/1520-0485(1995)025<1063: IFHMOT>2.0.CO;2.

Hernández-Terrones L. M., K. A. Null, D. Ortega-Camacho, and A. Paytan (2015), Water quality assessment in the Mexican Caribbean: Impacts on the coastal ecosystem, *Continental Shelf Research,* 102 (2015) 62–72, http://dx.doi.org/10.1016/j.csr.2015.04.015.

Janssen, T. T., J. A. Battjes, and A. R. Van Dongeren (2003), Long waves induced by short-wave groups over a sloping bottom*, J. Geophys. Res*., 108(C8), 3252.

Jay, D. A., and J. D. Smith (1988), Residual circulation in and classification of shallow estuaries. In: Dronkers, J., van Leussen, W. (Eds.), *Physical Processes in Estuaries,* Springer, Heidelberg, pp. 19–41, doi:10.1029/2002JC001515.

Joyce, T. (1989), On in Situ “Calibration” of Shipboard ADCPs, *Journal of Atmospheric and Oceanic Technology,* 6, 169-172.

Kaufmann, G., and J. Braun (1999), Karst aquifer evolution in fractured rocks, *Water Resour. Res.,* 35(11), 3223–3238.

Kennedy, D. M., and C. D. Woodroffe (2002), Fringing reef growth and morphology: A review, *Earth Sci. Rev.,* 57, 255–277, doi:10.1016/S0012-8252(01)00077-0.

Kraines, S. B., M. Isobe, and H. Komiyama (2001), Seasonal variations in the exchange of water and water-borne particles at Majuro Atoll, the Republic of the Marshall Islands, *Coral Reefs,* 20, 330–340, doi:10.1007/s00338-001-0191-8.

Kim, G., and D. Hwang (2002), Tidal pumping of groundwater into the coastal ocean revealed from submarine 222Rn and CH4 monitoring, *Geophys. Res. Lett.,* 29(14), doi:10.1029/2002GL015093.

Kundu, P. K., I. M. Cohen, and D. R. Dowling (2012), *Fluid Mechanics: Fifth Edition,* Academic Press, Waltham, MA.

Li, L., D. Barry, F. Stagnitti, and J. Parlange (1999), Submarine groundwater discharge and associated chemical input to a coastal sea, *Water Resour. Res.,* 35(11), 3253–3259.

Longuet-Higgins M. S., and R. W. Stewart (1964), Radiation stresses in water waves: a physical discussion with applications, *Deep-Sea Res.,* 11: 529—562.

Longuet-Higgins, M. S., and R. W. Stewart (1962), Radiation stresses and mass transport in surface gravity waves and application to surf beats, *J. Fluid Mech.,* 13, 481–504, doi:10.1017/S0022112062000877.

Lowe, R. J., J. L. Falter, M. D. Bandet, G. Pawlak, M. J. Atkinson, S. G. Monismith, and J. R. Koseff (2005), Spectral wave dissipation over a barrier reef, *J. Geophys. Res.,* 110, C04001, doi:10.1029/2004JC002711.

Lowe, R. J., U. Shavit, J. L. Falter, J. R. Koseff, and S. G. Monismith (2008), Modeling flow in coral communities with and without waves: A synthesis of porous media and canopy flow approaches, *Limnol. Oceanogr.,* 53(6), 2668–2680, doi:10.4319/lo.2008.53.6.2668.

Lowe, R. J., J. L. Falter, S. G. Monismith, and M. J. Atkinson (2009a), Wave- driven circulation of a coastal reef-lagoon system, *J. Phys. Oceanogr.,* 39, 873–893, doi:10.1175/2008JPO3958.1.

Lowe, R. J., J. L. Falter, S. G. Monismith, and M. J. Atkinson (2009b), A numerical study of circulation in a coastal reef-lagoon system, *J. Geophys. Res.,* 114 C06022, doi: 10.1029/2008JC005081.

Lowe, R. J., C. Hart, and C. B. Pattiaratchi (2010), Morphological constraints to wave-driven circulation in coastal reef-lagoon systems: A numerical study*, J. Geophys. Res.,* 115, C09021, doi:10.1029/ 2009JC005753.

Lu, Y., and R. G. Lueck (1999), Using a broadband ADCP in a tidal channel part II: Turbulence, *J. Atmos. Oceanic Technol.,*16, 1568–1579.

Lueck, Rolf (2015), Ocean turbulence: a 6-day introduction and training course, *Rockland Scientific Inc. Technical Note,* TN-033.

Lugo-Fernández, A., H. H. Roberts, W. J. Wiseman Jr., and B. L. Carter (1998), Water level and currents of tidal and infragravity periods at Tague Reef, St. Croix (USVI), *Coral Reefs,* 17, 343–349, doi:10.1007/ s003380050137.

Mariño-Tapia, I., R. Silva-Casarin, C. Enriques-Ortiz, E. Mendoza-Baldwin, E. Escalante-Mancera, and F. Ruiz-Reneria (2010), Transformation and wave-driven circulation on natural reefs under extreme hurricane conditions, *Coastal Engineering Proceedings* 1.32: waves-28.

Martin, J. B., J. E. Cable, P. W. Swarzenski, and M. K. Lindenberg (2004), Enhanced Submarine Ground Water Discharge from Mixing of Pore Water and Estuarine Water, *Ground Water*, *42*(7), 1000-1010.

Merino, M., and L. Otero (1991), *Atlas Ambiental Costero,* Puerto Morelos—Quintana Roo, Chetumal, México: Centro de Investigaciones de Quintana Roo (CIQRO).

Monismith, S. G. (2007), Hydrodynamics of coral reefs, *Annu. Rev. Fluid Mech.,* 39, 37–55, doi:10.1146/annurev.fluid.38.050304.092125.

Monismith, S. G. (2010), Mixing in estuaries, In: *Contemporary Issues in Estuarine Physics*, edited by A. Valle-Levinson, pp. 145–185, Cambridge Univ. Press, Cambridge, U. K.

Moore, W. S. (1996), Large groundwater inputs to coastal waters revealed by 226Ra enrichments, *Nature*, 380(6575), 612–614.

Moore, W. S. (1999), The subterranean estuary: A reaction zone of ground water and sea water, *Mar. Chem.,* 65(1), 111–125.

Moore, W. S. (2010), The effect of submarine groundwater discharge on the ocean, *Annu. Rev. Mar. Sci*., 2, 59–88.

Munk, W. H. (1949), Surf beat, *Eos Trans. AGU*, 30, 849–854.

Mutchler, T., K. H. Dunton, A. Townsend-Small, S. Fredriksen, and M. K. Rasser (2007), Isotopic and elemental indicators of nutrient sources and status of coastal habitats in the Caribbean Sea, Yucatan Peninsula, Mexico. *Estuar. Coast. Shelf Sci.,* 74, 449–457.

Nasmyth, P. W. (1970), *Ocean turbulence*. Ph.D. thesis, University of Bristish Columbia, Vancouver, British Columbia, Canada.

Null, K. A., K. L. Knee, E. D. Crook, N. R. de Sieyes, M. Rebolledo-Vieyra, L. Hernández-Terrones, and A. Paytan (2014), Composition and fluxes of submarine groundwater along the Caribbean coast of the Yucatan Peninsula, *Continental Shelf Res.,* 77, 38-50.

Osborn, T. R., and C. S. Cox (1972), Oceanic fine structure, *Geophysical Fluid Dynamics, 3*, 321–345.

Parra, S. M., I. Marino-Tapia, C. Enriquez, and A. Valle-Levinson (2014), Variations in turbulent kinetic energy at a point source submarine groundwater discharge in a reef lagoon, *Ocean Dyn.,* 1–14, doi:10.1007/s10236-014-0765-y.

Parra, S. M., A. Valle-Levinson, I. Marino-Tapia, and C. Enriquez, (2015), Salt intrusion at a submarine spring in a fringing reef lagoon, *J. Geophys. Res. Oceans*, 120, doi:10.1002/ 2014JC010459.

Paulsen, R. J., D. O'Rourke, C. F. Smith, and T. F. Wong (2004), Tidal Load and Salt Water Influences on Submarine Ground Water Discharge, *Ground Water*, *42*(7), 990-999.

Péquignet, A. N., J. M. Becker, M. A. Merrifield, and J. Aucan (2009), Forcing of resonant modes on a fringing reef during tropical storm Man-Yi, *Geophys. Res. Lett.,* 36, L03607, doi:10.1029/2008GL036259.

Peterson, R. N., W. C. Burnett, C. R. Glenn, and A. G. Johnson (2009), Quantification of point-source groundwater discharges to the ocean from the shoreline of the Big Island, Hawaii, *Limnol. Oceanogr.,* 54(3), 890–904.

Pomeroy, A., R. Lowe, G. Symonds, A. Van Dongeren, and C. Moore (2012), The dynamics of infragravity wave transformation over a fringing reef, *J. Geophys. Res.,* 117, C11022, doi:10.1029/2012JC008310.

Pope, S. B. (2000), *Turbulent Flows,* Cambridge Univ. Press, N. Y.

Prager, Ellen J. (1991), Numerical simulation of circulation in a Caribbean-type backreef lagoon: A preliminary study, *Coral Reefs,* 10:177-182.

Reidenbach, M. A., S. G. Monismith, J. R. Koseff, G. Yahel, and A. Genin (2006), Boundary layer turbulence and flow structure over a fringing coral reef, *Limnol. Oceanogr.,* 51(5), 1956–1968.

Rippeth, T. P., E. Williams, and J. H. Simpson (2002), Reynolds stress and turbulent energy production in a tidal channel, *J. Phys. Oceanogr.,*32,1242–1251.

Roberts H.H., and J. N. Suhayda (1983), Wave-current interactions on a shallow reef. *Coral Reefs,* 1:209-214.

Roberts H. H., S. P. Murray, and J. N. Suhayda (1975), Physical processes in a fringing reef system, *J. Mar. Res.,* 33:233-260.

Roelvink, D., and M. Stive (1989), Bar generating cross shore flow mechanisms on a beach, *J. Geophys. Res.,* 94(C4), 4785–4800.

Ruiz-Rentería, F., B. I. Van Tussenbroek, and E. Jordan-Dahlgren (1998), Puerto Morelos, Quintana Roo, México, In: *B. Kjerfve (Ed.). Caribbean coastal marine productivity (Caricomp): Coral reef, seagrass and mangrove site characteristics,* Paris: UNESCO.

Santos, I. R., W. C. Burnett, J. Chanton, N. Dimova, and R. N. Peterson (2009), Land or ocean? Assessing the driving forces of submarine groundwater discharge at a coastal site in the Gulf of Mexico, *J. Geophys. Res.,* 114, C04012, doi:10.1029/2008JC005038.

Sauvageot, H. (1992), *Radar Meteorology*, 384 pp., Artech House, Norwood,Mass.

Shoemaker W. B., K. J. Cunningham, E. L. Kuniansky, and J. Dixon (2008), Effects of turbulence on hydraulic heads and parameter sensitivities in preferential groundwater flow layer, *Water Resour. Res.,* 44, W03501, doi:10.1029/2007WR006601.

Simpson J. H., N. R. Fisher, and P. Wiles (2004), Reynolds stress and TKE production in an estuary with a tidal bore, *Estuar. Coast Shelf Sci,* 60:619–627, doi:10.1016/j.ecss.2004.03.006.

Souza, A.J., L.G. Alvarez, and T. Dickey (2004), Tidally induced turbulence and suspended sediment. *Geophys. Res. Lett.,* 31, L20309, doi:10.1029/2004GL021186.

Stacey, M. T., S. G. Monismith, and J. R. Burau (1999), Measurements of Reynolds stress profiles in unstratified tidal flow, *J. Geophys. Res.,* 104(C5), 10,933–10,949.

Symonds, G., K. P. Black, and I. R. Young (1995), Wave-driven flow over shallow reefs, *J. Geophys. Res.,* 100: 2639–2648.

Symonds, G., D. A. Huntley, and A. J. Bowen (1982), Two-dimensional surf beat: Long wave generation by a time-varying breakpoint, *J. Geophys. Res.,* 87(C1), 492–498, doi:10.1029/JC087iC01p00492.

Taebi, S., R. J. Lowe, C. B. Pattiaratchi, G. N. Ivey, G. Symonds, and R. Brinkman (2011a), Nearshore circulation in a tropical fringing reef system, *J. Geophys. Res.,* 116, C02016, doi:10.1029/2010JC006439.

Taebi, S., R. Lowe, C. Pattiaratchi, G. Ivey, and G. Symonds (2011b), The response of the wave-driven circulation at Ningaloo Reef, Western Australia, to a rise in mean sea level, In: *Coasts and Ports 2011 : Diverse and Developing: Proceedings of the 20th Australasian Coastal and Ocean Eng. Conference and the 13th Australasian Port and Harbour Conference,* Barton, A.C.T.: Engineers Australia, 2011: 706-711.

Taniguchi, M. (2002), Tidal effects on submarine groundwater discharge into the ocean, *Geophys. Res. Lett.,* 29(12), doi:10.1029/2002GL014987.

Taniguchi, M., W. C. Burnett, J. E. Cable, and J. V. Turner (2002), Investigation of submarine groundwater discharge, *Hydrol. Processess,*16(11), 2115–2129.

Torres-Freyermuth A., I. Mariño-Tapia, C. Coronado, P. Salles, G. Medellín, A. Pedrozo-Acuña, R. Silva, J. Candela, and R. Iglesias-Prieto (2012), Wave-induced extreme water levels in the Puerto Morelos fringing reef lagoon, *Nat Hazards Earth Syst Sci,* 12:3765–3773. doi:10.5194/nhess-12-3765-2012.

Valiela I., J. Costa, K. Foreman, J. M. Teal, B. Howes, and D. Aubrey (1990), Transport of groundwater-borne nutrients from watersheds and their effects on coastal waters, *Biogeochemistry,* 10:177–197. doi:10.1007/BF00003143.

Valle-Levinson, A., G. Gutierrez de Velasco, A. Trasviña, A. J. Souza, R. Durazo, and A. J. Mehta (2009), Residual exchange flow in subtropical estuaries, *Estuaries and Coasts,* 32:54–67, doi:10.1007/s12237-008-9112-1.

Valle Levinson, A., C. Li, T. Royer, and L. Atkinson (1998), Flow patterns at the Chesapeake Bay entrance, *Continental Shelf Research,* 18(10). 1157–1177.

Valle-Levinson, A., I. Marino-Tapia, C. Enriquez, and A. F. Waterhouse (2011), Tidal variability of salinity and velocity fields related to intense point-source submarine groundwater discharges into the coastal ocean, *Limnol. Oceanogr.,* 56(4), 1213–1224.

Van Dongeren, A., J. Battjes, T. Janssen, J. van Noorloos, K. Steenhauer, G. Steenbergen, and A. Reniers (2007), Shoaling and shoreline dissipation of low-frequency waves, *J. Geophys. Res.,* 112, C02011, doi:10.1029/ 2006JC003701.

Vera, I., I. Marino-Tapia, and C. Enriquez (2012), Effects of drought and subtidal sea-level variability on salt intrusion in a coastal karst aquifer, *Mar. Freshwater Res.,* 63(6), 485–493.

Walter R. K., N. J. Nidzieko, and S. G. Monismith (2011), Similarity scaling of turbulence spectra and cospectra in a shallow tidal flow, *J Geophys Res.,* 116, C10019, doi:10.1029/2011JC007144.

Waterhouse, A., A. Valle-Levinson, and R. A. Morales (2012), Tidal asymmetries in velocities and stratification over a bathymetric depression in a tropical inlet, *Cont. Shelf Res.,* 48: 87-99.

Wiens, H., (1962), *Atoll Environment and Ecology*. Yale University Press.

Werner, A. D., and C. T. Simmons (2009), Impact of sea-level rise on sea water intrusion in coastal aquifers, *Ground Water*, 47(2), 197–204.

Wiles, P. J., T. P. Rippeth, J. H. Simpson, and P. J. Hendricks (2006), A novel technique for measuring the rate of turbulent dissipation in the marine environment, *Geophys. Res. Lett.,* 33, L21608, doi:10.1029/2006GL027050.

Young, M.B., M. E. Gonneea, D. A. Fong, W. S. Moore, J. Herrera-Silveira, and A. Paytan (2008) Characterizing sources of groundwater to a tropical coastal lagoon in a karstic area using radium isotopes and water chemistry, *Mar. Chem.,* 109, 377–394.

BIOGRAPHICAL SKETCH

Jacqueline Marie Branyon grew up in Florida where she received her Bachelor of Science in civil engineering from the University of Florida in 2010. She continued her education by earning her Master of Engineering in civil engineering at the University of Florida in 2012. Jacqueline was the recipient of the Water Institute Graduate Fellowship that allowed her to pursue her PhD in coastal and oceanographic engineering. She has served as a Research Assistant in the Coastal Engineering department of the Engineering School of Sustainable Infrastructure & Environment (ESSIE). After graduation, she will work as a coastal scientist for Moffatt & Nichol and pursue her Professional Engineer license.